



Skolkovo Institute of Science and Technology

**Development of Group of Flying Robots
with Multifunctional Robotic Limbs
aimed at Operations in Cluttered Environments**

Doctoral Thesis

by

Grigoriy Yashin

Doctoral Program in Engineering Systems

Supervisor

Associate Professor, Dzmitry Tsetserukou

Moscow - 2020

© Grigoriy Yashin, 2020. All rights reserved.

I hereby declare that the work presented in this thesis was carried out by myself at Skolkovo Institute of Science and Technology, Moscow, except where due acknowledgement is made, and has not been submitted for any other degree.

Candidate (Grigoriy Yashin)

Supervisor (Assoc. Prof. Dzmitry Tsetserukou)

Development of Group of Flying Robots
with Multifunctional Robotic Limbs
aimed at Operations in Cluttered Environments

by

Grigoriy Yashin

December 2, 2020 00:10

Submitted to the Space Center of Research, Entrepreneurship and Innovation
on December 2020, in partial fulfillment of the requirements for the
Doctoral Program in Engineering Systems

Abstract

Flying robots are being developed to explore underground space, implement search and rescue operations, assist in emergency situations, and perform industrial inspection and maintenance. The environment of these missions contains a lot of various objects arranged in space orderly or, more often, randomly. Such an environment can be characterized as cluttered. In these conditions, the robots can be controlled using teleoperation or standalone automatic mode. Most robots designed for aerial manipulation are controlled by automated algorithms that are responsible for performing specific tasks. On the other hand, during rescue operations and the exploration, it is necessary to use multifunctional robots or a group of such robots capable of following the commands of an operator located in a safe place.

The present thesis proposes a solution to the problem of developing a multifunctional robotic system for the operation in a cluttered environment and method for effective remote control of such a system. In the framework of this solution, we developed two novel compact flying robots equipped with robotic limbs and controlled remotely through a [VR](#)-based teleoperation system. The first robot of the AeroVR project is the quadrotor equipped with 4-degrees of freedom ([DoF](#)) manipulator underneath for the implementation of aerial manipulation. The second robot, DroneGear, is the hexarotor equipped with four [2-DoF](#) legs. This robot can land on an uneven surface and move to the desired position using LocoGear algorithm. The control algorithms for these robots were designed, simulated, and tested in laboratory conditions with a ground-truth [Motion Capture System \(Mocap\)](#) VICON system.

In the framework of the AeroVR project, a novel teleoperation system is aimed at accurate object manipulation by the [UAV](#) equipped with a robotic arm in a remote environment in the absence of direct visual contact between a human operator and a flying robot. The robotic arm attached to the quadrotor can reproduce human hand movements when an operator used [IMU](#)-based wearable interface. The robot flight is managed by [VR](#) controller with visual feedback from the camera mounted

on the manipulator gripper. For a better perception of the current state of the robot and the surrounding environment, a digital twin of the robot and video from the camera are projected in the [head-mounted display \(HMD\)](#) in real-time. The user study revealed that the developed wearable interface and the traditional [VR](#) controller have comparable characteristics in manipulator control. However, according to [Analysis of Variance \(ANOVA\)](#) results, the wearable interface is a more natural control device ($F(1,28)=5.04$, $p=0.03<0.05$) and allows the operator to perform remote manipulation faster by 27 % with better matching of the manipulator position to the target set-point.

DroneGear is the first prototype of the robot capable of flying, landing on an uneven surface, and walking on the ground to the desired position. Though this robot had been designed to provide adaptive landing on uneven surfaces, we developed a LocoGear, a new algorithm for terrain locomotion of [UAV](#) equipped with the robotic landing gear. LocoGear is the kinematic-based algorithm developed by trajectory analysis of the robot [center of mass \(CoM\)](#), calculation of the dynamic loads using the Lagrangian dynamic formulation, and kinetostatic methods. We conducted laboratory experiments to verify the LocoGear approach based on feedforward control that proves the capability of landing gear to move along the desired trajectory with the speed of 0.75 cm/sec.

The robots and algorithms developed in this thesis present a significant step towards improving remote control methods for aerial manipulation and developing multifunctional robots for operation in a cluttered environment.

Publications

Journal publications

1. G. Yashin, A. Egorov, Zh. Darush, N. Zherdev, and D. Tsetserukou. Loco-gear: Locomotion analysis of robotic landing gear for multicopters. *IEEE Journal on Miniaturization for Air and Space Systems*, 1(2):138–147, 2020. doi:[10.1109/JMASS.2020.3015525](https://doi.org/10.1109/JMASS.2020.3015525)
2. Y. S. Sarkisov, G. A. Yashin, E. V. Tsykunov, and D. Tsetserukou. Dronegear: A novel robotic landing gear with embedded optical torque sensors for safe multicopter landing on an uneven surface. *IEEE Robotics and Automation Letters*, 3(3):1912–1917, 2018. doi:[10.1109/LRA.2018.2806080](https://doi.org/10.1109/LRA.2018.2806080)

Submitted journal paper

1. G. Yashin, D. Trinitatova, N. Zherdev, R. Agishev, and D. Tsetserukou. Airin-terface: Study of effectiveness of aerial manipulation using vr system. *Journal of Intelligent & Robotic Systems*. 16 pages, 2020. Submitted

Conference proceedings

1. G. A. Yashin, D. Trinitatova, R. T. Agishev, R. Ibrahimov, and D. Tsetserukou. Aerovr: Virtual reality-based teleoperation with tactile feedback for aerial manipulation. In *2019 19th International Conference on Advanced Robotics (ICAR)*, pages 767–772, 2019. doi:[10.1109/ICAR46387.2019.8981574](https://doi.org/10.1109/ICAR46387.2019.8981574)

Posters

1. G. A. Yashin, I. A. Kalinov, E. V. Tsykunov, and D. O. Tsetserukou. Touch and weight sensitive robotic arm for uav aimed at aerial manipulation and safe physical human-drone interaction. In *IEEE Haptics Symposium*, 2018. URL <https://cutt.ly/cuv8z5U>

Patents published during the author's PhD activity, though not strictly related to this thesis

1. I. A. Kalinov, G. A. Yashin, A. A. Petrovskiy, and D. O. Tsetserukou. Hybrid robotic platform for warehouse inventory automation, Patent: RU 197 225 U1, April 2020. URL bit.ly/fips-ru-patent-197225
2. I. A. Kalinov, R. T. Agishev, A. A. Petrovskiy, E. S. Safronov, T. V. Melnik, M. A. Kurenkov, V. S. Ramzhaev, I. N. Idrisov, G. A. Yashin, and D. O. Tsetserukou. The program for stabilization, localization and navigation of uavs relative to a mobile robot in a warehouse with a gps signal and the presence of a large amount of metal, Certificate of state registration of a computer program: RU 2019661130, April 2019. URL bit.ly/fips-ru-patent-2019661130

Dedicated to my mother Irina, wife Daria and daughter Polina.

Acknowledgments

I would like to thank Daria Trinitatova and Ruslan Agishev for their valuable contribution to this work and reliable support in research part dedicated to remote control and tests of the aerial manipulation. I am especially grateful to Yuri Sarkisov for his suggestions given during the numerous discussions of the developed locomotion strategy and the dynamic modeling of the landing platform for the multicopters. To my supervisor Dzmitry Tsetserukou for the bold research ideas, the creation of the most advanced robotics laboratory and the provided opportunity to create the newest technology in Russia. I also thank Tamash Fazli for practical advice in developing electrical circuits.

SkolTech's administrative and FabLab staff also deserve an acknowledgment for the comfortable education process at the institute. Thanks to all my laboratory and SkolTech colleagues for sharing with me professional experience and lots of good moments.

Finally, special thanks to my family for the continuous support and motivation during this long scientific journey.

Contents

| | |
|---|-----------|
| Glossary | 15 |
| 1 Introduction | 16 |
| 1.1 Motivation | 16 |
| 1.2 Specifications of the Application Scope | 23 |
| 1.3 Challenges and Proposed Solutions | 26 |
| 1.4 Research Contribution | 31 |
| 1.5 Thesis Structure | 32 |
| 2 Aerial Manipulator with 4-DoF | 35 |
| 2.1 State of the Art | 35 |
| 2.2 System Overview | 38 |
| 2.3 Kinematic Model | 42 |
| 2.3.1 Inverse Kinematics | 43 |
| 2.3.2 Forward Kinematics | 44 |
| 2.4 Dynamic Model | 45 |
| 2.5 GUI for Manipulator Control | 46 |
| 2.6 Experiment on Manipulation in Flight via GUI | 48 |
| 2.7 Concluding Remarks | 50 |
| 3 VR-based Teleoperation System for Aerial Manipulation | 52 |
| 3.1 State of the Art | 52 |
| 3.2 System Overview | 57 |
| 3.3 Manipulator Control with the VR controller | 59 |
| 3.4 Wearable Teleoperation Interfaces | 60 |
| 3.4.1 Smart Glove | 60 |
| 3.4.2 IMU-based Wearable Interface | 62 |
| 3.4.3 Interface with IMU and Flex Bending Sensors | 62 |
| 3.5 Control of the UAV using a VR Controller | 63 |
| 3.6 UAV Localization | 65 |
| 3.7 System Communication | 65 |
| 3.8 Experiment of Manipulation Control in Flight | 67 |
| 3.8.1 Description of VR Setup | 67 |
| 3.8.2 VR-based Teleoperation Tests | 69 |
| 3.9 User Study | 71 |
| 3.9.1 Manipulation Experiment in the Stationary Case | 71 |
| 3.9.2 Experiment of Aerial Manipulation in Virtual Mine | 85 |

| | | |
|----------|---|------------|
| 3.10 | Concluding Remarks | 91 |
| 4 | Analysis of Locomotion Algorithm for Landing Gear | 94 |
| 4.1 | State of the Art | 94 |
| 4.2 | System Overview | 97 |
| 4.3 | Problem Statement | 99 |
| 4.4 | Locomotion Algorithm | 100 |
| 4.4.1 | Movement Sequence | 100 |
| 4.4.2 | Kinematic Model | 102 |
| 4.4.3 | Calculation of the Robot Center of Mass | 105 |
| 4.4.4 | Dynamic Model | 107 |
| 4.4.5 | Simulation of the Robot Motion | 110 |
| 4.5 | Experimental Results | 112 |
| 4.5.1 | Parameter Configuration | 113 |
| 4.5.2 | Experiment of the Path Following | 118 |
| 4.6 | Concluding Remarks | 119 |
| 5 | Conclusion | 121 |
| 5.1 | Research Outcomes | 121 |
| 5.2 | Future Outlook | 125 |
| A | Electrical Circuit of IMU-based Wearable Interface | 129 |
| B | Electrical Circuit of DroneGear | 131 |
| C | Potential and Kinetic Energies of Landing Platform | 133 |
| | Bibliography | 139 |

List of Figures

| | | |
|------|--|----|
| 1-1 | Applications of the aerial manipulation: (a) the insertion task [Korpela et al., 2014], (b) valve turning [Korpela et al., 2014], (c) grabbing objects in flight [Thomas et al., 2014], (d) surface inspection [Bodie et al., 2019], (e) object grasping by two aerial manipulators [Ramon-Soria et al., 2020], (f) flying robot for maintenance of the power lines [Suarez et al., 2020]. | 18 |
| 1-2 | Block-diagram of human-robot interaction. | 19 |
| 1-3 | Types of the cluttered environments: (a) the interior of the building after earthquake [Michael et al., 2012], (b) mine after collapse [Pérez-Higueras et al., 2019], underground tunnel (c) and cave (d). | 24 |
| 1-4 | The scenario for operating a group of robots. | 30 |
| 1-5 | Scheme of the relations between the chapters. | 32 |
| 2-1 | Types of aerial manipulators: (a) 1-DoF gripper [Pounds et al., 2011], (b) two multi-DoF robotic arms [Suarez et al., 2018], (c) cable-Suspended manipulator [Sarkisov et al., 2019]. | 36 |
| 2-2 | Layout of the manipulator servo motors. | 39 |
| 2-3 | The distributions of displacement along Z-axis (a) and stresses (b) in manipulator link. | 41 |
| 2-4 | Scheme of the manipulator. | 42 |
| 2-5 | Block scheme of the dynamic model of 4-DoF manipulator. | 45 |
| 2-6 | Block scheme of the dynamic model servomotor Dynamixel MX-106T. | 46 |
| 2-7 | Simulation of the change in torque over time. | 46 |
| 2-8 | GUI to monitor the manipulator state. | 47 |
| 2-9 | The trajectory of the wrist joint position during experiment. | 49 |
| 2-10 | Dependencies of target coordinates (a) and motor torques (b) of the manipulator, roll (c) and pitch (d) angles from the experiment time for the flight test with the GUI teleoperation. | 49 |
| 3-1 | The flight test of the aerial manipulation. a) Robot during teleoperation. b) VR visualization in Unity. c) Operator with HMD and wearable interface. | 57 |
| 3-2 | Input buttons of the VR controller using for the manipulator control. | 59 |
| 3-3 | The scheme of the smart glove (a), pictures of an interface with IMU and flex bending sensors (b), components of the IMU-based haptic interface (c) and the location of the interface on the arm (d). | 61 |
| 3-4 | Unfiltered (a) and filtered (b) data from the IMU sensors. | 62 |

| | | |
|------|---|----|
| 3-5 | Data from the interface with IMU and flex bending sensors. | 63 |
| 3-6 | The principle scheme of communication of the VR-based teleoperation. | 66 |
| 3-7 | The scheme of communication for the flight experiment. | 68 |
| 3-8 | Digital twin of the room for the experiments on aerial manipulation. | 68 |
| 3-9 | Scheme of the rooms for VR-based teleoperation experiment. | 69 |
| 3-10 | Coordinates (a) and motor torques (b) of the manipulator, roll (c) and pitch (d) angles vs. time for the flight test using teleoperation. | 70 |
| 3-11 | (a) The stationary test of the VR-based teleoperation using IMU-based interface. The snapshot of the VR environment is shown in the upper left corner. (b) The test of the robot control using HTC VIVE controllers in a virtual environment simulating a mine. | 72 |
| 3-12 | VR environment for the user study before establishing a connection with a real manipulator. | 73 |
| 3-13 | Objects for manipulation used in the User Study. | 74 |
| 3-14 | Evaluation of the participant's experience for both control methods in the form of a 7-point Likert scale (1 = completely disagree, 7 = completely agree). Means and SD are presented. | 75 |
| 3-15 | The statistics of the mean number of attempts of the task execution. | 78 |
| 3-16 | The results of the Peg-in-Hall task execution. The first three columns represent the number of participants who completed the task on the first, second, and third attempts, respectively. The fourth bar indicates the number of participants failed the task. | 78 |
| 3-17 | The peg-in-hole task. The initial setup for the task (a), assemblies of the objects in the proposed format (b), with the transfer of both objects to the top box (c, d), after lifting the cup and placing the orange cylinder in it (e). | 79 |
| 3-18 | The average task execution time and length of the trajectory for the manipulation tasks. | 80 |
| 3-19 | The trajectories of the operator wrist position (target trajectory) and the gripper position for the up-down tasks. | 82 |
| 3-20 | The trajectories of the operator wrist position (target trajectory) and the gripper position for the down-up, ball-in-tape, and rotated cube tasks. | 83 |
| 3-21 | The trajectories of the operator wrist position (target trajectory) and the gripper position for the peg-in-hole tasks. | 84 |
| 3-22 | The average manipulation speed. | 84 |
| 3-23 | The initial position of the robot in virtual mine (a) and the screenshot of the robot near the gas source (b). | 86 |
| 3-24 | Evaluation of the participant's experience for both control methods in the form of a 7-point Likert scale (1 = completely disagree, 7 = completely agree). Means and SD are presented. | 87 |
| 3-25 | User evaluation of both control methods. Average values are marked with crosses. Scatter points represent answer of individual participants. | 88 |
| 3-26 | Experimental results averaged across all participants. a) Task execution time; b) The drone velocity during the task. Average values are marked with crosses. | 90 |

| | | |
|------|--|-----|
| 3-27 | The trajectory of the aerial manipulator in virtual mine for the second User Study. The green and red curves represent the trajectories of the first participant, while the pink and turquoise curves represent the trajectories of the other one. | 91 |
| 4-1 | The robots capable to fly and move on the ground: (a) HyTAQ [Kalantari and Spenko, 2013], (b) HERALD [Latscha et al., 2014], (c) HexaWalker, and (d) Hexapod-Quadcopter Robot [Pitonyak and Sahin, 2017]. | 96 |
| 4-2 | The landing platform for the multicopters (a) and the leg structure (b). | 97 |
| 4-3 | The scheme of LocoGear (in this scheme, the yellow leg is hidden behind the blue one). | 99 |
| 4-4 | The locomotion algorithm. A schematic representation of the robot in profile is shown on the XZ plane. Position of the robot CoM relative to the support polygon (blue line around the footpads position) is shown on the XY plane. | 101 |
| 4-5 | The scheme of LocoGear after the inclination and transfer of the leading leg. | 103 |
| 4-6 | The sequences of the robot locomotion along a curtate cycloid (orange, blue and black lines are the intermediate positions of supporting, side and leading legs accordingly). | 104 |
| 4-7 | The scheme of LocoGear for calculation of the robot CoM. | 105 |
| 4-8 | The robot scheme for calculation of the joint torques. | 108 |
| 4-9 | Joint and inclination angles (a), servomotor torques (b) vs. time, and the sequences of the robot locomotion (c) during the robot movement to step by the leading leg on the obstacle. | 111 |
| 4-10 | The movement of the robot along random trajectory after landed on the step (blue, black, orange and yellow dashed lines are the trajectories of legs, turquoise line is the motion trajectory of CoR). | 112 |
| 4-11 | GUI to control DroneGear at the heuristic analysis. | 113 |
| 4-12 | The phases of the Motion cycle (the white and yellow points are the initial positions of the leading and left leg respectively). | 115 |
| 4-13 | The desired and real values of β during one Motion cycle. | 116 |
| 4-14 | Trajectories for 2 experiments of the Motion cycle in XZ frame (a, c) and YZ frame (b, d). | 117 |
| 4-15 | Real movement paths of the CoR for five experiments at the specifying rectilinear movement (a) for Motion cycle without cycloid, b) with using cycloid during the CoM transfer). | 118 |
| 5-1 | Group behavior of the robots for search and rescue operations (a), usage of the multi-functional hybrid robot (b), the detection of plant diseases and sampling using the flying robot with robotic limbs (c). | 126 |
| A-1 | The electrical circuit of the IMU-based interface. | 129 |
| B-1 | The electrical circuit of DroneGear. | 131 |

List of Tables

| | | |
|-----|---|----|
| 1.1 | List of tasks performed by developed group of robots. | 28 |
| 2.1 | Technical characteristics of AeroVR. | 40 |
| 2.2 | Natural frequencies of manipulator components. | 41 |
| 2.3 | Technical characteristics of motors of DJI E600 multirotor propulsion system. | 42 |
| 2.4 | Comparative table of existing aerial manipulators. | 50 |
| 4.1 | Technical characteristics of DroneGear. | 98 |

Glossary

- ANOVA** Analysis of Variance. 4, 76, 84, 92
- CCS** Cartesian coordinate system. 98, 105, 106
- CoM** center of mass. 4, 13, 37, 51, 70, 95, 98, 100–103, 105, 106, 110, 113, 114, 116, 118, 119, 124, 138
- CoR** center of the robot. 98, 100, 102–104, 106, 107, 114, 119, 120, 124
- CoS** coordinate system. 42–44
- DoF** degree of freedom. 3, 11, 17, 27, 30, 32, 35–39, 42, 43, 45, 50, 52, 56, 62, 64, 79, 95–97, 99, 121, 123
- FE** finite element. 40, 41
- GUI** Graphical User Interface. 11, 31–33, 46–50, 53, 54, 67, 98, 113, 122, 123
- HMD** head-mounted display. 4, 20, 21, 31, 54–58, 67, 123
- IMU** Inertial Measurement Unit. 3, 11, 12, 31, 45, 58, 60–63, 74, 76, 77, 80, 81, 92, 93, 96, 122, 123, 125, 130, 132
- Mocap** Motion Capture System. 3, 31, 58, 65–69, 116, 119, 122, 124
- Motion cycle** The robot movement on one step. 13, 100, 110, 112–119, 124
- ROS** Robot Operating System. 19, 21, 65–67
- SAM** cable-Suspended Aerial Manipulator. 36, 52
- SD** standard deviation. 76, 77, 88, 89
- UAV** Unmanned Aerial Vehicle. 3, 4, 16, 19–23, 25, 27–29, 31, 33–38, 40, 44, 47, 48, 50, 51, 53, 54, 56–58, 60, 63–65, 67–70, 76, 88, 93–96, 106, 123, 124, 127
- VR** Virtual Reality. 3, 4, 12, 19, 21, 26, 29, 31, 33, 34, 42, 52–54, 56–60, 63–67, 69, 71, 74–77, 81, 85, 87–93, 121, 122

Chapter 1

Introduction

1.1 Motivation

Unmanned Aerial Vehicles (UAV) are being developed to perform a set of tasks, such as: parcel delivery in logistic business (Amazon PrimeAir [Amazon, 2016], UPS [Burns, 2017], et al.), implementation of search and rescue operations [Sousa et al., 2019], the assistance in emergency situations [Lygouras et al., 2019], industrial inspection¹ and maintenance [Ollero et al., 2019]. The UAV additionally equipped with one or several robotic arms can perform significantly more number of tasks for third and fourth applications. For example, such flying robots are able to carry out a detailed inspection of the pipelines and bridges, holding a heavy object with the swarm of drones [Kim et al., 2018], ecological sampling [Kutia et al., 2015] or land in point of interest and perform a detailed environmental exploration.

The first studies in the area of aerial manipulation were carried out in 2010-2011. It was the experiments on moving objects using a swarm of UAVs [Bernard et al., 2011], grabbing an object using a UAV equipped with a grip [Ghadiok et al., 2011], and applying an unmanned helicopter with a gripper [Pounds et al., 2011]. In 2013 the control system, research on dynamics and stabilization, and flight experiments of the first multirotor with manipulators were presented in three studies [Kim et al., 2013, Korpela et al., 2013, Jimenez-Cano et al., 2013]. A large project ARCAS²

¹Flyability launches ELIOS 2 for intuitive indoor inspection, available: <https://www.flyability.com/news/flyability-elios-2-indoor-inspections> (Retrieved March 22, 2020)

²ARCAS, available: <http://www.arcas-project.eu/> (Retrieved March 20, 2020)

dedicated to the development and experimental validation of the first cooperative free-flying robot system for assembly and structure construction was launched in the autumn of the same year. In 2015 the AEROARMS project³ [Ollero et al., 2018] was launched based on the results of the ARCAS project. This project aims to research on the mechatronics, control, telemanipulation perception and planning problems for aerial manipulation tasks. In 2016 Japanese company PRODRONE⁴ demonstrated multicopter with two manipulators, which can lift objects from the ground and land on the railing by using two manipulators. Nowadays the international scientific community was conducted considerable research of the aerial manipulation in the following areas: design of aerial robots with multiple degree of freedom (DoF) manipulators [Bellicoso et al., 2015, Suarez et al., 2018], a study of kinematics and dynamics during manipulation in midair [Marchand et al., 2014, Yüksel and Franchi, 2016], research of effective control systems for flight stabilization during interacting with objects [Kim et al., 2013, Rossi, 2017, Imanberdiyev and Kayacan, 2019], trajectory planning approaches [Chen et al., 2019], choice of robot equipment by necessary sensors to perform desired tasks and robot perception in surrounded space [Ramon-Soria et al., 2020]. The most significant results of research and developments in the field of aerial manipulation were published in two handbooks [Orsag et al., 2018, Ollero and Siciliano, 2019].

Over 9 years, the aerial manipulation has evolved from the laboratory tests to the validation experiments in conditions close to actual exploitation (e.g., pipeline inspection [Ollero et al., 2019]). Nevertheless, the question of controlling similar flying robots remains open, whether it is necessary to control manually, automatically, or in semi-autonomous mode. A large number of the works propose the autonomous performance of individual specific tasks, such as the insertion tasks [Korpela et al., 2014], valve turning [Korpela et al., 2014], grabbing objects in flight [Thomas et al., 2014], surface inspection [Bodie et al., 2019], object grasping by two aerial manipulators [Ramon-Soria et al., 2020], maintenance of the power lines [Suarez et al., 2020], and others (Fig. 1-1 b). At the same time, only some of the papers are devoted to

³AEROARMS, available: <https://aeroarms-project.eu/> (Retrieved June 6, 2020)

⁴PRODRONE Unveils the World's First Dual Robot Arm Large-Format Drone. PRODRONE, available: <https://www.prodrone.jp/en/archives/1420/> (Retrieved March 20, 2020)

the teleoperation of the flying robots [Suárez et al., 2018, Coelho et al., 2019], and one research is devoted to the semi-autonomous manipulation [Staub et al., 2018].

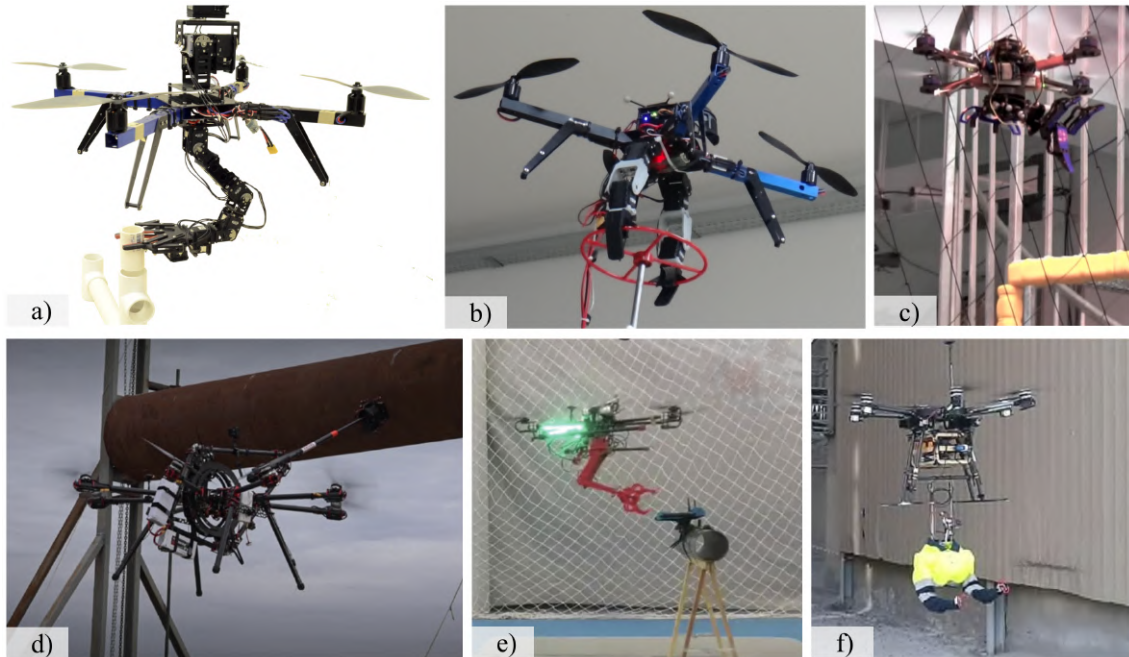


Figure 1-1: Applications of the aerial manipulation: (a) the insertion task [Korpela et al., 2014], (b) valve turning [Korpela et al., 2014], (c) grabbing objects in flight [Thomas et al., 2014], (d) surface inspection [Bodie et al., 2019], (e) object grasping by two aerial manipulators [Ramon-Soria et al., 2020], (f) flying robot for maintenance of the power lines [Suarez et al., 2020].

The industrial maintenance and assistance in rescue operations are the two areas that require the most versatile robots. The usage of robots for these purposes often implies the ability to perform non-standard actions that arise already during task execution. In this case, the flying robots capable of performing aerial manipulation are of particular interest. For instance, at the present time industrial tasks are carried out by personnel. Some of these tasks must be performed using high-altitude equipment. Even partial implementation of these activities by the robot can help to reduce human risk and cost, as evidenced by the focus of European projects ARCAS and AEROARMS. For this purpose, the robot should carry out different specific tasks with high accuracy that could not be performed only in autonomous mode. The robot control can be achieved by teleoperation methods. In this case, the robot and the operator can be located in remote places, that is especially important for hazardous conditions.

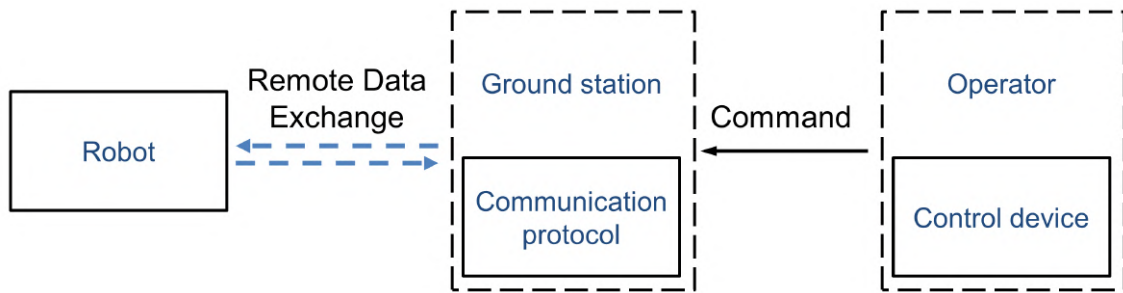


Figure 1-2: Block-diagram of human-robot interaction.

We can describe the block-diagram of the remote robot control, as it is shown in Fig. 1-2. In this scheme we see the ground station, which gets commands from the control device of an operator and exchanges data with a robot using a communication protocol. With regard to the communication protocol, data exchange via Wi-Fi is most often used type of wireless communication (for instance [Mohaimeni-anPour and Vaughan \[2018\]](#), [Coelho et al. \[2019\]](#)). The reason for this is probably due to the convenience of connecting to [Robot Operating System \(ROS\)](#) and providing transmission of large amounts of images and video from cameras at the using methods of computer vision (for instance [Roldán et al. \[2019\]](#), [Sun et al. \[2020\]](#)). While the connection of [VR](#) equipment (for example, HTC VIVE) is often carried out using Bluetooth that ensures fast and stable transfer of small size data amount (e.g. position, orientation, temperature, pressure and other). However it should be noted that both Bluetooth and Wi-Fi are inferior to radio protocols in the communication range between the [UAV](#) and the ground station. Wi-Fi and Bluetooth stop transmitting information after 50-100 meters [[Sen et al., 2018](#)], while the radio can work up to 600 meters [[Li et al., 2016](#)]. An example of using radio communication is presented in the work of [Pereira et al. \[2016\]](#). Thus, it is efficient to use Bluetooth and Wi-Fi in indoor conditions (e.g. laboratory) or when using a group of robots, where one of the robots will be a mobile base station. When working over a large area (e.g. forestry), it is rational to use radio communication.

As we mentioned earlier, the number of studies on the teleoperation of flying robots is small; therefore, it is necessary to consider the existing control methods for ground or stationary robots. Computer vision methods are often used in human-

robot collaboration tasks, especially for remote control of robots. In a number of works [Naseer et al., 2013, MohaimenianPour and Vaughan, 2018, Nagi et al., 2014], it was proposed an approach for controlling a UAV located in close proximity to the operator using an on-board camera (RGB camera, Kinect sensor) that recognizes face and hand gestures. However, this approach cannot be applied in the tasks of control of UAVs in remote environment. Jang et al. [2019] and Sun et al. [2020] used the Leap Motion controller mounted on the HMD to track the operator's hands. This method has a significant drawback, the Leap Motion working area is significantly limited, and the operator must keep his hands in front of the helmet in the area of $0.227 m^3$.

Another approach includes the development of a physical interface for teleoperation with a set of motion capture sensors and electromyography sensors [Miehlbradt et al., 2018, Wu et al., 2019]. Such a solution requires placing a set of sensors on the operator's body or using special suits or clothing items. In Wu et al. [2019] the operator control the motion of the mobile platform by slightly bending in the direction of the desired movement exploiting the displacement of his/her center of pressure. This way of controlling the robot is unusual and can be tiring during long missions. Rognon et al. [2018] developed FlyJacket, which is a wearable interface based on a soft exoskeleton for controlling the UAV with gestures of the upper body. The exoskeleton includes a motion-tracking device to monitor body movements, an arm support system to prevent fatigue, and is coupled to virtual reality goggles to provide visual feedback. In addition, the application of haptic feedback in teleoperation systems for improving control is considered in a number of works by using commercial desktop haptic devices with force-feedback [Kanso et al., 2015, Valenzuela-Urrutia et al., 2019, Son, 2019]. Son [2019] tested of the haptic feedback based on the cues corresponding to the UAVs' velocity or directed forces from sensed obstacles. This study aimed to improve the perception of flight control in a remote environment. To enhance the teleoperation precision Valenzuela-Urrutia et al. [2019] used Phantom Omni for manipulator position control with force feedback based on the use of point cloud data obtained with an RGB-D camera. In their experiments, they used virtual workspace to display the current position of the manipulator.

Roldán et al. [2019] studied the integration of ROS-based robots with VR for monitoring a fleet of drones, commanding a robot manipulator, and integration of multiple ground and aerial robots. They concluded that the usage of VR provides a comfortable perception of the current robot state, which makes it easier to perform the necessary scenarios. The scientific search for improving the perception of the environment during remote flight control can be called one of the important tasks in aerial manipulation. Currently, it is possible to purchase various First-person view goggles for UAV control. Such devices allow the pilot to see real-time video from the camera on the UAV and some important characteristics during the flight (speed, flight altitude, battery charge, and others). However, the visual experience can be enhanced with VR or/and the addition of haptic feedback. VR allows the operator to look at the flying robot from the side, and with the help of tactile feedback, the operator can receive additional information about the interaction of the robot with the environment. In 2008 Ferre et al. [2008] suggests that usage of HMD can significantly improve working within the aforementioned conditions by a more precise and effective telemanipulation performance. All of this can be applied at the performing of the aerial manipulation, when it is necessary to provide a comfortable provision of a large amount of visual information, so that the operator should not be overloaded and can perform the assigned tasks with the help of a robot in a calm state. It is also necessary that the control device should be intuitive and without discomfort at usage in order to better focus on the task.

Separately, special attention should be given to the usage of flying robots for remote applications such as monitoring or delivering cargo to hard-to-reach or dangerous places, such as urban areas devastated by natural disasters. UAVs are also used to carry out rescue operations to search for missing tourists in the territory of nature reserves with a complex terrain⁵. The paper [Pérez-Higueras et al., 2019] is dedicated to the usage of a group of robots in mines. These robots are significantly different from each other in functionality and size. The researchers evaluated the navigation and exploration system for the robotic team consisting of a ground robot,

⁵How do drones and neural networks look for missing people? And how effective are they? TASS, Russian news agency, available: <https://tass.ru/obshchestvo/6757981> (Retrieved June 6, 2020)

micro UAV, and a teleoperated snake-like robot. They developed and tested the algorithms of the robotic team behavior in the simulation environment for search and rescue activities in mine incidents. Also, within the framework of this project, it is supposed to use a mobile ground-based robot as a carrier for the small robots. In another example, a group of researchers from the University of Pennsylvania [Michael et al., 2012] used the ground and aerial robots to generate the three-dimensional maps of floors of a destructed building after the earthquake. In these conditions UAV with one or several robotic limbs can significantly extend the application of robots in rescue operations by accompanying such activities in the conditions of destroyed urban infrastructure and natural landscape, when it may be necessary to deliver medicine, drinking water or ancillary equipment (for instance, spare batteries for power tools or repair kits). The equipment of the flying robots with several manipulators can be useful not only for performing operations with objects, but also for landing on uneven surfaces. With such functionality, the robots can spend their power sources more efficiently due to the rational use of flight and ground modes. However we can notice that in recent times, research in the field of using a group of robots for search and rescue operations is carried out using highly specialized robots with a bias in the mapping and indoor localization. At the same time, significantly less research is devoted to the development of a multifunctional robots.

The usage of the robotic arms designed for aerial manipulation not only for performing operations with objects, but also for landing on uneven surfaces, is of considerable interest for research. Xie et al. [2015] developed an algorithm for landing and grasping objects using two robotic legs. Their work was devoted to the development of effective mechanics of the landing chassis and control system. It is worth noting that similar chassis can also be used to perform dynamic grasping of objects, as was demonstrated in the work of Thomas et al. [2014]. Arns and Zhang [2019] designed the chassis for landing and performing operations with objects based on the delta robot. There are developments in the use of classic paired manipulators to perform tasks on manipulation and landing [Yu et al., 2019]. Paul et al. [2019] combined landing gears and manipulator system for UAV with the objective to provide the ability to manipulate objects and acting as adaptive landing gear on uneven

terrain. However, the presence of only three limbs does not allow such configuration to move on the ground.

It is worth considering another combination of functions for the robotic limbs of flying robots, this is the usage of landing gear to move on the ground. This necessity arises when there are cavities in the ground or it is required to pass through a narrow passage and move in a dilapidated room with a low ceiling. UPS [Burns, 2017] is testing package delivery by a UAV launching from the truck cargo. It is expected that UAVs will be launched and land on a moving car (e.g., in Walmart's concept). After the landing, the UAV needs to move to the charging station. Another example of the application of the multifunctional robots can be found in exploring underground caves. Delivering or extracting things, that are located in hardly accessible places are potential tasks in this mission. Examples of this would be ecological sampling or installation of the observation sensors deep inside the caves, that can be reached only through narrow tunnels.

Based on state of the art, we defined the main problem as developing a multifunctional flying robotic system and methods for effective remote control of such a system. In order to better characterize this problem, two clarifying subtasks were formulated. It is necessary to design a comfortable control interface to perform the various aerial manipulation tasks with a cognitive perception of the robot state. And the second subtask is the development of a locomotion algorithm for the landing platform.

1.2 Specifications of the Application Scope

We can summarize that there is a tendency of active development of both multifunctional robots and the execution of operations by groups of robots in order to more efficient implementation of critical tasks for shorter periods of time. The main potential fields of application for such robots are search and rescue operations on the reserves, underground tunnels, mines, in areas following natural disasters. Although such robots can also be used for industrial maintenance. In order to promote these developments in the world, competitions are held on the usage of robots for search

and rescue operations in forests⁶ and underground environments⁷. The first competition is aimed to develop devices or technologies capable of detecting the exact coordinates of the location of a missing person without means of communication in the natural environment. Despite the competition focus in the field of image processing, it is worth noting that the list of necessary tasks in these conditions can be expanded by delivering essential items, as well as methods to inform the found person about subsequent actions using the robot. The DARPA challenge is addressed to development of novel approaches to rapidly map, navigate, and search underground environments during disaster response scenarios. Tunnel, urban underground and cave are used as a test zones in this competition. Examples of some types of the cluttered environments are shown in Fig. 1-3.



Figure 1-3: Types of the cluttered environments: (a) the interior of the building after earthquake [Michael et al., 2012], (b) mine after collapse [Pérez-Higueras et al., 2019], underground tunnel (c) and cave (d).

At this time, mine robots were used to manipulate fan doors, push aside obstacles, and transmit video and atmospheric monitoring information (mine gas and temperature readings). In the paper [Murphy et al., 2009], the authors noted the

⁶Odyssey. In Search of Man, available: <https://odyssey.community/> (Retrieved June 22, 2020)

⁷DARPA's Subterranean Challenge, available: <https://www.subtchallenge.com/> (Retrieved June 22, 2020)

three deployment scenarios: surface entry, borehole entry, and void entry. The surface and borehole entries are the most common scenarios. The uniqueness of the environment and operating conditions in a mine require to use multifunctional robots. The operation functions of these robots include the ability to a different location of deployment, beyond-line-of-sight operations, real-time data acquisition, wide field of view, work envelope, and capable of 2–3 h missions.

Humanitarian demining is another prospective application area which requires the usage of the robot with flexible and adaptable mobility and with obligatory remote control [Habib, 2008]. For this type of tasks a robot should be able to locomote and maneuver in the unstructured environment and on the different type of terrain. The design should integrate proper balance between maneuverability, stability, speed, and the ability to overcome obstacles [Habib, 2008]. Marques et al. [2016] defined the technical characteristics of robots for mine clearance as follows: a high level of protection against the environmental conditions (dust, humidity, temperature, etc.), long and continuous operation time between battery charging/changing, wireless communication range, low cost, high maintainability, easy to use. Currently tracked and wheeled robots equipped with mine detectors or manipulators are most often used today (for example, robot MTGR⁸). At the same time, the UAVs can be used to improve locating and detecting minefield and also greatly enhance wide-area survey and assessment. Summarizing the above, we can say that a group of flying robots can effectively assist in mine clearance operations. The flight speed significantly exceeds the speed of movement on the ground, which provides a high speed of exploration of large areas. The usage of a robot with robotic legs allows observing a point of interest in a more energy-saving mode. On the other hand, aerial manipulation allows inspecting dangerous areas from different angles, including exploring cavities and hollows. Besides, the presence of a manipulator allows removing small objects that can be used to cover explosives. Using a digital twin of a robot along with a video stream from the robot's cameras will provide the operator with the necessary amount of information about the current state of the robot

⁸MTGR® - The World's Lightest Full-Featured Tactical Ground Robot, available: <http://robo-team.com/products/mtgr/> (Retrieved September 17, 2020)

and the environment around it. Originally developed to improve manufacturing processes, digital twins can be defined as digital replications of real-world objects bridging the physical and virtual worlds [El Saddik, 2018]. Real twins could be equipped with sensors so that digital twins could replicate their behavior (e.g., motion or exploration process) that provides the interaction in real-time with the real world. Thereby digital twins facilitate the means to monitor, understand, optimize the functions of physical processes, and remote control of real devices.

1.3 Challenges and Proposed Solutions

As a result of the study of the potential application area of the flying robots and aerial manipulation field, we can determine the following actual challenges:

- **Standalone vs. manual mode.** Algorithms of automatic terrain analysis to the search of objects require significant computing power and most often require the determination of the specific search goals. That is, Standalone mode can not fully replace manual control by the operator at the moment. Besides, when the robot works in automatic operation mode, it is necessary to use auxiliary precision sensors for accurate positioning during interaction with surrounding objects.
- **Sophisticated manual control.** On the other hand, during manual control, an operator is visually overloaded to find the target object in a real environment and to control the robot at the same time. In addition, manual control is usually performed in the field of view of the operator or when performing complex tasks using the monitor. VR technologies, the usage of the robot digital twin, and tactile feedback can enhance the perception of the environment around the robot.
- **Limited functionality.** Most often, robots are used to perform specific tasks, since in this case it is easier to develop automatic mode of their work (the absence of transients). The usage of a replaceable payload can compensate for the limited robot functionality. However, when operating robots in a cluttered

environment, the robot's ability to immediately adapt to the environment is required, as noted above.

- **Autonomy vs. payload.** The usage of highly specialized devices for specific tasks is justified only in the case of a modular robot structure. However, replacing the tool leads to the need to return at the starting position and, accordingly, increase time costs. The installation of several different mechanical devices on the UAV is usually impossible, since this requires a more powerful propulsion system and an increase of the robot size, which is not always acceptable. Also, a more powerful computer or equipment with additional sensors increases power consumption, and hence reduces the autonomous operation.

Lack of payload versatility and effective control methods slow down the commissioning of the flight robots to perform real assistance in search and rescue operations. Nevertheless, the aforementioned technical difficulties are the initiators of the scientific search for new approaches of remote robot control and the development of new algorithms for the functioning of existing robots, such as landing platforms. Based on the existed needs, we can formulate the main research question for this thesis:

"How to improve the functional efficiency and control method of the unmanned aerial vehicles equipped with robotic limbs?"

In search of an answer to this question we developed the group of the robots, which is capable of performing tasks indicated in Table 1.1. The first robot, AeroVR, is the quadrotor equipped with 4-degree of freedom (DoF) manipulator underneath for the implementation of aerial manipulation. The second robot, DroneGear, is the hexarotor equipped with four 2-DoF legs, which is capable of landing on the uneven surface and moving to the desired position. Potentially, both robots can be controlled both in stand-alone mode (moving to the target point) and in manual control/teleoperation mode (moving and exploring the local area). It is worth noting that the DroneGear can act as a coordinator, transmitting data about target coordinates to assistant robots, such as AeroVR.

| AeroVR | DroneGear |
|--|---|
| <ul style="list-style-type: none"> • Ecological sampling. • Deliver and install of sensors (e.g., sensors for the collection of information about the environment state). • Deliver the aid or repair kit. • The interaction with objects (e.g., door opening, grasping). • Inspection of the structure safety in teleoperation mode. | <ul style="list-style-type: none"> • Flight and ground movement. • Landing in target position. • Exploration of the surrounding area (in case of installation of additional sensors). • Functioning as a coordinating robot for other service UAVs (in case of installation of additional sensors). |

Table 1.1: List of tasks performed by developed group of robots.

As we noted earlier, control of the flying robots during the implementation of various operations is most often performed using pre-programmed specific tasks. At the same time, as noted in [Section 1.1](#), the scientific community actively develops the field of remote control of stationary manipulators, as well as control technologies using wearable devices. In 2020 team of the DLR researchers presented the teleoperation method for aerial manipulation using onboard visual and inertial sensors, an object tracking algorithm, and a pre-generated object database. During experiments the operator controlled cable-suspended manipulator by a haptic device and 3D visualization in virtual reality [[Lee et al., 2020](#)]. In this work, particular attention is paid to the data exchange protocol between the robot and the operator control device. However, the usage of the joystick to control the manipulator in space and radio control equipment to handle the UAV are not intuitive and convenient methods. The operator must initially undergo additional training for the usage of this control system. Thereby, existing control methods require considerable time for learning how to operate robots and do not provide natural interaction with the robot (a more detailed consideration of existing systems for remote control of robots is presented in [Section 3.1](#)). Thus, it is worth asking the following clarifying research question:

"How can the operator remotely control the aerial manipulator in comfortable way?"

Our hypothesis is that controlling a robot using a wearable interface connected to VR can expand the functionality of aerial manipulators, improve the perception quality of the environment surrounding the robot, and reduce the operator's training time. To validate this hypothesis, we developed and tested several types of wearable interfaces for tracking the orientation of the operator's hand. To provide the operator with a perception of the current state of the robot, we made a VR application that displays a digital twin of the robot and a video stream from the robot's camera in real-time. We conducted two user studies to evaluate efficiency of the proposed method for remote control of the manipulator and control of the UAV.

The main characteristics of any UAV are a time of autonomous operation, range of remote control, and payload. These parameters determine how long, at which distance, and which tasks the UAV is capable of performing. When we expand the functionality of the flying robot for better exploration of the target area or interaction with objects, we need to equip the UAV by additional mechanics and sensors. This payload has its weight, and depending on it the propulsion system is selected for UAV. Accordingly, the bigger the power of its motors, the more energy is consumed for the autonomous functioning of the robot, which means more massive batteries are required. Thus, at the design stage of the flying robots, it is critically important to choose the optimal ratio of the size and weight of the robot to the desired payload, or respectively to the number of different operations or the duration of a particular operation depending on the robot application. As we mentioned early and described in detail in Section 4.1, landing platforms are being recently developed for flying robots to land on the uneven surfaces safely. But if the robot can land somewhere and its landing platform is theoretically capable of moving on the ground, it would be better if the robot has a locomotion function. It can provide more economical use of the battery charge and increase the time of autonomous operation, respectively. Also, it ensures the multifunctionality of an existing payload. The second additional research question is as follows:

"How can the UAV equipped with landing gear walk without structure improvements?"

For this goal, we proposed a new kinematic-based locomotion algorithm for the landing gear with four legs with 2-DoF. The development of this algorithm was carried out in two stages. Using a heuristic approach, we experimentally determined the required number of motion gates and possible stable positions for each gate. At the second stage, based on the experimental results, we set the trajectory of the robot motion and calculated its kinematic model. To analyze the developed algorithm, we created a visualization of robot motion in MATLAB, then we calculated the servomotor torques during robot motion using Lagrangian dynamic formulation and kinetostatic methods, and finally test this algorithm on the real robot.

One of the potential scenarios for operating the developed group of robots is presented in Fig. 1-4. For example, in the underground environment there was a partial collapse of the rocks. DroneGear flies into the tunnel to the point where the collapse occurred. An accumulation of toxic gas (e.g., carbon monoxide) may occur at this point. Initially, the robot needs to reconnaissance of the place, then tries to find a suitable place for the landing and explores the area around it. In the event of coal collapse detection (in this case, methane appears most frequently), DroneGear informs the second robot about the specified coordinates via a radio link. Finally, AeroVR arrives at the specified point and install a gas analyzer in teleoperation

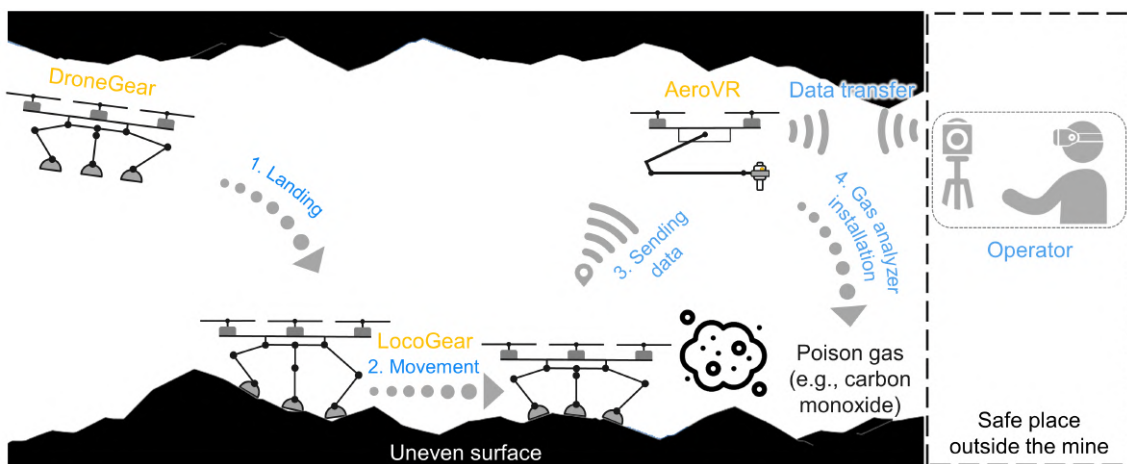


Figure 1-4: The scenario for operating a group of robots.

mode. We used a simple version of this scenario to conduct a user study of the developed remote control system using VR. In this user study, the participants controlled the AeroVR robot and searched for gas sources in a virtual mine, and after finding them, they placed gas detectors near these sources (Subsection 3.9.2).

1.4 Research Contribution

The present thesis aims to expand the capabilities of the robots for aerial manipulation via VR-based teleoperation and to demonstrate two novel multifunctional flying robots for potential assistance in the cluttered environment (e.g., search and rescue operations in mines or on the terrain after the natural disasters). The kinematic and dynamic models for these robots were calculated in Maple and MATLAB. The Graphical User Interface (GUI) in MATLAB was designed for each robot in order to estimate and adjust their processes of movement. Finally, the robots were tested in laboratory conditions with a ground-truth VICON Motion Capture System (Mocap). User studies were used for the evaluation of the VR-based teleoperation system. The main contributions of this thesis can be summarized as follows:

- The novel human-robot interaction strategy was developed for accurate object manipulation by the UAV equipped with a robotic arm in a remote environment without direct visual contact between a human operator and a flying robot. The lightweight robotic arm was assembled and attached to the quadrotor. This manipulator is capable of reproducing human hand movements. The manipulator is controlled by developed wearable IMU-based interface. The robot flight is managed by HTC VIVE controller with visual feedback from the camera mounted on the manipulator. Such intuitive control allows an operator to manipulate remote objects successfully with short preliminary training. For a better perception of the current state of the robot and the environment surrounding it, a digital twin of the robot and video from the camera located on the end effector are projected into the head-mounted display (HMD) in real-time. The effectiveness of this method was confirmed during user study.
- A novel non-traditional locomotion algorithm for the quadrupedal landing

platform was developed and tested. This approach was called LocoGear. In the framework of this approach, the robot movement by one step consists of the movement of the robot center along a path consisting of a cycloid and parabola segments, and the movement of the legs along parabolic paths. The experimental tests of the robot moving along a given path were performed.

1.5 Thesis Structure

The Fig. 1-5 shows the relations between the thesis chapters. Chapter 2 and Chapter 3 are dedicated to the development of the AeroVR project, Chapter 4 contains information about research and development of the LocoGear algorithm for the DroneGear robot. AeroVR and DroneGear robots are equipped with robotic limbs which have only rotational DoF in joints. The kinematics of these limbs is described using Denavit-Hartenberg parameters. Thus, calculation of the kinematics for the robotic arm was used for heuristic analysis. It is also worth noting that the calculation principles of the manipulator dynamics were used as the basis for calculating the dynamic loads of the DroneGear robot. We use the GUI for motion visualization and adjustment of the manipulator to set the necessary parameters for the manipulator operation. Changing these parameters provides flexible configuration and debugging of the manipulator at the design stage. Therefore, based

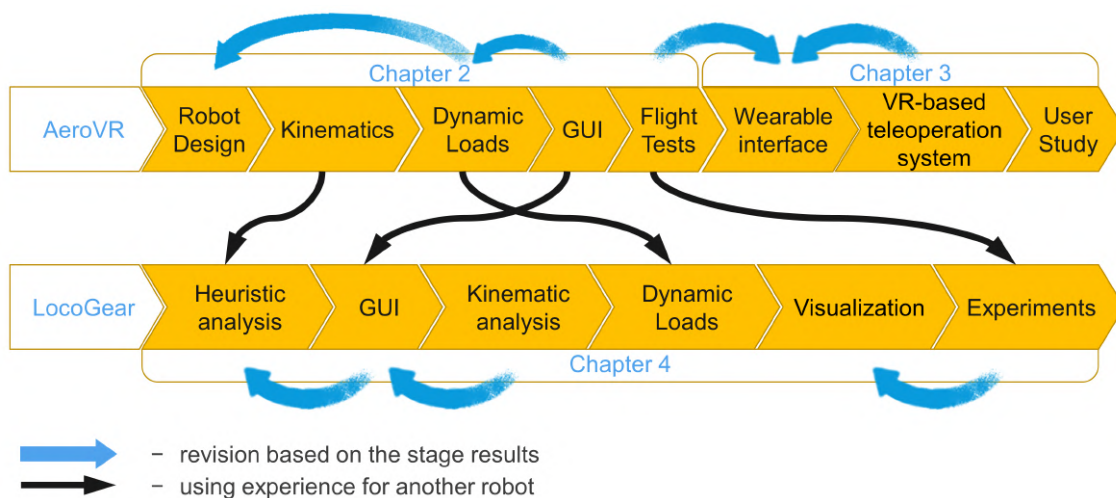


Figure 1-5: Scheme of the relations between the chapters.

on this development, a second interface was written to study the movement of the DroneGear robot. In addition the results of flight experiments of the AeroVR robot using the GUI motivated us to develop a VR-based teleoperation system for more convenient control of the aerial manipulation. This remote control system was developed in several iterations with the goal of creating a most comfortable wearable device for the manipulation control. Finally, the control electronics of the DroneGear robot function based on the same algorithms as AeroVR electronics. Nevertheless, since the tests of the robots were carried out almost in parallel, part of the control program code was improved based on the experiments carried out on both robots.

This thesis is organized as follows.

Chapter 1 - Introduction. In this part we have presented the general overview of the current state of technologies relevant to this research, the motivation of this thesis, specifications of the application scope, proposed solution, and established aims during this research.

Chapter 2 - Aerial Manipulator with 4-DoF. This chapter comprises the state of the art of the aerial manipulator design (Section 2.1), the information about design of the robotic arm for UAV (Section 2.2), kinematic and dynamic model of the manipulator (Section 2.3 and Section 2.4 respectively). A description of the GUI for manual control and adjustment of the manipulator are presented in Section 2.5. Experimental results of the manipulator control at flight using GUI are presented in Section 2.6.

Chapter 3 - VR-based Teleoperation System for Aerial Manipulation. The chapter consists of nine sections and summary, and narrates about the development and tests of the VR-based teleoperation system. Section 3.1 contains information about the state of the art of the teleoperation methods and devices, which is used for the manipulation and control flying robots and manipulators. In Section 3.3 we described the principle of manipulator control using a VR controller. Section 3.4 comprises the information about design and experimental comparison of the wearable interface developed for the VR-based teleoperation. In Section 3.5 we described the principle of UAV control using

a VR controller. The UAV localisation approach and description of the communication system are given in Section 3.6 and Section 3.7, respectively. User study results of the VR-based teleoperation control over aerial manipulator at flight are presented in Section 3.8. The evaluation of the system performance by the group of users is considered in Section 3.9.

Chapter 4 - Locomotion Algorithm for Landing Gear. The chapter consists of five sections and summary, and contains information about the development and tests of the LocoGear approach. Section 4.1 narrates about the state of the art of the quadrupedal robots and landing platforms for UAV. The structure of the landing gear and their technical characteristics are presented in Section 4.2. Section 4.3 comprises the problem statement of the movement of the landing gear. A description of the locomotion algorithm, kinematic and dynamic models of the landing platform, simulation of the robot motion are presented in Section 4.4. Experimental results of the robot movement in the laboratory conditions are described in Section 4.5.

Chapter 5 - Conclusion. In the last chapter, we summarize the results obtained during experiments and simulations. Also, we discuss three prospective research and commercialization opportunities with the application developed technologies.

Appendix A - Electrical circuit of IMU-based wearable interface. This section contains the electrical circuit of wearable interface which is an appendix for Chapter 3.

Appendix B - Electrical circuit of DroneGear. This section contains the electrical circuit of DroneGear which is an appendix for Chapter 4.

Appendix C - Potential and Kinetic Energies of Landing Platform. This section is appendix for Chapter 4. In this part the calculation of the potential and kinetic energies for the landing platform is described.

Chapter 2

Aerial Manipulator with 4-DoF

2.1 State of the Art

In the field of aerial manipulation, we can identify several types of interaction with payload [Kutia, 2019]. It can be simple load carrying, grabbing objects using 1-DoF gripper, manipulation by one or two multi-DoF robotic arms, or aerial interaction with objects using cable-Suspended manipulator (Fig. 2-1). These technologies are intended for different applications and, accordingly, distinguished by the hardware design, maximum payload, dynamic loads, and type of control methods.

Load carrying and usage of 1-DoF gripper under the UAV are of the greatest interest in order to move payloads between two static landing platforms. The advantages of these type aerial interaction with an objects are balancing the load relative to the UAV's center of mass, therefore, the dynamics of such robots is simpler. In addition, the absence of additional mechanisms for manipulating objects in space increases the payload. All of the above has provided significant support for the development of this technology by commercial logistics companies. In 2013 the company SF Express in cooperation with XAIRCRAFT were the first developers performed tests of the parcel delivery in place without infrastructure¹. After a while, the Amazon company took the initiative and began engaged in the active development of the parcel delivery to the customer by quadrotor with the automatic vertical grasping of

¹Drone Delivery Service Launched in China – SF Express, available: <https://dronesonvideo.com/drone-delivery-service-launched-in-china/> (Retrieved June 14, 2020)



Figure 2-1: Types of aerial manipulators: (a) 1-DoF gripper [Pounds et al., 2011], (b) two multi-DoF robotic arms [Suarez et al., 2018], (c) cable-Suspended manipulator [Sarkisov et al., 2019].

the object [Amazon, 2016]. Besides significant interest from commercial companies, in 2011 scientists from the University of Pennsylvania and Yale University independently were one of the first developers who studied the control of UAVs equipped with the gripper [Mellinger et al., 2011, Pounds et al., 2011].

A cable-suspended load is more often attached to the helicopters, that is applied to firefighting and forestry. Cable-Suspended interaction with objects was proposed in 2008 Markus et al. [2008], this approach allows to deliver heavy loads by a group of aerial vehicles. Since then, this technology has been greatly improved. Today **cable-Suspended Aerial Manipulator (SAM)** platform, which is equipped with propulsion units, is being developed in DLR [Sarkisov et al., 2019, 2020]. The **SAM** is hanged on the main aerial carrier (e.g. a helicopter) utilizing a long cable. This solution allows performing aerial manipulation in a complex environment while keeping the main aerial carrier at a safe distance from the obstacles. However cable length has a significant influence on load-carrying dynamics, which requires the use of more complex control algorithms. **SAM** are large and can be used to interact with large

and heavy objects.

As was mentioned in [Section 1.1](#), 2013 can be considered as the beginning of the active development of the scientific direction of aerial manipulation using the robotic arm. Specially designed robotic arms with from 2 to 6 DoF [[Kim et al., 2013](#), [Suarez et al., 2015](#), [Korpela et al., 2013](#), [Bellicoso et al., 2015](#), [Cano et al., 2013](#)], as well as 7-DoF KUKA industrial manipulator [[Kondak et al., 2014](#)], and delta robots [[Danko et al., 2015](#)] were designed and tested as manipulators attached to the UAV. Some paper [[Lee et al., 2016](#), [Ohnishi et al., 2017](#)] were dedicated to the mechanical compensation of CoM displacement of the robot during aerial manipulation in front of the UAV. If we consider the evolution of the design of manipulators in ARCAS and AEROARMS projects, it is worth noting that the version of the robotic arm with 6-DoF was originally designed [[Cano et al., 2013](#)], however, the first tests were carried out using a manipulator with 3-DoF [[Jimenez-Cano et al., 2013](#)]. In AEROARMS project the latest versions of the robots have 4-DoF, three of which are located on the shoulder [[Suarez et al., 2018](#)].

The diversity of structures for manipulating objects in the midair reflects the trend of the scientific search for a minimalistic design of the manipulator, which would have a lightweight and high strength characteristics. At the same time, the rigidity of the structure should ensure the damping of vibrations that can arise both during the flight of the robot and due to dynamic loads during the manipulation process. The manipulator actuators must ensure stable interaction with objects of a certain weight, which is determined by the carrying capacity of the carrier UAV. In addition to technical requirements, the choice of the manipulator configuration is carried out based on the functionality which the flying robot should perform. As noted above, to perform simple operations for the delivery of various goods, only a grabbing device is generally sufficient, while it makes sense to perform the inspection or maintenance of industrial facilities using multi-DoF manipulators. The installation of the sensors may require the usage of multiple robotic arms, as was done when installing the sensors on the power line [[Suarez et al., 2020](#)].

In addition to structural characteristics, robots also differ in the set of sensors required to perform specific tasks. However, compact cameras currently have the

most important role in aerial manipulation. The cameras are used for target tracking, trajectory generation without collision and trajectory tracking control [Chen et al., 2019]. In the paper of Danko and Oh [2014] the manipulator is visually servoed using an eye-in-hand camera. With this ability the robotic arm compensate the undesired UAV motions. Also in the article of Heredia et al. [2014] investigated the control of a flying robot using two cameras on the drone frame and one on the end effector. Papers [Kim et al., 2016, Laiacker et al., 2016] are focusing on accurate manipulations with objects by flying robots using computer vision algorithms. In other words, the equipment of a aerial manipulator with one or several cameras is necessary to perform interaction with objects in both the cases, for automatic control and remote teleoperation.

Based on the considered state of the art we developed robotic arm equipped with 4-DoF and camera mounted on the gripper. It provides simplicity of the manipulator construction and robot control. The additional necessary freedom of movement to manipulate in space can be implemented using the three rotational and three translation DoFs of the UAV. A similar approach was demonstrated in [Chen et al., 2019], but this robot was operated in stand-alone mode. AeroVR and DroneGear robots were designed as small size prototypes, such compact robots can be useful for implementation of sampling, installation sensors and exploration of the environment after disasters (such as was discussed in Section 1.1).

2.2 System Overview

Large payload, long continuous flight time, and size are the main UAV requirements. Taking into account these limitations, we assembled a quadrotor based on the frame DJI Flame Wheel ARF KIT F450 with propulsion system DJI E600, and Cube Flight Controller (based on Pixhawk 2.1). Also, onboard computer Odroid is installed on the robot to provide the data exchange between the client computer and autopilot, client computer and gripper camera via Wi-Fi connection (communication system is described in Subsection 3.8.1). The robot is connected to a stationary power supply via cable to eliminate the need for a changing battery during long flight

tests.

4-DoF manipulator consists of three motors in articulated joints (Dynamixel servomotors MX-106T, MX-64T and AX-12 in the shoulder, elbow and wrist joints respectively), two links, one servomotor for the grip rotation (Dynamixel AX-12) and the grip with 1-DoF (Futuba S9156). 3D model of flying robot is developed in CATIA and shown in Fig. 2-2. The manipulator servomotors are chosen based on the necessary values of the maximum torque in the manipulator joints, that was calculated in Section 2.4. For designed manipulator the maximum torques have the following values:

- The shoulder joint: $T_{max1} = 5.167$ N·m.
- The elbow joint: $T_{max2} = 2.792$ N·m.
- The wrist joint (pitch): $T_{max3} = 0.850$ N·m.
- The rotation joint of gripper (roll): $T_{max4} = 0.097$ N·m.
- The grasping mechanism: $T_{max5} = 0.614$ N·m, this value is calculated using gear ratio.

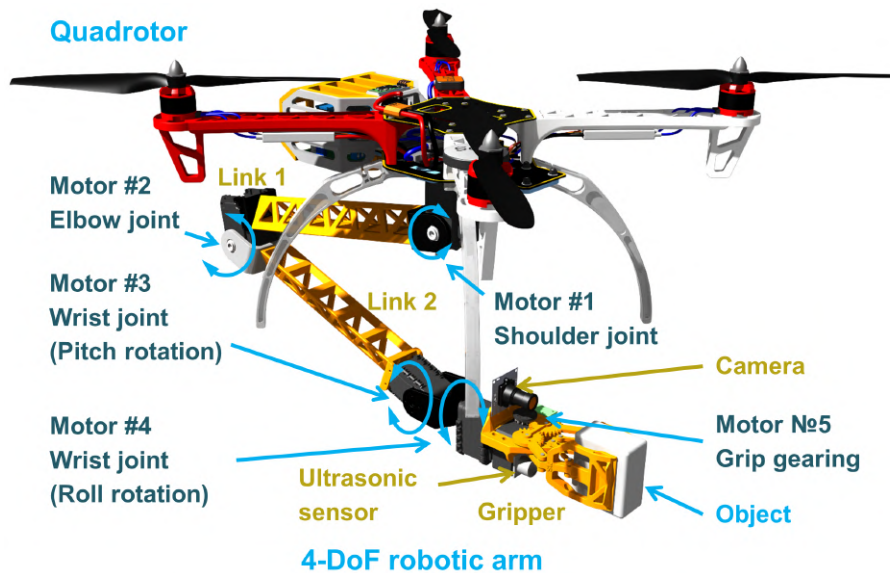


Figure 2-2: Layout of the manipulator servo motors.

The grip design is based on the four-bar linkage mechanism with gear ratio 1,85. On the gripper we installed ultrasonic sensor HC-SR04. This sensor can measure

the distance to an object in the range from 2 to 400 cm. To ensure the transmission of visual feedback, the manipulator is equipped with a compact digital 8-megapixel camera with a 75-degree field of view. Also, two force sensitive resistors are fixed on the gripper bars. These sensors detect the contact between the gripper and the object and determine the force with which the bars of the gripper hold the cargo. The technical characteristics of the developed robot are presented [Table 2.1](#).

| | |
|---|---------------|
| Weight of flying robot | 2080 g |
| Manipulator weight (with electronics) | 918 g |
| Maximum robot payload | 400 g |
| Manipulator length | 740 mm |
| Distance between the edges of the propeller and end of the grip | 400 mm |
| Number of the manipulator DoF | 4 |
| Work range of the shoulder joint | 0 - 180 deg. |
| Work range of the elbow joint | 0 - 180 deg. |
| Work range of the wrist joint (pitch) | -90 - 90 deg. |
| Work range of the wrist joint (roll) | -90 - 90 deg. |

Table 2.1: Technical characteristics of AeroVR.

To perform the aerial manipulation tasks it is necessary to mount the robotic arm under the UAV. Therefore we designed link 1 so that the robotic arm folds completely and does not interfere during the take-off and landing phases. Manipulator links have a truss structure to achieve a light and rigid construction. The links are 3D-printed from PLA material. We conduct the stress-strain analysis of the links in FE Software Abaqus 6.14 to validate that the plastic links with designed structure provides the minimum weight and maximum rigidity. For the finite element method, the robot link was considered as cantilever beam loaded by uniform gravity force and torque of 5.3 N·m at the opposite end. This load corresponds to the holding an object weighing 400 grams in the extended position of the manipulator. The distributions of displacement along Z-axis and stresses in the manipulator link 1 are provided in [Fig. 2-3\(a\)](#) and [Fig. 2-3\(b\)](#), respectively. The displacement along Z-axis is less than 3.5 mm at maximum payload, the deflection angle is less than 1 degree. Thus, the manipulator has a robust structure while manipulating an object.

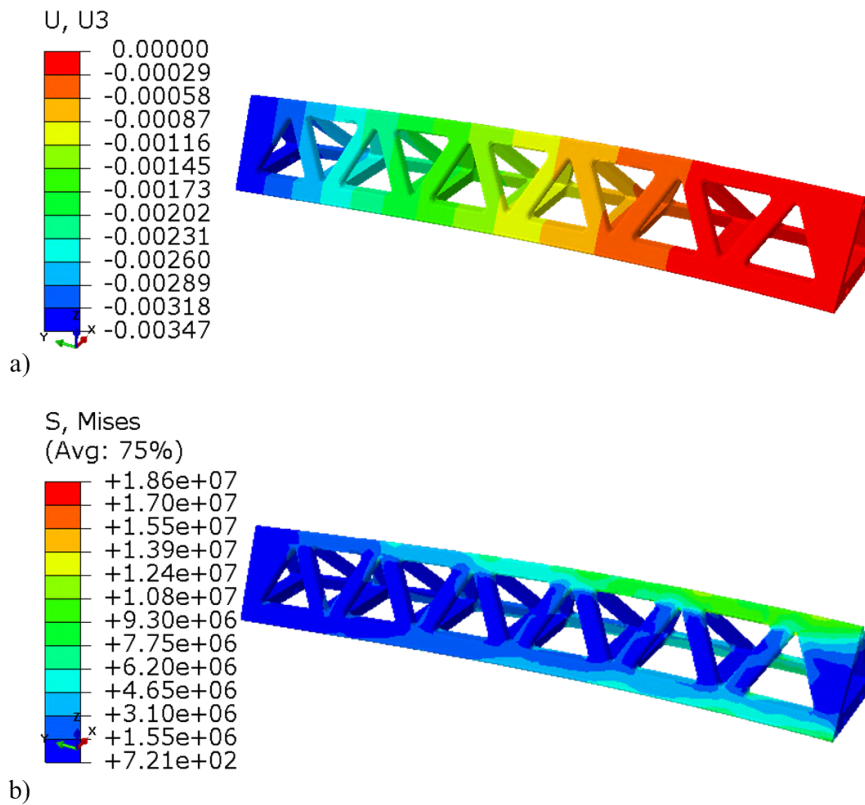


Figure 2-3: The distributions of displacement along Z-axis (a) and stresses (b) in manipulator link.

In addition to the stress-strain analysis we conduct the frequency analysis of the links using *finite element* (FE) method in CATIA to validate the absence of resonance oscillations. All calculated natural frequencies (Table 2.2) differ from the rotation frequency of the quadrotor motors, which is equal to 153.55 Hz (when motors powered from 22.2 V). The technical characteristics of the quadrotor motors are presented in Table 2.3².

| Manipulator components | Natural frequency, Hz | | |
|------------------------|-----------------------|--------|--------|
| | Pitch | Roll | Yaw |
| Link 1 | 87.74 | 304.61 | 106.47 |
| Link 2 | 66.12 | 270.04 | 85.21 |
| Gripper | 38.82 | 73.97 | 50.09 |

Table 2.2: Natural frequencies of manipulator components.

²E600 – DJI, available: <https://www.dji.com/e600/spec> (Retrieved October 02, 2020)

| | |
|-------------------------|-------------|
| Recommended Load | 600 g/axis |
| Maximum Thrust | 1600 g/axis |
| Voltage | 22.2 V |
| Stator Size | 35×8 mm |
| Motor velocity constant | 415 rpm/V |
| Weight | 90 g |

Table 2.3: Technical characteristics of motors of DJI E600 multicopter propulsion system.

2.3 Kinematic Model

We used inverse kinematics to calculate the desired position of the gripper and the possible geometric limitations of the manipulator. For VR-based teleoperation mode, we applied forward kinematics. At the calculation of the kinematics, we do not take into account the rotational degree of freedom of the grip since we are transmitting the desired angle directly to the servomotor controlling this DoF. Thus, we consider the kinematics of 3-DoF planar manipulator. Fig. 2-4 shows the scheme of the robotic arm. The abbreviations are as follows: θ , β , and α are the shoulder, elbow and wrist joint angles respectively; l_1 and l_2 are the link lengths; l_3 is the position of the grip end in relation to the wrist joint; (x_i, z_i) coordinate system (CoS) is attached to i -th CoS transformation; l_{dis} is the transition from CoS (x_2, z_2) to CoS (x_3, z_3) due to the shape of link 1; γ is the angle formed by the shape of link 1; T_1 , T_2 , and T_3 are torques in shoulder, elbow and wrist joints, respectively.

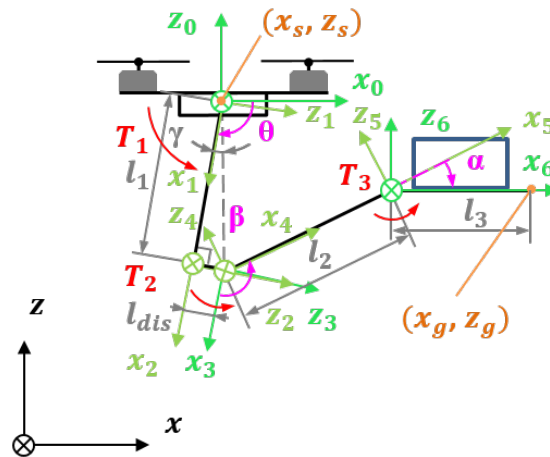


Figure 2-4: Scheme of the manipulator.

2.3.1 Inverse Kinematics

For the 3-DoF planar manipulator, we used the following transition matrix, which corresponds to the transformation from the CoS (x_5, z_5) to drone coordinates (x_0, z_0):

$${}^B_p T = T_5^0 = \begin{bmatrix} \cos(\phi) & -\sin(\phi) & 0 & x \\ \sin(\phi) & \cos(\phi) & 0 & z \\ 0 & 0 & 1 & 0 \\ 0 & 0 & 0 & 1 \end{bmatrix}, \quad (2.1)$$

$$\text{where } \begin{cases} \phi = \alpha - \beta + \theta \\ x = l_1 \cdot \cos(\theta) + l_2 \cdot \cos(\beta - \theta) - l_{dis} \cdot \sin(\theta) \\ z = l_1 \cdot \sin(\theta) - l_2 \cdot \sin(\beta - \theta) + l_{dis} \cdot \cos(\theta). \end{cases}$$

Using the VR controller, the gripper's DoFs are controlled by the touchpad (Section 3.3). Therefore, for the convenience of positioning the manipulator in relation to the target object during teleoperation, we calculate the position of α , so that the gripper will be parallel to the ground by default, but the operator can change this value directly if it is necessary for object grasping. To get expressions for calculating all joint angles, firstly, we calculate β (2.2) from (2.1). Secondly, using systems of equations (2.1) and (2.3) [Craig, 2009] we calculate θ and α :

$$\begin{cases} \gamma = \arctan(l_{dis}/l_1) \\ \cos(\beta) = \frac{x^2 + z^2 - l_1^2 - l_2^2}{2 \cdot l_1 \cdot l_2} \\ \sin(\beta) = \sqrt{1 - \cos(\beta)^2} \\ \beta = \arctan 2(\sin(\beta), \cos(\beta)) + \gamma, \end{cases} \quad (2.2)$$

$$\begin{cases} x = k_1 \cdot \cos(\theta) - k_2 \cdot \sin(\theta) \\ z = k_1 \cdot \sin(\theta) + k_2 \cdot \cos(\theta) \\ k_1 = l_2 \cdot \cos(\beta) + l_1 \\ k_2 = -l_2 \cdot \sin(\beta) + l_{dis}, \end{cases} \quad (2.3)$$

$$\begin{cases} \theta = -(\arctan 2(x, y) - \arctan 2(k_1, k_2)) \\ \alpha = \beta - \theta. \end{cases} \quad (2.4)$$

2.3.2 Forward Kinematics

We used forward kinematics to display the position of manipulator components in Unity. To do this, it is necessary to write the transformation matrix for each joint of the manipulator via rotation and translation matrices from the drone **CoS** (x_0, z_0) to each joint **CoS**. Thus, we got the following equations for position of elbow, wrist joints (2.5, 2.6) and the grip end (2.7):

$$\begin{cases} x_e = x_s + l_1 \cdot \cos(\theta) - l_{dis} \cdot \sin(\theta) \\ z_e = z_s + l_1 \cdot \sin(\theta) + l_{dis} \cdot \cos(\theta), \end{cases} \quad (2.5)$$

$$\begin{cases} x_w = x_e + l_2 \cdot \cos(\beta - \theta) \\ z_w = z_e - l_2 \cdot \sin(\beta - \theta), \end{cases} \quad (2.6)$$

$$\begin{cases} x_g = x_w + l_2 \cdot \cos(-\alpha - \beta + \theta) \\ z_g = z_w + l_2 \cdot \sin(-\alpha - \beta + \theta), \end{cases} \quad (2.7)$$

where x_s, z_s are the coordinates of the shoulder joint that corresponds to the current position of the **UAV**.

2.4 Dynamic Model

To estimate the servomotor loads of the manipulator, we created a dynamic model in Simulink (Fig. 2-5). For this purpose, we assembled simple visualization of the manipulator with the assignment of the mass of components (on the right side of the Fig. 2-5), then we connect this model with transfer functions of the servomotors and input data. The transfer functions (Fig. 2-6) were modeled for the most loaded servomotors MX-106T and MX-64T based on the dynamic models of Dynamixel motors proposed in article [Maximo et al., 2017]. This model takes into account almost all physical elements of the servomotor: PWM converter, DC motor, gearbox, inertia and friction of the components angular encoder. Changing the motor torques in the shoulder, elbow and the wrist joints in time is shown on the Fig. 2-7. In the initial and final positions, the manipulator is lowered down. From 38 to 42 seconds the manipulator operates in the position elongated in the front, in this interval the torques correspond to their maximum values. The angles for this simulation of the manipulator movement was obtained using IMU-based haptic interface (see Section 3.4).

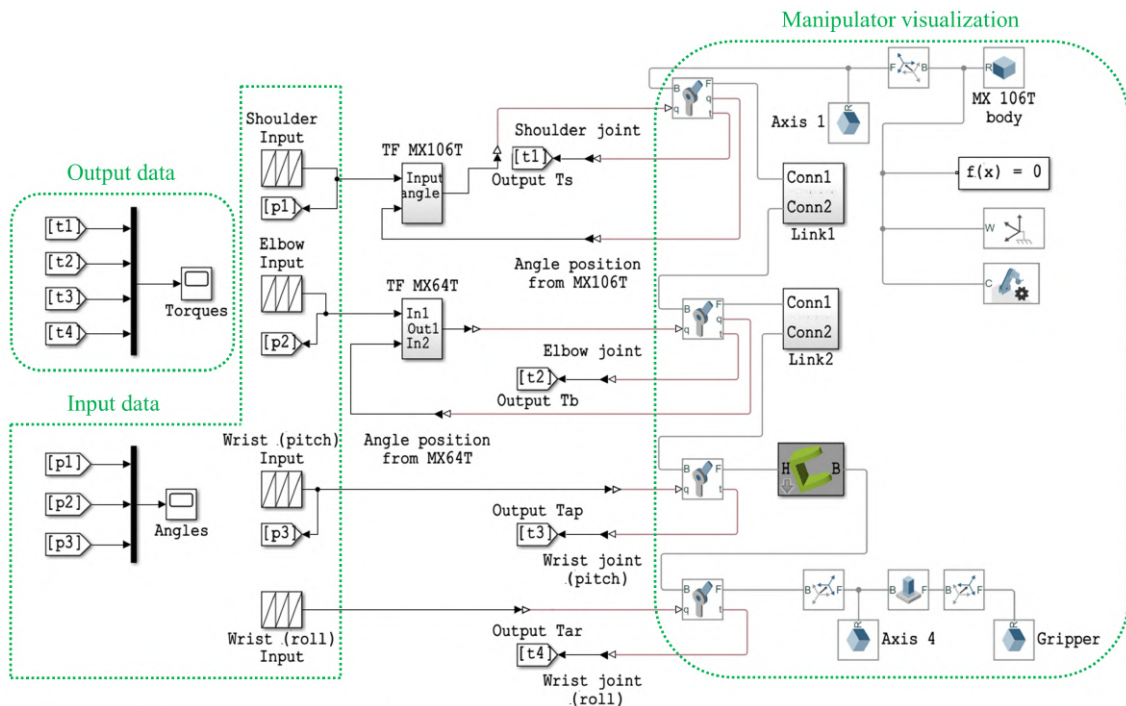


Figure 2-5: Block scheme of the dynamic model of 4-DoF manipulator.

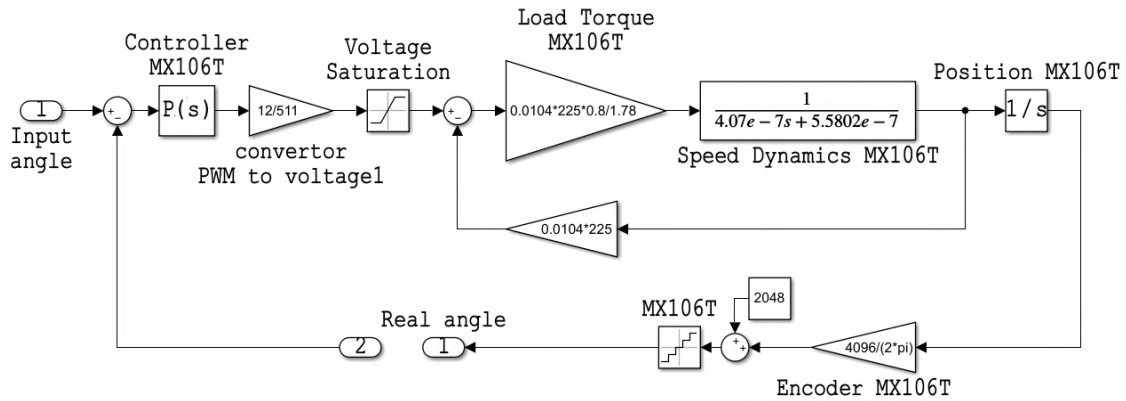


Figure 2-6: Block scheme of the dynamic model servomotor Dynamixel MX-106T.

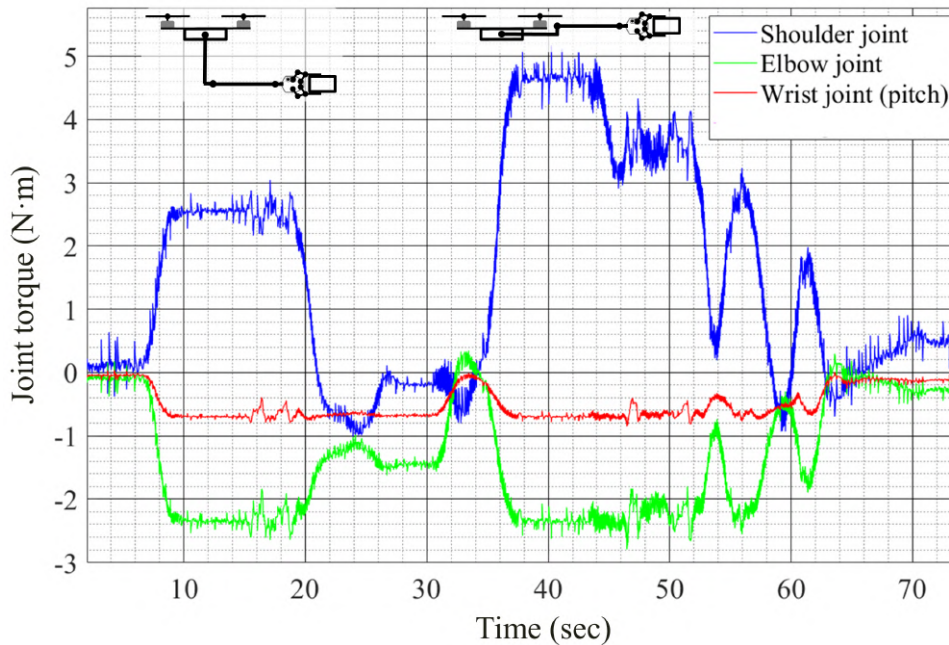


Figure 2-7: Simulation of the change in torque over time.

2.5 GUI for Manipulator Control

The connection of motors and sensors to MATLAB is performed via board OpenCM 9.04. Wireless control of the robotic arm is carried out by Bluetooth module HC-05. Adjustment of the control algorithm and monitoring the state of the robot is realized by the developed GUI interface in MATLAB (see Fig. 2-8). Using the GUI, we can conveniently configure the robot and observe the real-time manipulator behavior using a computer. In addition, we can send a command to

turn on (off) the manipulator power supply using the transistor switch. It is necessary if the behavior of UAV will become unstable.

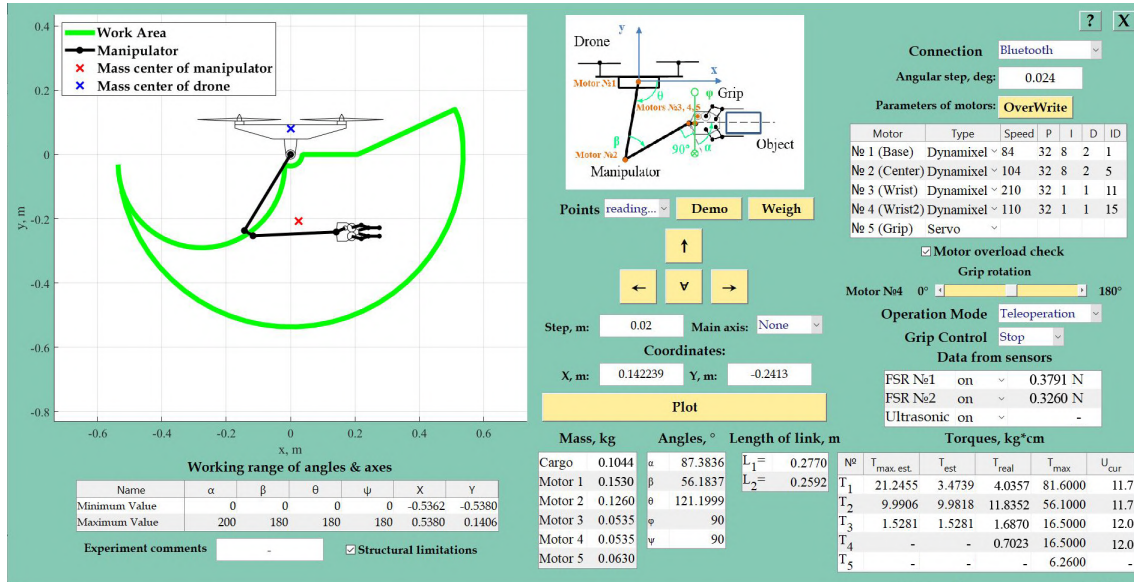


Figure 2-8: GUI to monitor the manipulator state.

Depending on the manipulator components, GUI provides information about the work area of the manipulator and the required torques of servomotors. It also displays information about the current technical parameters of servomotors (voltage, speed, PID coefficients) and sensor data (force resistive and ultrasound sensors). The user can change the following manipulator settings:

- Control modes of motors depending on the controllers: Arduino UNO, USB2Dynamixel or OpenCM9.04.
- Work area via changing the acceptable value of joint angles.
- Lengths of manipulator links.
- Types of the manipulator motors (ordinary servomotors or Dynamixel smart servomotors).
- Teleoperation and manual manipulator control modes.

In manual mode, the operator can change the position of the gripper by writing desired X and Y coordinates or pushing on the arrow keys (forward, back, up or

down). The step size is set separately for the usage of the arrow keys. Teleoperation mode switches the GUI to the mode of displaying and recording the experimental data, while control of the manipulator is transferred to Unity and the operator.

The application allows displaying the position of the manipulator in accordance with the current coordinates and the range of acceptable angles of servomotors. When the GUI starts, the verification of this range is performed in accordance with the specifying angles. After that, the manipulator's working area is calculated depending on physical limitations, such as the operating range of the servomotors and the positioning of the manipulator relative to the UAV propellers. Further, checking the entered coordinates is carried out in several steps. In the first step, we check whether the desired position is within the acceptable range of X and Y . In the case of fulfillment of this condition, the coordinates should be reachable in accordance with the lengths of the manipulator links (l_1 and l_2) and design features of the UAV. On the next step, the obtained angles are checked for being in the allowable range, which is specified by the operator. If the coordinates do not satisfy conditions, the manipulator movement will not occur, and GUI return the previous correct coordinates.

2.6 Experiment on Manipulation in Flight via GUI

The first test of the developed flying robot was carried out using GUI. In this flight tests we aimed to estimate the influence of manipulator movement on UAV deviations from the target position, and assess how the standard quadrotor autopilot (pixhawk) will react to dynamic load. The manipulator with grasped object is moved along the specified path (Fig. 2-9, Fig. 2-10(a)). In point No. 9 the operator sends a command to release the object. A wooden cube weighing 77 grams was used as an object for this experiment.

Fig. 2-10(c) shows that the maximum deviation of the roll angle is of 5.22 degrees (standard deviation is of 0.99 degrees). The fluctuations in the roll direction in the range of points 3 to 9 arise due to the fast manipulator movement with a considerable distance. The standard deviation of pitch angle is of 3.51 degrees, the maximum

pitch error of 9.38 degrees (see Fig. 2-10(d)) occurs when the manipulator is moved along one of the coordinates about 0.2 m, which is accompanied by a significant change of the servomotor torque in the elbow joint.

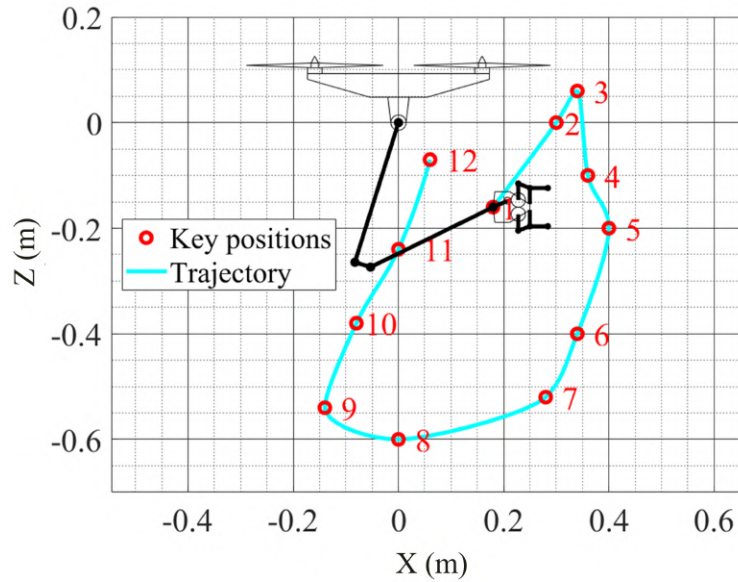


Figure 2-9: The trajectory of the wrist joint position during experiment.

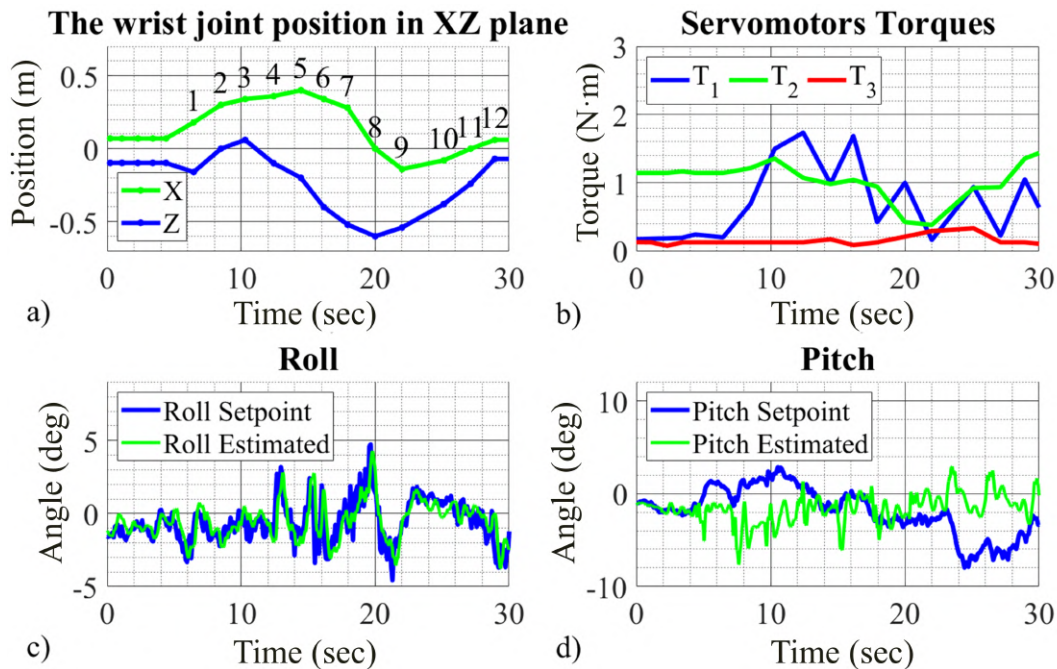


Figure 2-10: Dependencies of target coordinates (a) and motor torques (b) of the manipulator, roll (c) and pitch (d) angles from the experiment time for the flight test with the GUI teleoperation.

2.7 Concluding Remarks

The developed manipulator has competitive characteristics with existed aerial manipulators (Table 2.4). The manipulator has an increased payload and the greatest length among those considered. The length of the robotic arm allows interacting with objects directly in front of the robot. However, stretching the arm increases the dynamic load on the UAV's propulsion system, so it is worth interacting with objects no more than 0.2 kg in extended manipulator position. Our lightweight manipulator was designed applying truss structure at designing of the manipulator links. The stiffness of the links was calculated under the static effect of the maximum load using the finite element method. When the robot crashes during some flight tests, the robot fell on the robotic arm, but the manipulator practically did not get damage due to the preliminary calculation of the dynamic loads and the modular design. It is worth noting that the developed manipulator does not have a rotational DoF in the shoulder joint to perform rotation around the Z-axis of the quadrotor. If necessary, rotation around this axis is carried out by controlling the yaw orientation of the UAV, also the robot can move sideways using the translation DoF of the UAV. The wrist joint of the robotic arm has 2-DoF for better interaction with objects located randomly in the space.

| Reference | UAV type | Number of joints | Manipulator length (mm) | Weight/Payload (kg) |
|-------------------------|-----------------------|------------------|-------------------------|---------------------|
| Developed | quadrotor | 4 | 740 | 0.918/0.4 |
| Chen et al. [2019] | X8 coaxial octocopter | 4 | 419 | 0.545/0.2 |
| Suarez et al. [2018] | hexarotor | 4 | 500 | 0.65/0.2 |
| Bellicoso et al. [2015] | quadrotor | 5 | 300 | 0.25/0.2 |

Table 2.4: Comparative table of existing aerial manipulators.

We have developed a GUI for manipulator adjustment and control. This application is universal for manipulators of this configuration, which differ in the length of the links and the mass of the components. We controlled the manipulator movement using the application during the robot's flight. The flight tests of the developed robot showed a stable UAV behavior while manipulation by the grasped object. The average deviations in pitch and roll were 3.51 and 0.99 degrees, respectively.

In the framework of the AeroVR project, the manipulator movements were smooth at a low speed in the range from 0.08 to 0.2 m/s (Subsection 3.9.1). The motors of the propulsion system rotated at a speed of 9153 rpm. We performed the frequency analysis of manipulator components to prove the absence of resonant oscillations, which could destabilize the system during manipulation. It is also worth noting that the stability of the robot's functioning has been confirmed empirically. The robot did not crash even if the robotic arm was quickly moved from the lower position to the extended position during the laboratory testing. We experimentally tuned the PID coefficients of the Pixhawk autopilot to compensate for disturbances caused by the displacement of the robot CoM during the aerial manipulation. The proportional gain value of the speed controller has been slightly lowered and the integral gain value has been increased.

For a qualitative consideration of stability, it is necessary to use nonlinear control methods. For this goal, it is necessary to create a detailed mathematical model (e.g., in Simulink), taking into account all physical properties of all robot components. It can be one of the subjects for future work. For example, the doctoral dissertation of Roberto Rossi [Rossi, 2017] is dedicated directly to the control of an UAV equipped with a robotic arm (that is the name of the thesis). The stability of the system is demonstrated by utilizing the Lyapunov analysis. The controller of this robot was designed based on inverse dynamic controller with pre-impact control strategy.

Chapter 3

VR-based Teleoperation System for Aerial Manipulation

3.1 State of the Art

For the implementation of industrial maintenance, assistance in rescue operations in an unstructured environment, we can formulate two most important tasks for performing aerial manipulation. Firstly, the robot should carry out various specific tasks with high accuracy that may not always be performed in autonomous mode. This function can be achieved with teleoperation. Secondly, the robot and the operator are often located in remote places, which is especially important for hazardous conditions.

One of the solution for inspecting industrial facilities via teleoperation is proposed by team of the European project AEROARMS. [Suárez et al. \[2018\]](#) designed a hexarotor platform equipped with a 2-DoF compliant joint arm which is controlled by a wearable exoskeleton interface via visual feedback. The proposed method provides variability of the manipulation tasks, but the exoskeleton is a bulky mechanism, that can constrain the movement of the operator. In [\[Coelho et al., 2019\]](#) researchers tested Novint Falcon haptic device for teleoperation of a SAM [\[Sarkisov et al., 2019\]](#) in simulation using Time Domain Passivity Approach based drift compensation methods. The results of the numerical simulation showed round-trip time delays up to 700 ms. As was mentioned in [Section 1.1](#), applying VR provides a com-

comfortable perception of the situation around the robot, what can be improved with tactile feedback. Naceri et al. [2019] proposed VR-based teleoperation interface with additional visual feedback from the camera mounted on the robot, that provides the immersive control and freedom of viewpoint selection. In this research, the developers noted the communication latencies between system components, and it is also not suitable to use with haptic feedback. We can summarize, that at performing tasks of the aerial manipulation, the operator is faced with the following challenges: operator is visually overloaded to find the target object in a real environment and to control the robot at the same time, also, there is no comfortable wearable and intuitive interface to perform the various aerial manipulation tasks.

In paper [Isop et al., 2019] authors developed a teleoperation system for exploration and indoor navigation in structured spaces by micro UAV. A key technology of this system is the automated processing of information during the indoor exploration missions and designation of critical objects of interest. This functional of the teleoperation system was substantiated by the need to reduce the time required by the operator for a qualitative assessment of the situation surrounding the UAV. Besides increasing the efficiency of the mission, the authors set a goal to reduce the information load on the operator. For this goal, they developed a multi-view GUI, which consists of a traditional egocentric scene view, an exocentric scene view, and a complementary topological graph view of the scene. The exocentric scene view was represented as grid-map representations. In addition, the comparison of the developed system with the usual system with traditional joystick control was carried out via user study. To control UAV participants used the usual computer mouse.

The system [Isop et al., 2019] undoubtedly has advantages over the conventional indoor exploration using radio equipment and an on-board camera, since the developed system provides the operator with extended information by a map and marking critical objects on it. However, it should be noted that using a mouse significantly limits the robot's flight control capabilities. In the mentioned article, the operator can only give 3 commands for the robot; these are "explore", "inspect", and "navigate". The authors put forward a hypothesis about increasing the efficiency of the exploration due to the usage of a simple topological graph, which contains only basic

information about objects and passageways between rooms. But at the same time, the designed GUI has three screens of the same size, one of which is a detailed map of the room, updated in real-time. Thus, the operator remains free to choose the concentration on one of the three views, while the authors could choose one of them as the most important or highlight a part of the user study to determine the most informative view. Perhaps it was more rational to use a simplified contour map combined with a graph. Based on research findings of the study of the human-robot interaction [Yanco et al., 2004] the GUI for the remote control of the mobile robots must meet the following requirements: availability of a map, critical information from robot sensors (a charge, speed, and others), minimizing the usage of multiple windows, spatial information about the surrounding environment, the ability to switch control methods when performing various operations.

Particular attention should be paid to developments dedicated to the control of complex robots, consisting of a mobile platform (e.g., wheeled or tracked chassis, UAVs) and a robotic device for performing specialized tasks (e.g., manipulator). Most often, bilateral teleoperation is used to control such robots [Andaluz et al., 2016, Santiago et al., 2019]. Andaluz et al. [2016] used Falcon haptic device, Leap Motion, VR and augmented reality to control the wheeled platform equipped by the manipulator. The haptic device provides robot position control and force feedback to feel the approach to obstacles. The camera located on the manipulator end-effector transmits video and audio stream to thy HMD. Leap Motion was used to interact with a menu of virtual or augmented reality applications, and also to switch between these applications. In this paper designed comfortable GUI in Unity3D, which provides the operator with the necessary information to successfully control the robot. However, the proposed control method does not imply simultaneous control of the movement of the mobile platform and control of the manipulator. The usage of one haptic device is intended to operate in two modes: locomotion and manipulation.

The authors of the article [Pepe et al., 2016] proposed control using a single haptic device to control an omnidirectional mobile platform with a robotic arm. In this paper Phantom Omni device is used as a master device, the volume of which

workspace is approximately a portion of a sphere with a variable radius. The authors divided the working sphere into three areas with different concentric radii. These three workspaces were defined as grasping (central), transition, and navigation (external) areas. The position-position and position-velocity controllers were used for the teleoperation of the manipulator and mobile platform, respectively. This approach for controlling multifunctional robots by one master device is attractive, but the authors did not conduct a user study to assess the usability of the proposed method. Perhaps, not every operator will be able to use this type of control effectively. In addition, the authors did not take into account the possibility of stopping the teleoperation process in the event of unforeseen situations.

Valner et al. [2018] tested the remote teleoperation system, which consists of Leap Motion for gestural commands, microphone speech input, and mixed-reality scene. A rotational knob maps operator input to the task's scale. This device provides comfortable control of both the movement of the mobile platform for several meters and the manipulator control with an accuracy of 1 mm. The mixed-reality scene combines the model-based representation of the robot's current state with a lidar-based map. Also, the scene contains visual cues representing the motion constraints of the robot. The authors emphasized that the usage of HMD can improve the way the operator perceives the robot and task space and allow more intuitive to control point-of-view. The position control is based on the implementation of predetermined command, such as "navigation" and "manipulation". The hand gestures are interpreted as a virtual pointer for commanding the position of interest, but the Leap Motion has a small workspace, as was mentioned in Section 1.1. The aforementioned functions do not provide the operator the ability to switch to full control by the manipulator that excludes the possibility of performing more complex operations. Nevertheless, the simultaneous use of visual, verbal, and tactile control can significantly expand the functionality of remote control of robots.

The operator interface is a combination of input/output devices and the integrating software often evaluated quantitatively using task-specific metrics: completion time, latency, training time, success rates; and qualitative evaluations of the provided situational awareness, required cognitive load and user experience [Valner

et al., 2018]. The paper [Murphy and Schreckenghost, 2013] contains the metrics for the process of human-robot interaction based on analysis of the 29 papers. The authors categorised 42 metrics measuring human (H), robot (R), and systems (S). Among them, we can highlight training time (H), situation awareness (H), performance of the predetermined algorithms (R), time ratio of autonomous and manual modes (R), productivity (S), efficiency (S), reliability (S), safety (S), and coactivity (S) which are most important factors at the design of the teleoperation system for aerial manipulation. The number of successful attempts can be used to assess system productivity. The efficiency can be measured by the time of preparation for the task and the time of execution itself. Reliability can be defined by false alarms, system flexibility to changing working conditions, and time in unscheduled manual operations. The safety metric is the risk to destroy the robot or damage expensive equipment (e.g., at the industrial maintenance). Coactivity subdivision has the following metrics: cognitive interaction (information exchange, information assessment, decision and action selection, inherent lag, command specification), percentage of requests for assistance made by a robot, percentage of requests for assistance made by the operator, and task allocation [Murphy and Schreckenghost, 2013].

Our developed teleoperation system (Fig. 3-1) is aimed at accurate object manipulation by the UAV equipped with a 4-DoF robotic arm in a remote environment without direct visual contact between a human operator and flying robot. This goal is achieved by the development of the teleoperation system based on the VR environment. For this, the robotic arm attached to the quadrotor is capable of reproducing human hand movements. For the implementation of this function we used a commercial VR controller, a combination of the developed smart glove with commercial VR trackers, and two wearable interfaces designed by us. At the same time, the robot flight is managed by HTC VIVE controller with visual feedback from the camera mounted on the manipulator. For a better perception of the current state of the robot and the environment surrounding it, a digital twin of the robot and live video from the camera located on the end effector are projected into HMD. In addition to visual feedback, the operator receives information about the distance between the inner part of the gripper and an object opposite the manipulator. Also, the system

provides an operator with the tactile feedback, informing whether the target object is grasped. Proposed teleoperation system allows an operator to manipulate remote objects successfully after short preliminary training.



Figure 3-1: The flight test of the aerial manipulation. a) Robot during teleoperation. b) VR visualization in Unity. c) Operator with HMD and wearable interface.

3.2 System Overview

For the teleoperation of the the flying robot with 4-DoF manipulator (Fig. 3-1 (a)) we develop a VR system that consists of VR application (Fig. 3-1 (b)), HMD and wearable interface (in Fig. 3-1 (c) the smart glove with HTC VIVE trackers are used as wearable interface). We used the position-position and position-velocity control scheme to control the manipulator and UAV, respectively. Position-position control is widely used to perform teleoperation tasks requiring object manipulation in remote environments. The manipulator control scheme is based on an inverse (VR controller) and direct (wearable interface) kinematics mapping between master and slave devices. The movement of the right hand holding the HTC VIVE controller is

converted to drone position and orientation commands (flight control device is not shown Fig. 3-1 (c)). The manipulator control device transfers the position (in the case of VR controller operation) and the orientation of the operator's hand (in the case of IMU-based wearable device operation) to the VR application designed with the Unity engine, which sends target angles to the robot manipulator. The position-velocity scheme is suitable in case of the robot control in an infinite workspace, but this type of control is less intuitive when small displacements are required. The glove controls the closing of the grip and provides feedback to the operator via vibration motors when the gripper bars interact with an object. For verification of the whole developed system, we tested the VR teleoperation of aerial manipulation using Mocap, which provides localization data of the robot and object. The VR setup includes HTC Vive Pro base stations, HMD, joystick.

The issue of choosing the convenient viewing angle for teleoperation is one of the most important. For the real experiment (Section 3.8) in laboratory conditions (room with an area of 5 by 5 square meters), we used a Mocap, which provides the precise positions of the robot and object. In this case, the operator could change his position in the room and inspect the robot from a comfortable viewing angle. For this purpose, the operator should use the UAV controller to switch to the mode of the holding position in order to disable control of the robot's body movement temporarily. Similarly, the operator could freely choose a viewpoint during the first user study (Subsection 3.9.1). In the second user study (Subsection 3.9.2), we experimentally selected a convenient view for controlling the robot in a simulated environment. It is a third-person view, slightly behind the robot and slightly higher. This field of view is realized by binding the HMD coordinate system to the robot's center with some offset.

The third-person view allows the operator to see the whole robot when controlling its robotic limbs. The operator must be fully aware of the robot's size that the robot does not collide the robot into potential obstacles. If necessary, this function can be accomplished without the third-person view using additional algorithms and tactile feedback, giving an auxiliary signal (for example, vibration or a light signal in the VR interface) that the desired position is unattainable. However, a convenient field

of view provides more useful information about the surrounding environment. Using only a first-person view for aerial manipulation is generally insufficient for successful robot control. When the camera is only installed on the robot body, the operator can not grab the target object. If the camera is installed on the gripper, the operator can be disoriented at the manipulator moving and especially at the turning the gripper along the roll direction. Thus we used a camera on the gripper as an additional source of information useful for grasping operation.

3.3 Manipulator Control with the VR controller

The manipulator control is carried out through the inverse kinematic using the position of VR controller as the input parameters. We engaged all the functionality of the controller buttons to operate the necessary components of the system (Fig. 3-2). Before the start of the teleoperation process it is required to perform an initial calibration since each operator has a unique height and the arm's length. For this purpose the operator should touch the shoulder by the hand holding joystick and press the Menu button on the controller. The calibration provides the origin point

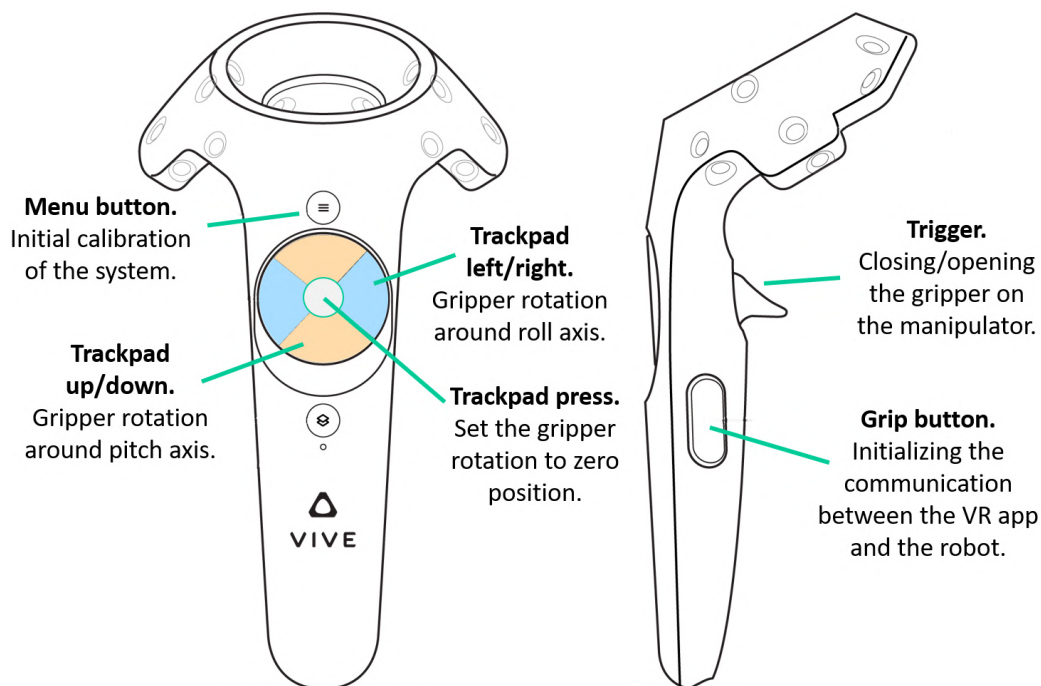


Figure 3-2: Input buttons of the VR controller using for the manipulator control.

relative to which the operator's hand movements with a joystick is transformed into the manipulator movement. The trackpad is used for changing the gripper rotation along roll and pitch axes. Besides, we added the opportunity to set the gripper rotation to zero position by pressing the center of the trackpad. The trigger on the controller is used for opening and closing the gripper of the manipulator. The communication between VR system and robot with manipulator initialized by pressing the Grip button on the controller.

3.4 Wearable Teleoperation Interfaces

To control aerial manipulator we developed three type of the wearable haptic interface, these are a smart glove with HTC VIVE trackers, an interface with IMU and flex bending sensors, an IMU-based interface (see Fig. 3-3).

3.4.1 Smart Glove

The design of the tracking glove was inspired by the glove of Chan et al. [2018]. They tested the glove equipped with Inertial Measurement Unit (IMU) and flex sensors. Our glove for grip control consists of the fabric glove, 5 embedded flex sensors, IMU sensor, coin vibration motors, battery, and control electronics (Fig. 3-3 (a)). Five spectra symbol flex sensors 4.5 allow measure average flexion angles of fingers that directly controls the opening/closing of the gripper. IMU sensor AltIMU 10 v4 determines the rotation of the hand in space (angles of the wrist joint). We sewed 5 vibration motors into the glove at the fingertip areas that allows transferring the feedback about the interaction of the manipulator with the grasped object. The usage of the vibration motors on the fingertips to get feedback from the micro UAVs was proposed in the paper [Labazanova et al., 2018]. Control of sensors and vibration motors is performed via Arduino Nano. The data exchange between the microcontroller and computer is carried out by Bluetooth module HC-05. The assembled electrical circuit is powered by a 7.5V Li-Po battery via DC-DC converter MP1584EN.

The developed glove has been supplemented with HTC VIVE trackers, which

were attached to the arm for tracking the user's hand motion. The first tracker is mounted on the shoulder to control the rotation of the shoulder joint of the manipulator. The second tracker is fastened around the elbow joint and aimed to control the elbow joint rotation of the manipulator. Experimentally we defined the optimal position of trackers, which provides the largest work area of the elbow and shoulder joint angles of the operator's arm.

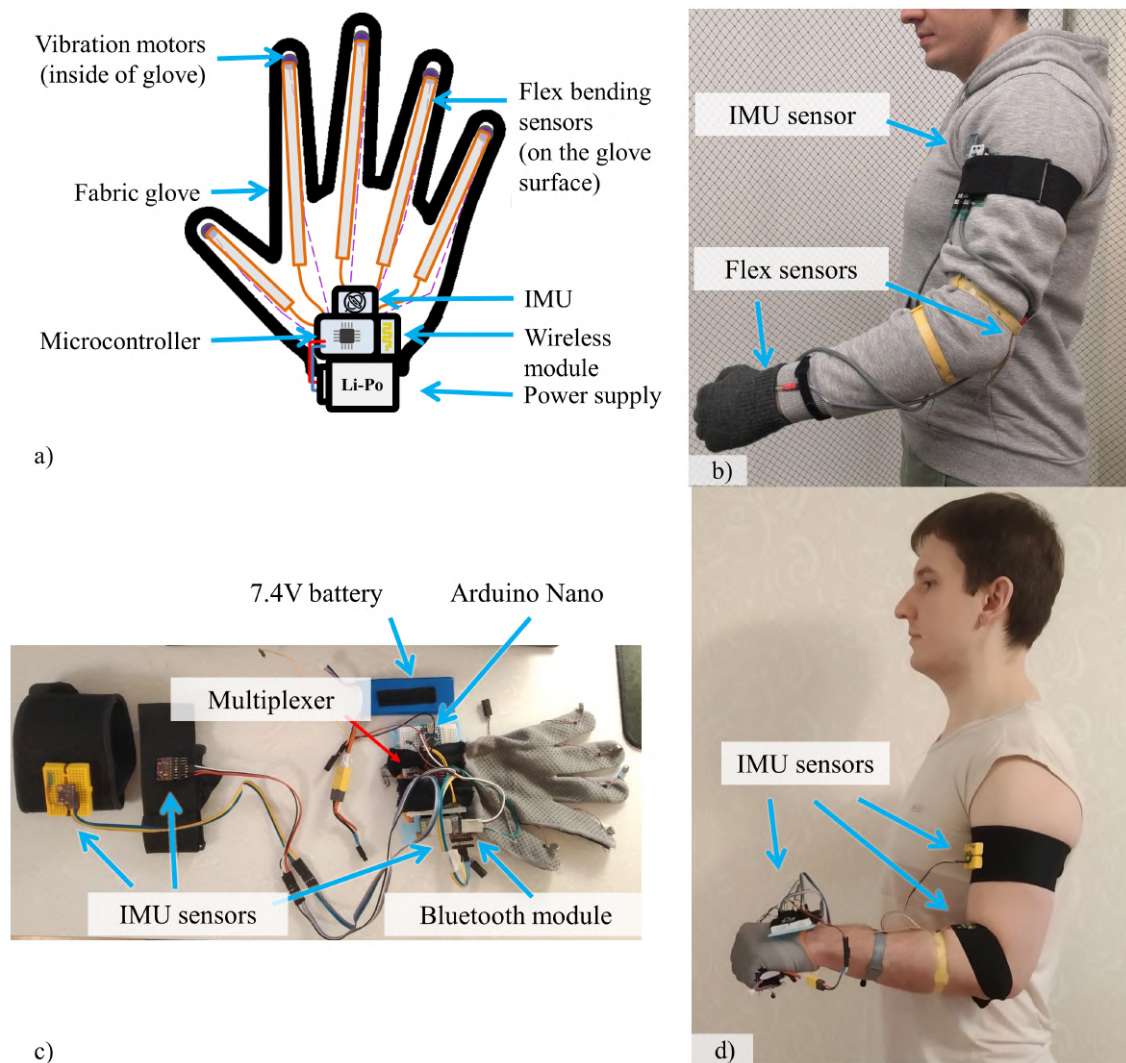


Figure 3-3: The scheme of the smart glove (a), pictures of an interface with IMU and flex bending sensors (b), components of the IMU-based haptic interface (c) and the location of the interface on the arm (d).

3.4.2 IMU-based Wearable Interface

IMU-based wearable interface includes 3 IMU sensors GY-91 controlled by Arduino Nano with usage multiplexer TCA95448A. The data exchange between these components is carried out using I2C protocol with usage library for IMU sensors¹. Raw data from the sensors are very noisy, therefore we applied a Madgwick filter² [Madgwick, 2010]. In the Fig. 3-4 are shown dependencies of the unfiltered (a) and filtered (b) values of the joint angles from time.

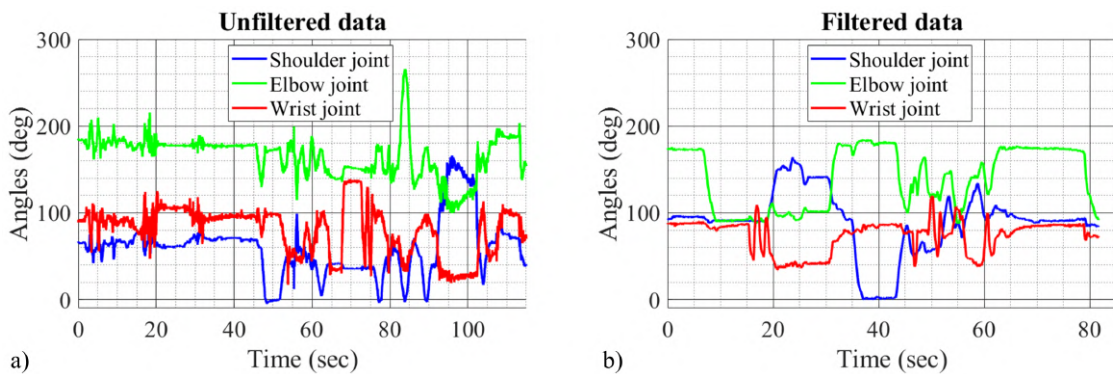


Figure 3-4: Unfiltered (a) and filtered (b) data from the IMU sensors.

The smart glove is also part of the wearable interface. The difference from the first version is in the usage of two flexible sensors (instead of five in the first design) since there is enough data from them to control the opening/closing of the gripper. Also, the second version of the glove was also made compact, despite the expansion of functionality by the connection of three IMU-sensors. IMU-based haptic interface is shown in Fig. 3-3 (c, d), the electrical circuit of this interface is presented in Appendix A.

3.4.3 Interface with IMU and Flex Bending Sensors

The third solution for the teleoperation consists of 10-DoF Troyka IMU sensor located on the shoulder, two flex bending sensors to obtain data about elbow and wrist position, and flex bending sensor to control gripper. The data obtained from

¹MPU6050_tockn, available: https://github.com/tockn/MPU6050_tockn (Retrieved June 16, 2020)

²TroykaIMU, available: <https://github.com/amperka/Troyka-IMU> (Retrieved June 16, 2020)

this haptic set are shown in Fig. 3-5. This wearable interface also allows collecting data of changes in joint angles without significant noise. However, the usage of single flex sensors in the elbow and wrist joint restricts the range of measured angles from 0 to 180 degrees. This problem was solved using dual sensors in joints, but in this case, there remains the necessity of their accurate positioning on the elbow, as well as a limited service life due to regular bending at an acute angle. At the stage of testing the prototype of this wearable interface, we determined that the individual structure of each person’s hand significantly affects on the reading of the angle value from the sensor located on the operator’s elbow. In this regard, we had to abandon the tests of this device to control a real manipulator in the framework of the user study.

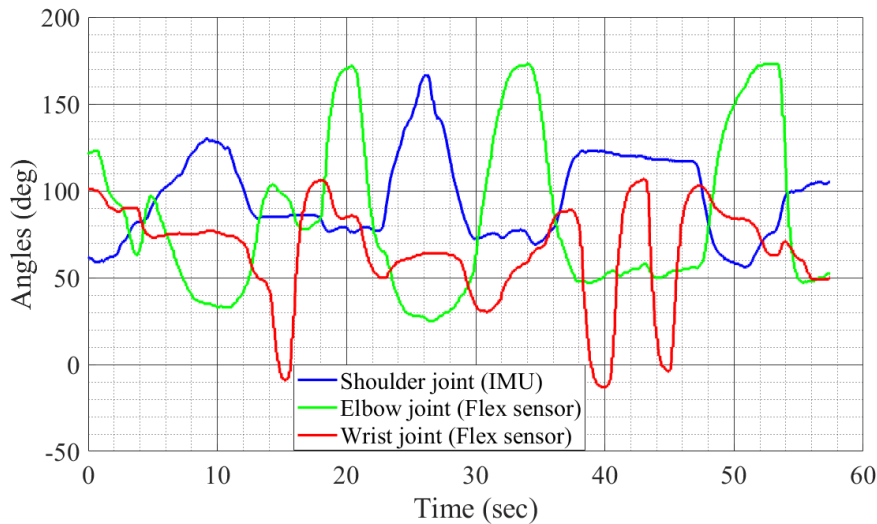


Figure 3-5: Data from the interface with IMU and flex bending sensors.

3.5 Control of the UAV using a VR Controller

The position and orientation of the VR controller are estimated with HTC Vive base stations (which can be replaced with any positioning system). To control UAV we modify the algorithm proposed in [Tsykunov et al., 2019]. Four parameters of the state of this controller (x_c, y_c, z_c, yaw) are used to calculate four control inputs

(V_x, V_y, V_z, α) in order to control 4 DoF of the UAV, according to:

$$\left\{ \begin{array}{l} \begin{bmatrix} V_x \\ V_y \\ V_z \\ \alpha \end{bmatrix} = K_v \begin{bmatrix} -(x_c - x_0) \\ y_c - y_0 \\ z_c - z_0 \\ yaw - yaw_0 \end{bmatrix} \\ |x_c - x_0| > d_{min} \\ |y_c - y_0| > d_{min} \\ |z_c - z_0| > z_{min} \\ |yaw - yaw_0| > yaw_{min}, \end{array} \right. \quad (3.1)$$

where V_x, V_y, V_z are the global velocities for the UAV; α is the target yaw angle of the UAV; K_v is the vector of scaling coefficients which determines the control sensitivity; x_0, y_0, z_0, yaw_0 are the initial position of the VR controller; $d_{min}, z_{min}, yaw_{min}$ are threshold values that filter noise (tiny movements around target position).

System of equations 3.1 describes, how displacement of the VR controller is mapped to desired UAV movements. Controlled UAV reacts to the controller position and orientation change in the following way. If the VR controller is moved to the side (forward, backward, left, or right), the controllable drone is commanded to change its velocity $[V_x, V_y]^T$ in horizontal plane, proportionally to controller's displacement in accordance with the 3.1. It is also important to introduce lower boundaries ($d_{min}, z_{min}, yaw_{min}$ in the 3.1) on the VR controller movements, since its orientation is not always static. Coefficient K_v controls how much controller's position change affects on UAV velocities. The guided UAV's position set-points are derived from the commanded velocity as follows:

$$\begin{bmatrix} x_t \\ y_t \\ z_t \end{bmatrix} = \begin{bmatrix} x_{t-1} \\ y_{t-1} \\ z_{t-1} \end{bmatrix} + dt \begin{bmatrix} V_x \\ V_y \\ V_z \end{bmatrix}, \quad (3.2)$$

where (x_t, y_t, z_t) and $(x_{t-1}, y_{t-1}, z_{t-1})$ are the UAV positions in current and previous

time, respectively.

3.6 UAV Localization

The external position estimation system is used to localize the UAV during the flight. In order to get the high-quality tracking of the quadrotor and a target object during the experiments, we use VICON Motion Capture System (Mocap) with 12 cameras (Vantage V5) covering 5 m x 5 m x 5 m space. ROS Kinetic framework is used to run the development software and Mavros ROS stack for drone control and ground station communication. Connection between client computer and drone's onboard computer is established using the Vicon-bridge ROS package.

The position and attitude update rate for the quadrotor and the target object is 100 Hz. The estimated poses of the tracked robot and object are sent to the computer running Unity 3D software for VR simulation. While the main goal of the experiment is to manipulate an object in virtual and real environments at the same time, the quadrotor is commanded to give in place holding its position close to the object (in this position, the object is located within the robotic arm's manipulation area). During the aerial manipulation, the robot position is corrected by a UAV operator in order to prevent high oscillations around the desired location of the robot.

3.7 System Communication

The principle system communication flowchart is shown in Fig. 3-6. This system consists of a client computer with Unity, the manipulator control device, HTC VIVE controller, Mocap positioning system, the flying robot represented by an on-board single-board computer, a Pixhawk flight controller, and a manipulator. The Client computer with Unity receives control inputs and drone local position from the control devices of the operator through a Bluetooth connection and Mocap positioning system through an Ethernet cable, respectively. The connection between

Mocap and VR application is performed using the Vicon plugin for Unity³. Client and drone's onboard computers are working in the same Wi-Fi local network and are connected via ROS multimaster network. Onboard computer is connected to the Pixhawk flight controller through Telem2 port (using USB-UART connector). Through a Wi-Fi connection onboard computer on the robot receives two sources of data: position and yaw orientation from the HTC VIVE controller and drone's local position from Mocap. A dedicated ROS node parses them and sends to the flight controller using the Mavlink communication protocol. Control inputs are sent to the robot through the sockets interface via TCP protocol. The same principle is used in the transmission video from the camera, installed on the gripper, to Unity.

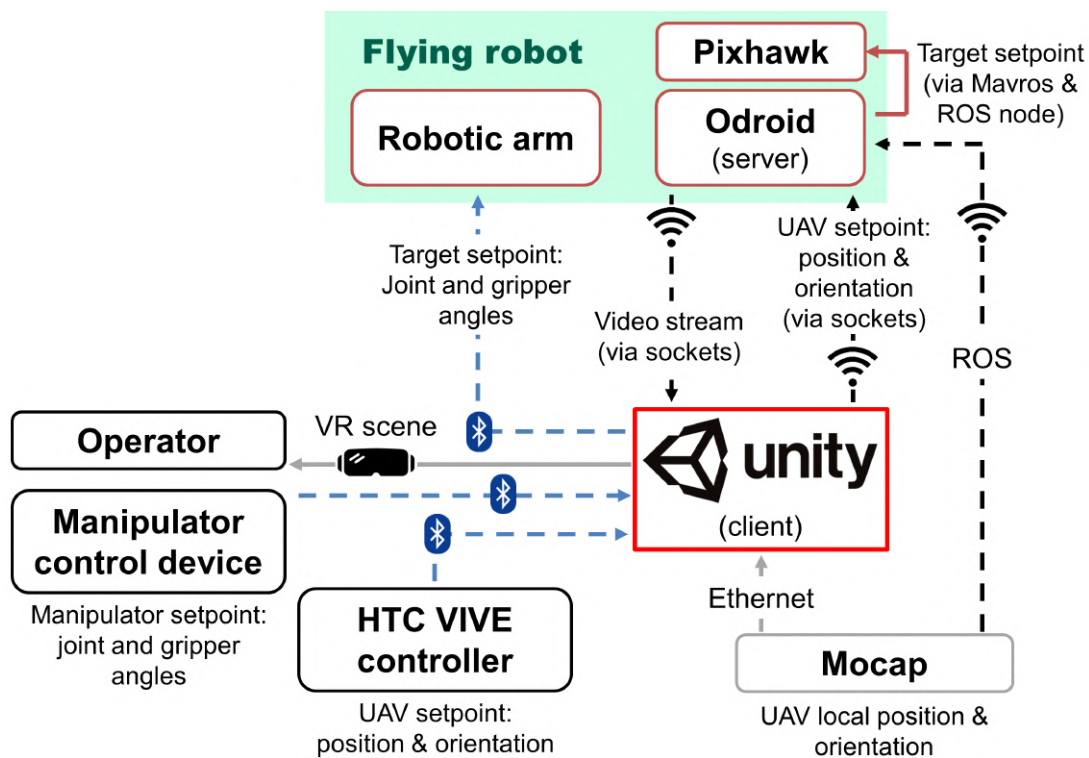


Figure 3-6: The principle scheme of communication of the VR-based teleoperation.

³Unity Plugin 1.2 Documentation, available: <https://docs.vicon.com/display/UnityPlugin12/Install+and+set+up+the+software> (Retrieved March 20, 2020)

3.8 Experiment of Manipulation Control in Flight

Initially, we conducted an experiment on manipulator control during a flight to evaluate the performance of a remote control system using VR on a real robot. For this purpose, the robot took off and was in the mode of the position holding. At this time, the operator controlled the movement of the robotic arm using the smart glove with HTC VIVE trackers. Video clip containing a demonstration of the experiment can be found at the following link: https://youtu.be/_RK1fm7CaTY.

3.8.1 Description of VR Setup

The VR setup includes HTC Vive Pro base stations, HMD, and trackers attached to the arm for tracking the user's hand motion in VR. During the flight tests smart glove with HTC VIVE trackers was used to control manipulator motion. The first tracker is mounted on the shoulder to control the rotation of the shoulder joint of the manipulator. The second tracker is fastened around the elbow joint and aimed to control the elbow joint rotation of the manipulator. Experimentally we defined the optimal position of trackers, which provides the largest work area of the elbow and shoulder joint angles of the operator's arm.

For the flight tests we used simplified communication system, which did not include the control of the UAV by the operator. Fig. 3-7 contains the scheme of communication among Mocap, ROS, Unity, the flying robot with manipulator, and the operator. Unity application is the core part of this system, which receives the data from the operator and the robot through a Bluetooth connection and from ROS through a cable. Also, Unity sends the necessary commands to the devices in accordance with predefined scripts. To provide the user with visual feedback, the operator wears HMD to experience VR environment, which includes a simplified model of the room along with a flying robot (see Fig. 3-8). Mocap cameras transfer position and rotation data of each tracked object to the Unity 3D engine. The connection between Mocap and VR application is performed using the Vicon plugin for Unity⁴. In addition, data from the manipulator are transmitted to the GUI.

⁴Unity Plugin 1.2 Documentation, available: <https://docs.vicon.com/display/>

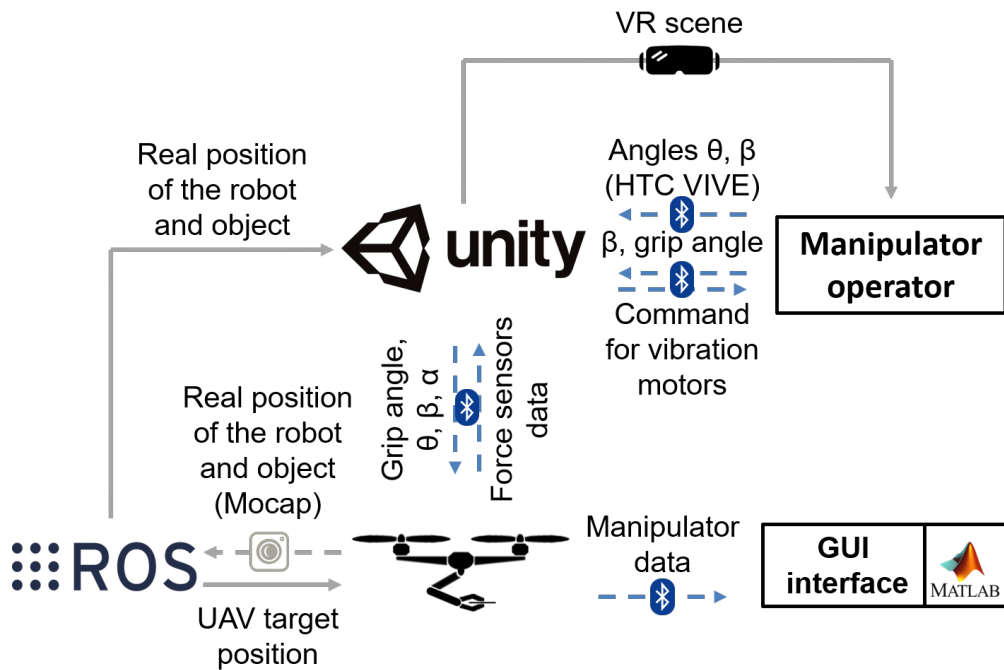


Figure 3-7: The scheme of communication for the flight experiment.

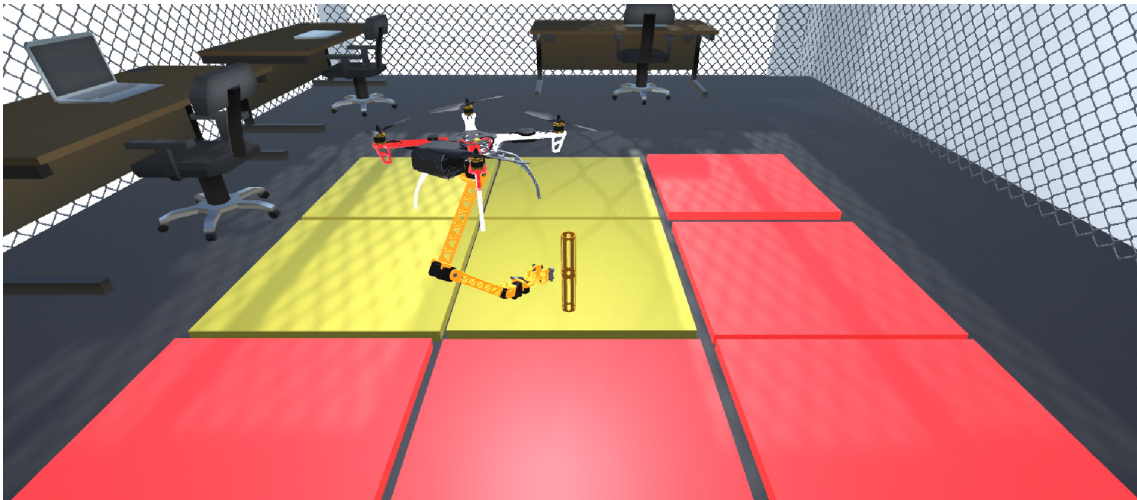


Figure 3-8: Digital twin of the room for the experiments on aerial manipulation.

The work space for testing the teleoperation system consists of two rooms (Fig. 3-9). The first room, where the aerial manipulation is carried out, is equipped with *Mocap* cameras. In addition, the *UAV* operator with a radio remote control is present in this room to eliminate unforeseen high oscillations around the target position. In the second room, we installed HTC VIVE equipment and base station [UnityPlugin12/Install+and+set+up+the+software](#) (Retrieved March 20, 2020)

(computer with Unity application). The operator can freely move his or her hand on which the trackers and glove are worn. Data transfer about the relative position of the robot and the object in VR from Mocap allows the operator to accurately navigate the robotic arm in the current situation, which corresponds to the real context in the room where the flight experiment is carried out.

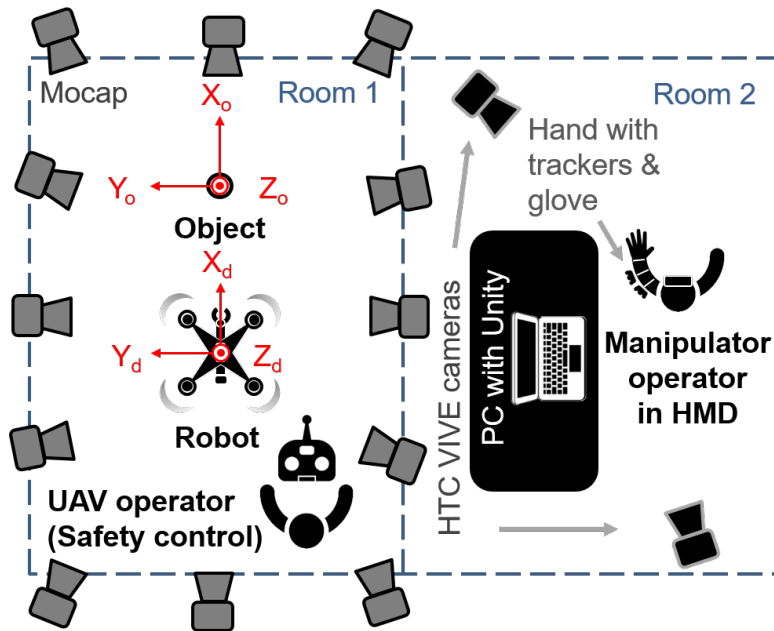


Figure 3-9: Scheme of the rooms for VR-based teleoperation experiment.

3.8.2 VR-based Teleoperation Tests

For the VR teleoperation experiment we chose a plastic cylinder weighing 105 grams as the object to be grasped. During stationary testing of the teleoperation system, we defined that the position of the trackers on the shoulder and forearm influences the possibility of trackers' circular offset on the hand, which can decrease the work area of θ and β . After that, we calibrated delays of control codes for the manipulator, glove, and Unity. Long delay or non-synchronous repetition of the movement of the operator's hand by the manipulator can cause unsuccessful aerial manipulation with the object.

Fig. 3-10 shows the change of the wrist joint position, the torques of the servomotors of the manipulator, roll, and pitch angles of the UAV in time. The recorded

time interval is shown between the moment when the robot hangs over the target position and the time when it is stabilized after releasing the object. Furthermore, the time-stamps of the key operations (contact with an object, object grasping, raising and releasing) are marked on this figure. The target trajectory was filtered and collected with a big time interval between data records; therefore it doesn't contain oscillations.

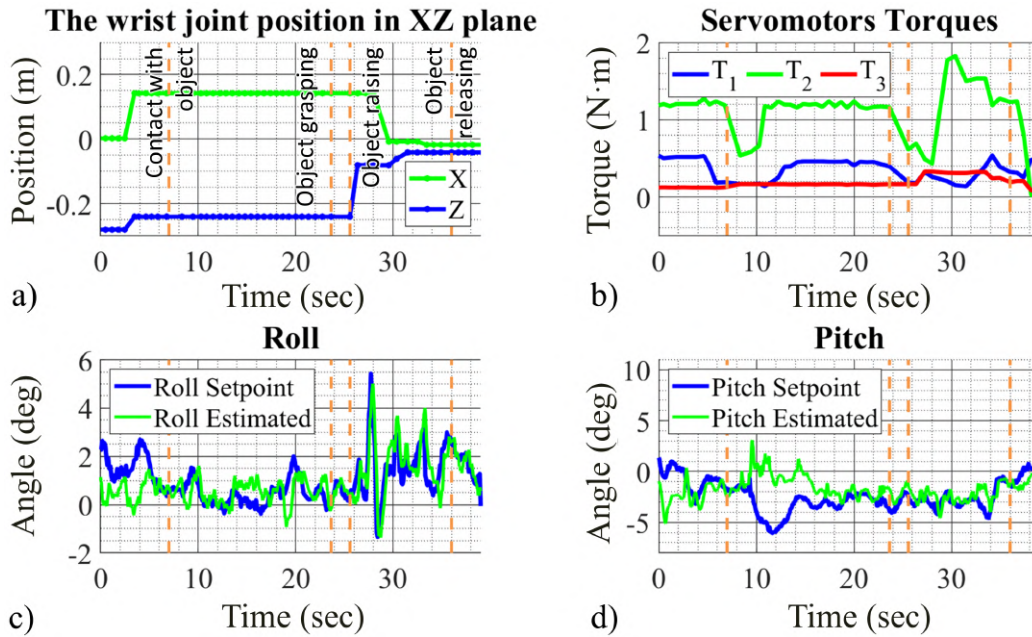


Figure 3-10: Coordinates (a) and motor torques (b) of the manipulator, roll (c) and pitch (d) angles vs. time for the flight test using teleoperation.

The largest pitch deviation is 7.15 degrees (at 11.2 sec, Fig. 3-10(d)) that corresponds to the reliable contact of the manipulator with the object. Grasping the object and picking it after 2 seconds caused a fluctuation of the UAV attitude that affected on the roll angle (maximum standard roll deviation is of 2.61 degrees). After the object grasping, the drone was confined in movement in the direction along Y-axis. That is why its roll angle during this period (8 - 20 sec) deviated from the desired value, i.e. its set-point. The movement of the object in new position also increased the torque value in the elbow joint. The object release caused a sharp decrease of the robot mass (in comparison to the robot with the object) and the robot CoM moved quickly. The drone controller handled this situation, and the robot stabilized itself after 4 seconds. During aerial manipulation, standard deviations in

pitch and roll directions were 2.03 and 0.83 degrees, respectively.

3.9 User Study

The purpose of the user studies was to evaluate the effectiveness of the developed VR-based control system. In the first experiment, we investigated the manipulation process via the VR environment towards convenience and simplicity of robot control using two proposed devices for user operation, namely the HTC VIVE controller and the wearable interface. During the second experiment, we tested the whole control system for aerial manipulation in the simulated VR scenario. Photos of operators and snapshots of the VR scenes for both User Studies are shown in the Fig. 3-11).

3.9.1 Manipulation Experiment in the Stationary Case

Description

In the framework of the experiment, the participants performed control of the aerial manipulator placed stationary at a height of one and a half meters from the floor. The main idea of the first user study is to test the process of controlling a digital twin of a real manipulator in VR environment by reading position signals from a device in the operator's hand. The manipulator was controlled directly by the movement of the operator's left hand. One meter high boxes are positioned in front of the robot at a distance of 45 cm. Fig. 3-12 shows a VR environment with a digital twin of the real setup represented the actual positions of the robot and boxes. For additional feedback, we used a video stream from a camera mounted on the manipulator grip and the information about the distance between the gripper and the objects obtained from the ultrasonic sensor. This information was displayed on the monitor in the VR scene. Besides, the VR environment contains a schematic representation of the robot and displays the angle values received from the operator's control interface. A red semi-transparent sphere appears when the participant is ready to start the experiment. The participant must touch this sphere with the virtual gripper to connect the data exchange between the operator's control device

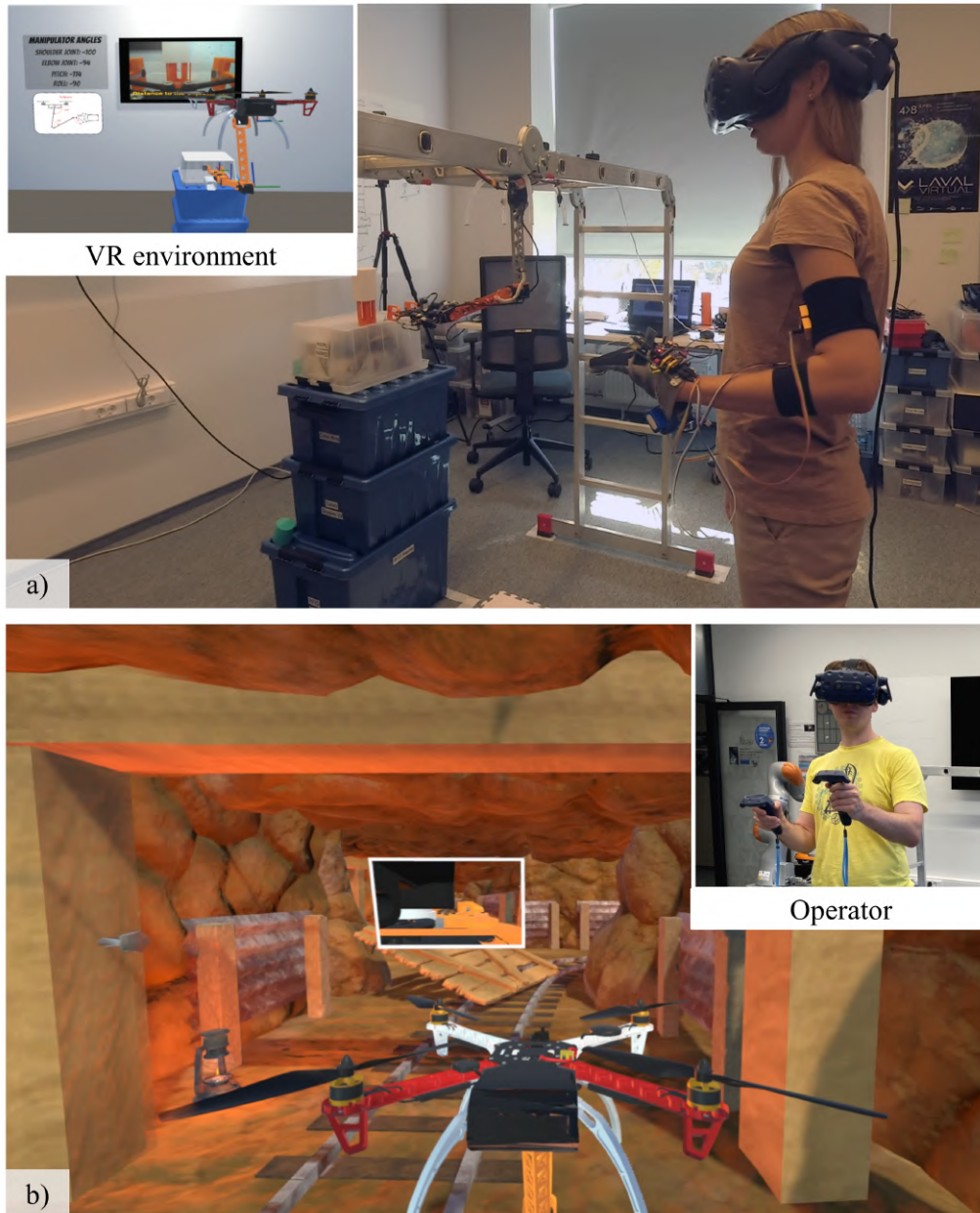


Figure 3-11: (a) The stationary test of the VR-based teleoperation using IMU-based interface. The snapshot of the VR environment is shown in the upper left corner. (b) The test of the robot control using HTC VIVE controllers in a virtual environment simulating a mine.

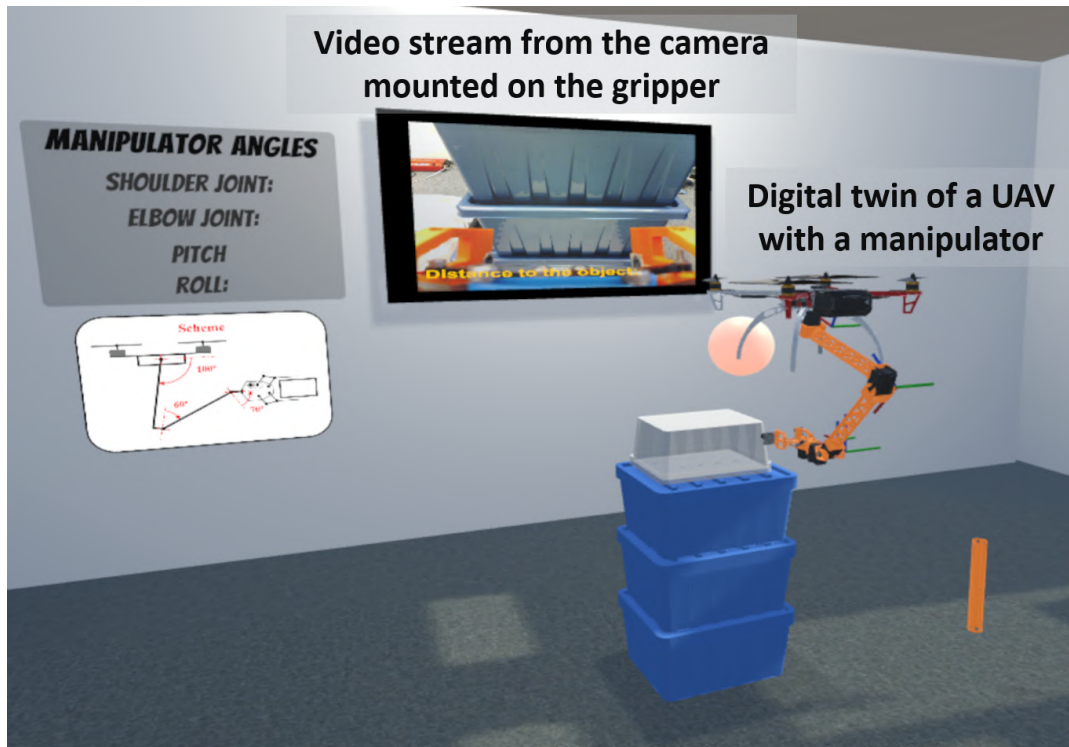


Figure 3-12: VR environment for the user study before establishing a connection with a real manipulator.

and the real robot.

For a qualitative comparison of the functioning of the developed wearable interface with the HTC VIVE controller, the user study was carried out in two stages, respectively. Each stage contained an equal number of manipulation tasks. The total number of tasks per stage was 11. Participants had to complete five types of tasks: moving an object (spray, cube, turquoise cylinder, ball, and tape) from the top box to the bottom box (up-down), moving an object (spray, cube, tape) from the bottom box to the top box (down-up), placing the ball from the top box in tape on the bottom box (ball-in-tape), taking a cube located at an angle to the robot (rotated cube), grasping the orange cylinder from the top box and placing it in the cup located horizontally on the bottom box (peg-in-hole task). Photos and characteristics of the objects are shown in Fig. 3-13.

Before the experiment, each participant was familiarized with a short instruction on how to use the teleoperation system. While operating the controller, each participant performed an initial device calibration for themselves. This procedure was not

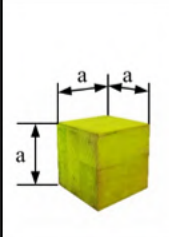
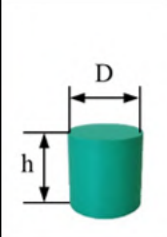
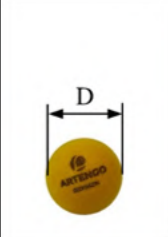
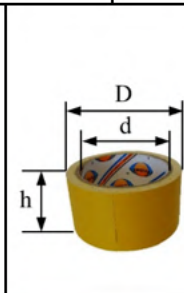
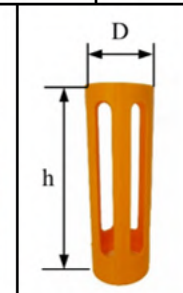
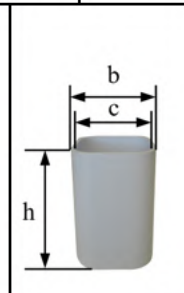
| | | | |
|---|---|--|--|
|  |  |  |  |
| Spray | Cube | Turquoise cylinder | Ball |
| 55.6 g | 120.9 g | 35.5 g | 4 g |
| h = 145 mm, D = 50 mm | a = 58 mm | h = 58 mm, D = 58 mm | D = 44 mm |
|  |  |  | |
| Tape | Orange cylinder | Cup | |
| 133.5 g | 48.4 g | 78.1 g | |
| h = 50 mm, D = 96 mm, d = 77 mm | h = 175 mm, D = 58 mm | h = 100 mm, b = 69 mm, c = 63 mm | |

Figure 3-13: Objects for manipulation used in the User Study.

required for the wearable interface, since the *IMUs* are initially located on certain places on the operator's hand. Thereafter, the participants had time to practice using each device. The main objectives of this training were to get acquainted with the principles of manipulator control, study the *VR* application, as well as check the manipulator's working area so that the participant perceived the technical capabilities of the robot. The training session for each device took from 4 to 8 minutes. The session time for all tasks took from 37 to 64 minutes per participant. After completing the tasks using both devices, we asked participants to respond to a 12-question survey using bipolar Likert-type seven-point scales. The questionnaire was drawn up based on the questions described in the article [Witmer and Singer \[1998\]](#) and in the article [Pérez et al. \[2019\]](#). The survey results are presented in Fig. 3-14.

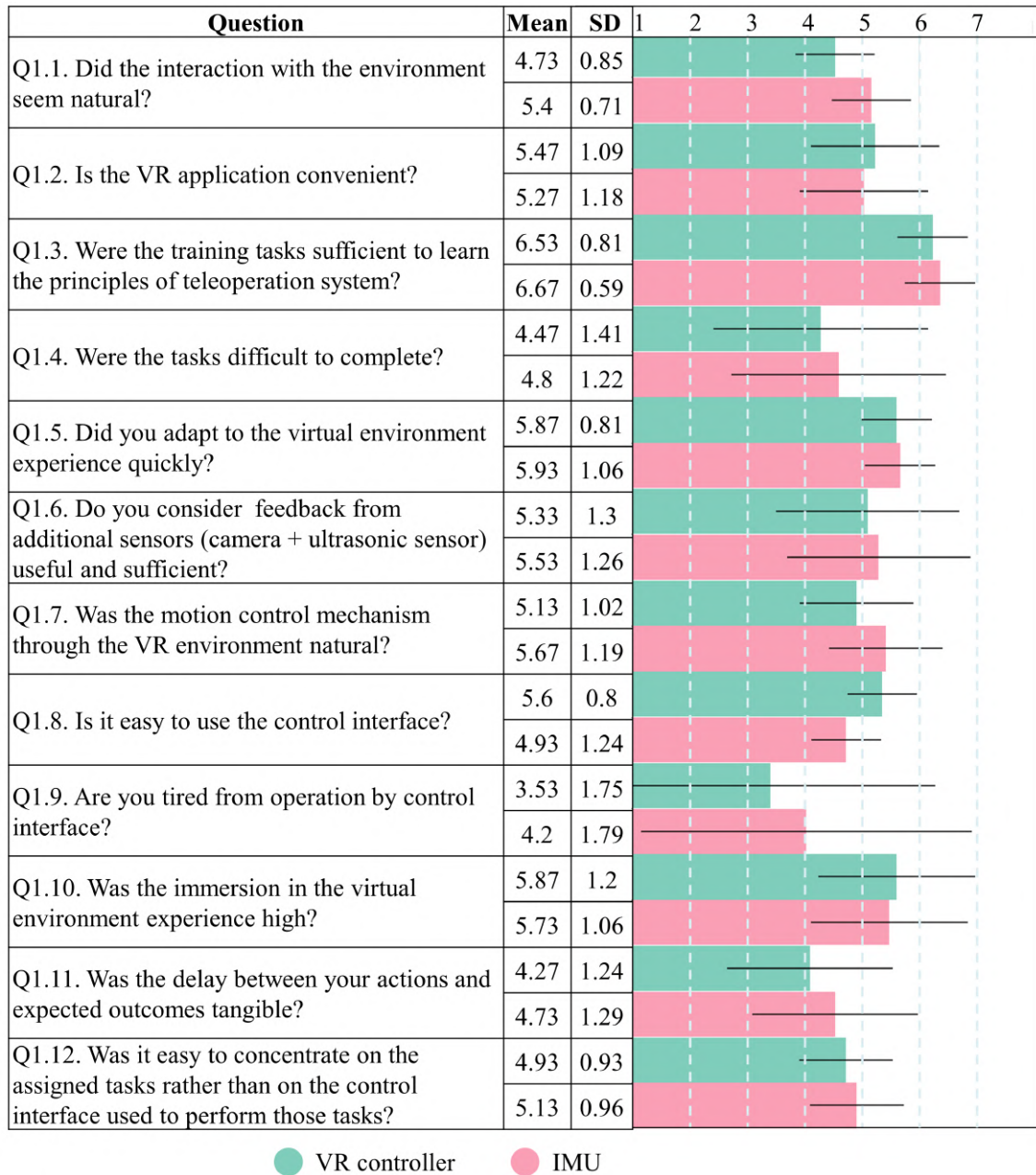


Figure 3-14: Evaluation of the participant's experience for both control methods in the form of a 7-point Likert scale (1 = completely disagree, 7 = completely agree). Means and SD are presented.

Participants

The experiment involved 17 subjects (sixteen males and one female, aged from 22 to 31 years old). Six participants used VR only a few times, three participants have never had experience using VR technologies, four people had experience with VR from time to time, and four people answered that they used VR devices regularly.

Results

The subjects assessed the quality of the VR application in terms of convenience and comfortable involvement in the robot control process (Q1.2, Q1.5, Q1.10). On the question Q1.1 the participants answered that interaction with the VR environment was quite natural when using a controller (4.73/7) and comfortable when using a wearable interface (5.4/7). According to results of *Analysis of Variance* (ANOVA) the type of control interface affects the naturalness of the interaction in the VR environment ($F(1, 28) = 5.04$, $p = 0.03 < 0.05$). Thus, by using the wearable interface, the participants used all the advantages of the developed VR application more effectively. Based on additional comments to the questionnaire, we can note a correlation with question Q1.6, as some participants noted that they paid more attention to the live video from the camera mounted on the gripper, as well as the need to install an additional camera on the UAV itself, to track the gripper position from a different view. The data from the ultrasonic sensor was used from time to time during missions, mainly to estimate the size of objects and the distance to obstacles. The usage of the ultrasonic sensor was most useful during training, where participants checked the distance between the robot and objects.

Based on the results of the survey, we can conclude that both devices had comparable characteristics for the participants. However, the developed IMU-based interface is a more convenient device, which provides a natural way to control the manipulator (Q1.7, Q1.12). This method of control allows the operator to control the manipulator as people control their hands. The robotic arm naturally repeats a human hand movements. This provides an increased focus on performing tasks without the necessity to switch attention on the control of the manipulator functionality using buttons, which is necessary at the usage of a controller. In comments to the questionnaire, five subjects noted a significant inconvenience of gripper control by the controller compared to the wearable interface.

At the same time, the participants noted that the control with the controller is easier (Q1.8), and with this type of control, they are less tired (Q1.9). The *standard deviation* (SD) in the answers to question Q1.9 is the largest in the survey, which can be explained by the experience of using virtual reality. Participants with

no experience or superficially familiar with this technology reported more fatigue than experienced users. Beginners required more effort to concentrate on using the handled controller, and some of them used video from the camera more than the VR scene, which made the task more difficult. This was reflected in the perceptible standard deviation in questions of engagement in VR (Q1.10, SDs are 1.20 and 1.06 for the controller and wearable interface, respectively) and the use of information from the camera (Q1.6, SDs are 1.30 and 1.26 for the controller and wearable interface, respectively). Also, the VR experience of the participants was reflected in the large SDs of answers to the question about the complexity of the user study tasks (Q1.4). In this case, experienced subjects noted the ease of completing the tasks, although not all of them were able to complete the Peg-in-hole task. We can note the duality of responses about the usability of devices (Q1.7 and Q1.8). This is explained by the fact that when controlling by the IMU-based interface, some of the participants intuitively better associated their hand with the manipulator, while some of the participants concentrated their attention on the position of the manipulator joint angles. In turn, the reason for this could be a more tangible delay (Q1.11) in the response of the robot to the control system when using the wearable interface, which is explained by a more reliable data transfer protocol for the factory HTC VIVE controller.

The tasks provided for the user study were fully consistent with effective teleoperation training (Q1.3) and were sufficiently difficult for the participants to cope with proposed objectives and, at the same time, be able to study the possibilities of remote teleoperation of the robot (Q1.4). From the observation of the experiment executions, it can be noted that the set of tasks selected for the user study corresponded to the successful development of VR-based teleoperation skills. Fig. 3-15 shows the average number of attempts for all tasks except peg-in-hole; the statistics of the peg-in-hole task execution is shown in Fig. 3-16. Fig. 3-15 shows that the average number of attempts for all tasks does not exceed two. There is also a tendency for the first tasks (up-down) to take on average more attempts, while the subsequent tasks (down-up, ball-in-tape, and rotated cube) mostly took one try. The ball and tape were the most difficult objects to manipulate. Based on the ex-

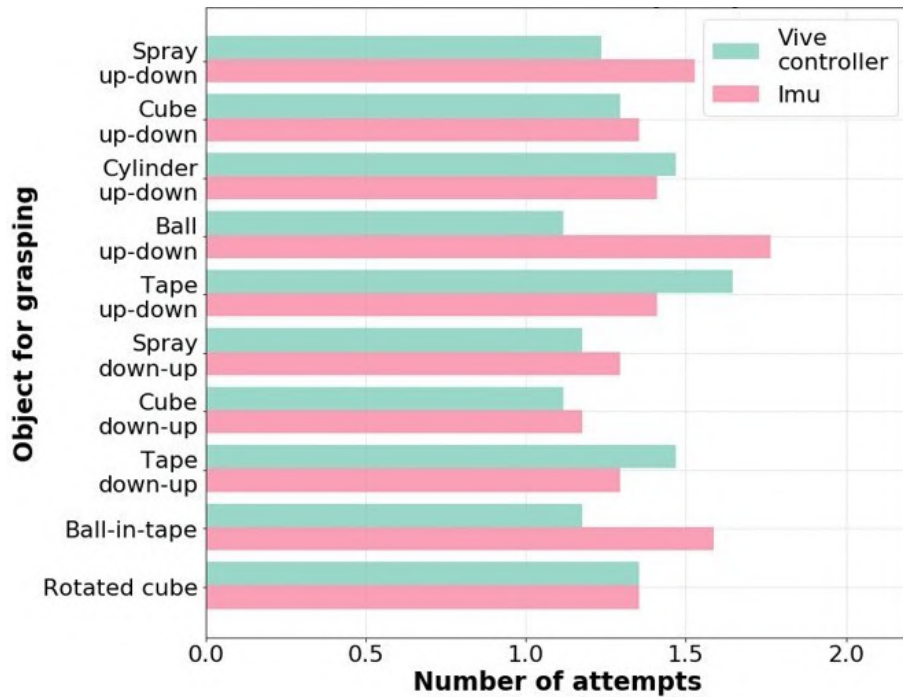


Figure 3-15: The statistics of the mean number of attempts of the task execution.

The statistics of the Peg-in-Hole task execution

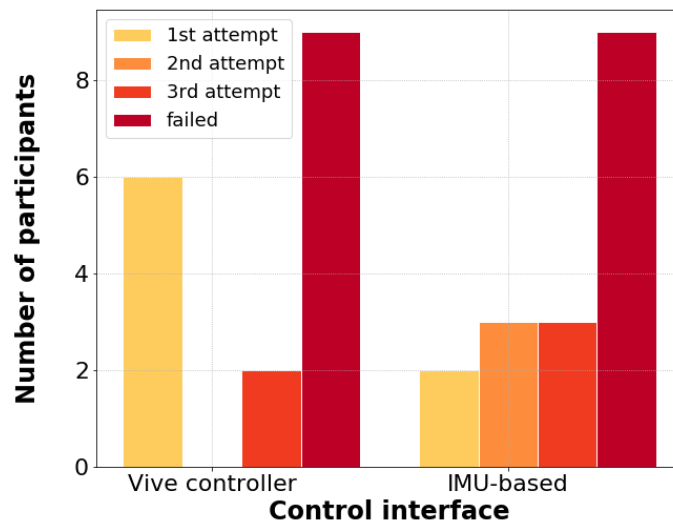


Figure 3-16: The results of the Peg-in-Hall task execution. The first three columns represent the number of participants who completed the task on the first, second, and third attempts, respectively. The fourth bar indicates the number of participants failed the task.

perimental results, performing tasks with tape caused difficulties when the operator used the HTC VIVE controller and interacting with the ball was more difficult at teleoperation using a wearable interface. To explain the causes of the difficulties

with the manipulation of these objects, it is necessary to refer to the questionnaire results. The tape has the most complex shape compared to other objects, which affects the necessity for a more thoughtful performing of the manipulation in the plane. Accordingly, the participants required the use of all DoF of the gripper, but this function is performed less conveniently when using the controller (Q1.1), as noted earlier. Implementation of the tasks with ball required more accurate positioning, which was slightly more difficult to achieve at the presence of more tangible delay (Q1.11) when using the wearable interface.

Before executing the peg-in-hole task, the participants had already formed a notion of the usage of several different approaches to manipulating objects, and the subjects could individually choose a method for successfully completing the final task. For this goal, it was necessary to place the orange cylinder in a horizontal cup. The cup was not fixed on the bottom box, which made the assembly more complicated, as the assembled structure could tip over if the manipulator operator would not be careful. At the same time, the participants could move the assembled structure to the top box or take additional actions with the objects using the manipulator so that the objects were in a more convenient position for assembly. In Fig. 3-17 we showed the initial position of the orange cylinder and cup, the final position of the objects how it was suggested to assembly, and three another type of assembly of the objects. Among the participants, four people were able to complete the peg-in-hole task using both devices, four people completed the task using the

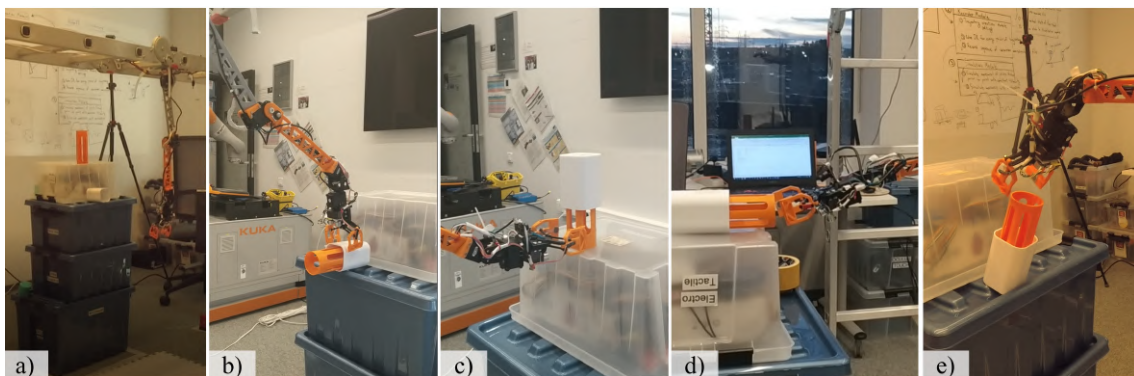
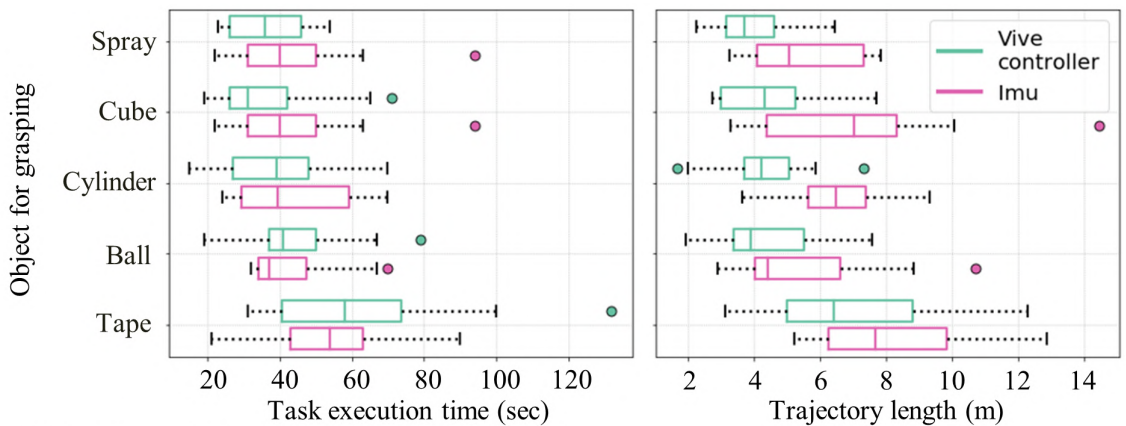


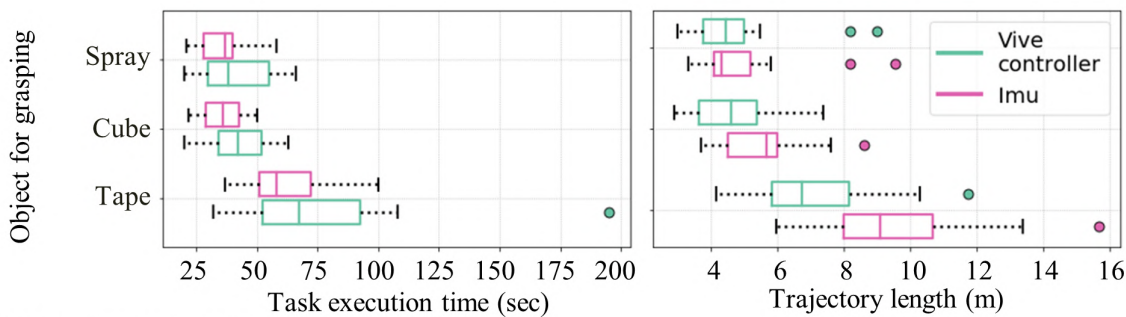
Figure 3-17: The peg-in-hole task. The initial setup for the task (a), assemblies of the objects in the proposed format (b), with the transfer of both objects to the top box (c, d), after lifting the cup and placing the orange cylinder in it (e).

HTC VIVE controller, and the same number of people completed the task using the wearable interface. Five subjects failed to perform the task in three attempts.

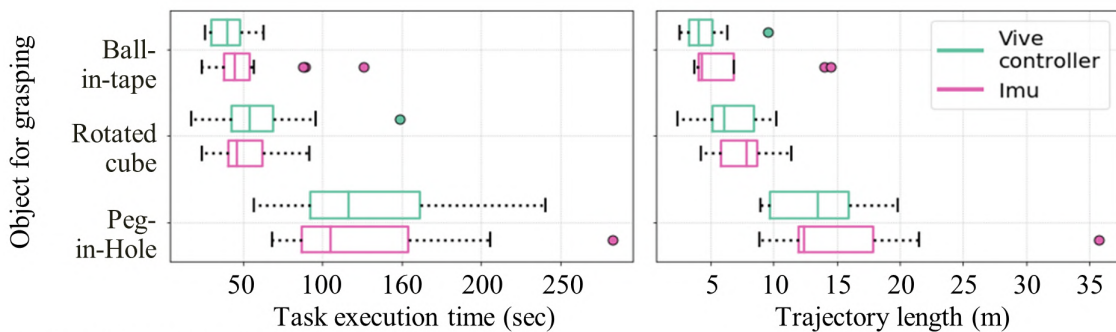
In Fig. 3-18 we showed the average values of the execution time and trajectory length of the manipulator gripper for each teleoperation task. These graphs clearly show that the execution of tasks using both devices was carried out at similar time intervals. Also, the average time to complete tasks is similar. It can be noted that tasks such as lifting an object from bottom to top using the IMU-based interface



a) The up-down manipulation tasks



b) The down-up manipulation tasks



c) The advanced manipulation tasks

Figure 3-18: The average task execution time and length of the trajectory for the manipulation tasks.

were performed faster (the average task execution time for down-up tasks are 43.08 and 53.19 for IMU-based interface and VR controller, respectively). More complex tasks (tape manipulation, rotated cube) were performed a little slower by both devices in regard to simple pick-and-place tasks. Our assumption about the reason for this statistic is that the boundary positions of the working area of the manipulator are slightly more difficult to reach using a wearable interface due to the individual characteristics of the body structure of each operator. Participants tried to stretch their hand in front of them in different ways (very often with the elbow to the side, rather than straight ahead). At the same time, from observing the progress of the User Study, we noticed that using the HTC VIVE controller, the subjects leaned forward if they could not reach the object, which caused discomfort when controlling. The reason for the forward tilt is an inaccurate calibration of the controller before starting the tasks. In turn, this error occurred again due to the individual characteristics of the body.

The trajectory length of the gripper position is shorter in case of using the HTC VIVE controller. With this type of control, the participants tried to immediately move to a desired position, sometimes forgetting about the restrictions associated with the robot's environment. Using the wearable interface, the subjects moved their hand more smoothly, and, when they were near the target, more frequent fluctuations in the trajectory were observed, which may be due to the motivation for more accurate positioning of the gripper near the object before taking or lowering it to the target position. The trajectories of the operator wrist position (target trajectory) and the gripper position for each task are shown in Fig. 3-19 - 3-21. The gripper trajectories are better following to the target trajectories in case of the control via wearable interface that is clearly seen in Fig. 3-19 (b-d), Fig. 3-20 (d, e), and Fig. 3-21. This is well consistent with the faster manipulation speed for this control device. Controller trajectories also have a characteristic margin of the distance between picking up an object and lowering the object to a new position. This is due to the fact that the subjects moved the manipulator back so as not to hit him to the boxes, whereas using the wearable interface, the participants felt the real position of the robot better and calmly move the manipulator around the obstacles.

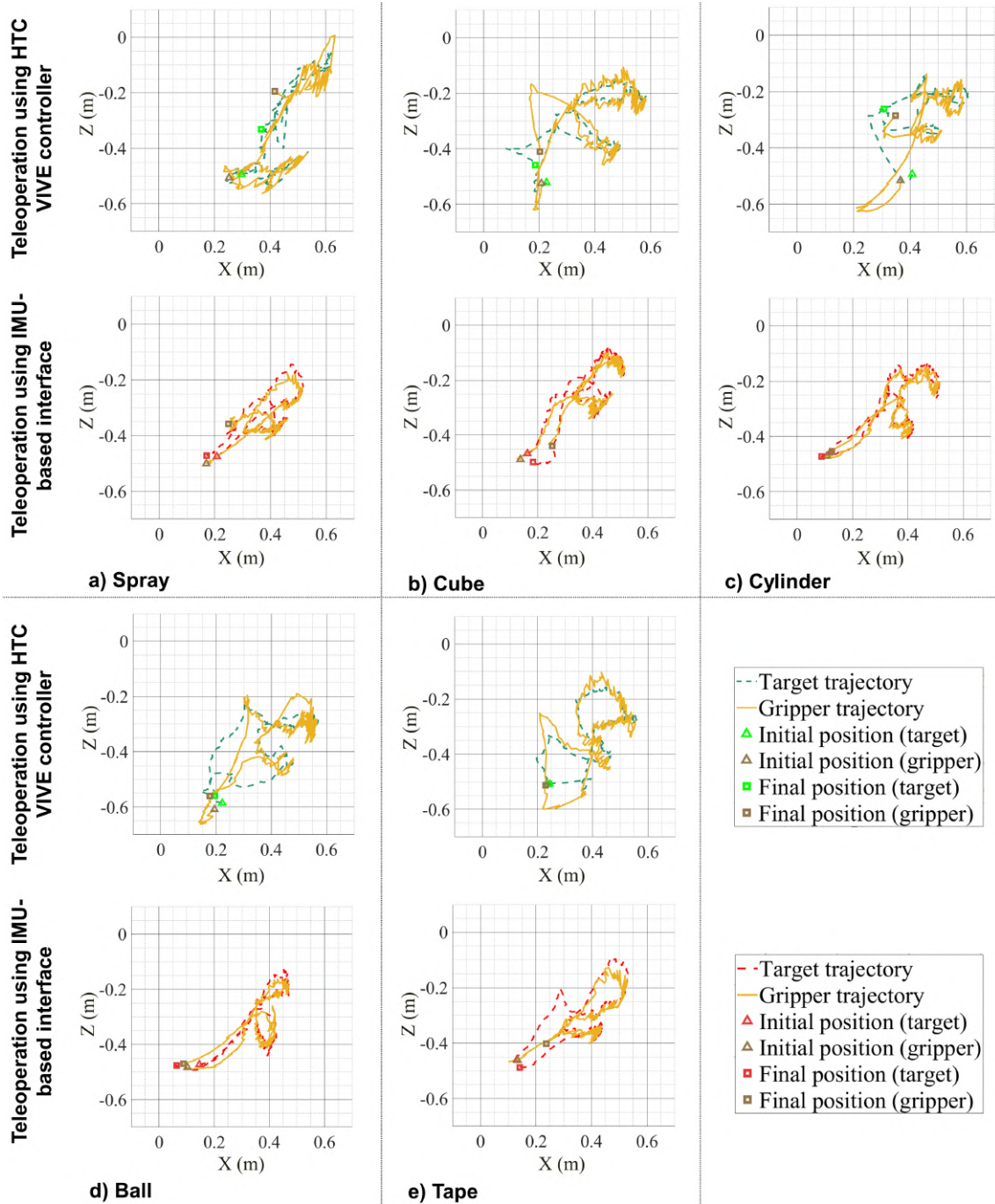


Figure 3-19: The trajectories of the operator wrist position (target trajectory) and the gripper position for the up-down tasks.

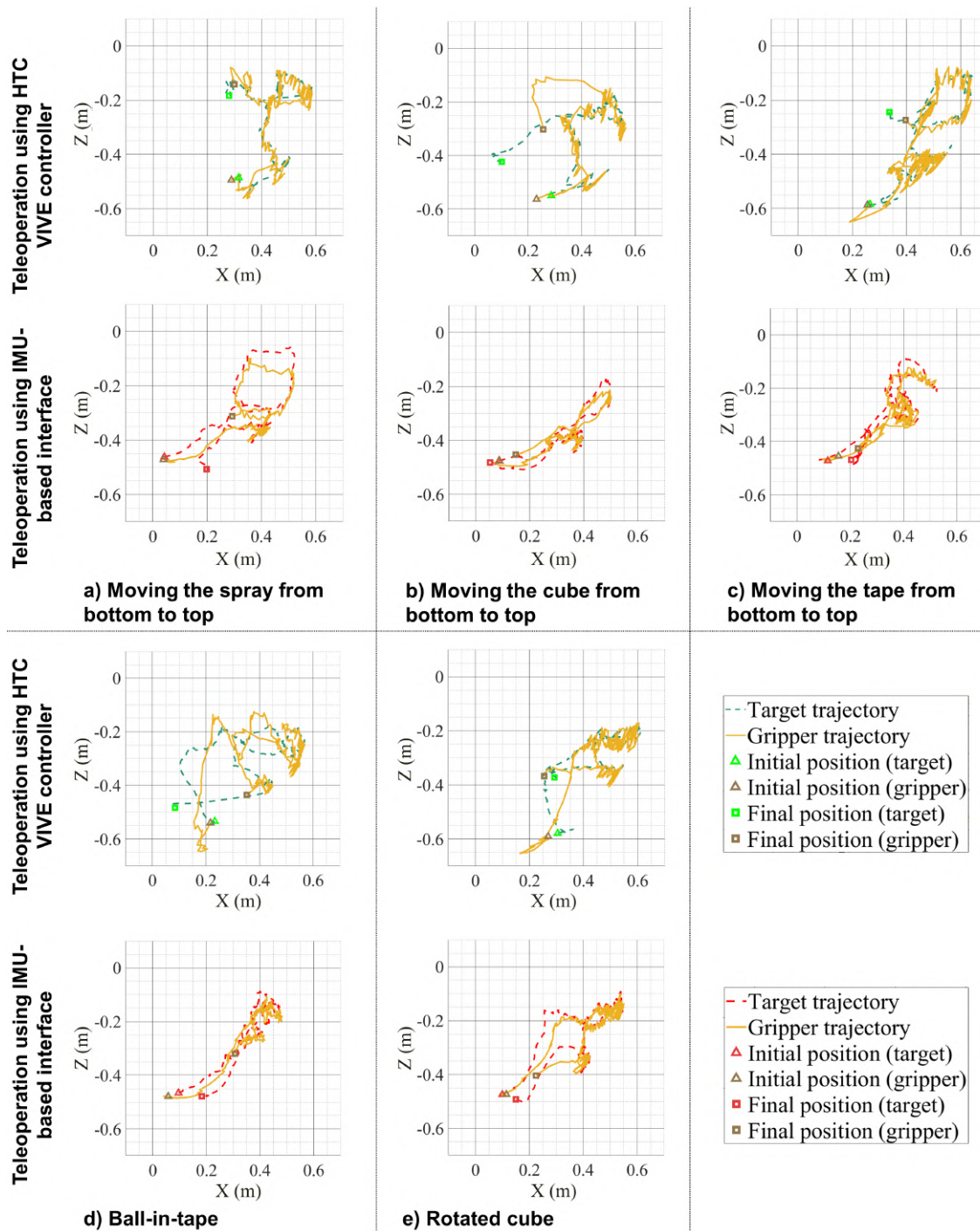


Figure 3-20: The trajectories of the operator wrist position (target trajectory) and the gripper position for the down-up, ball-in-tape, and rotated cube tasks.

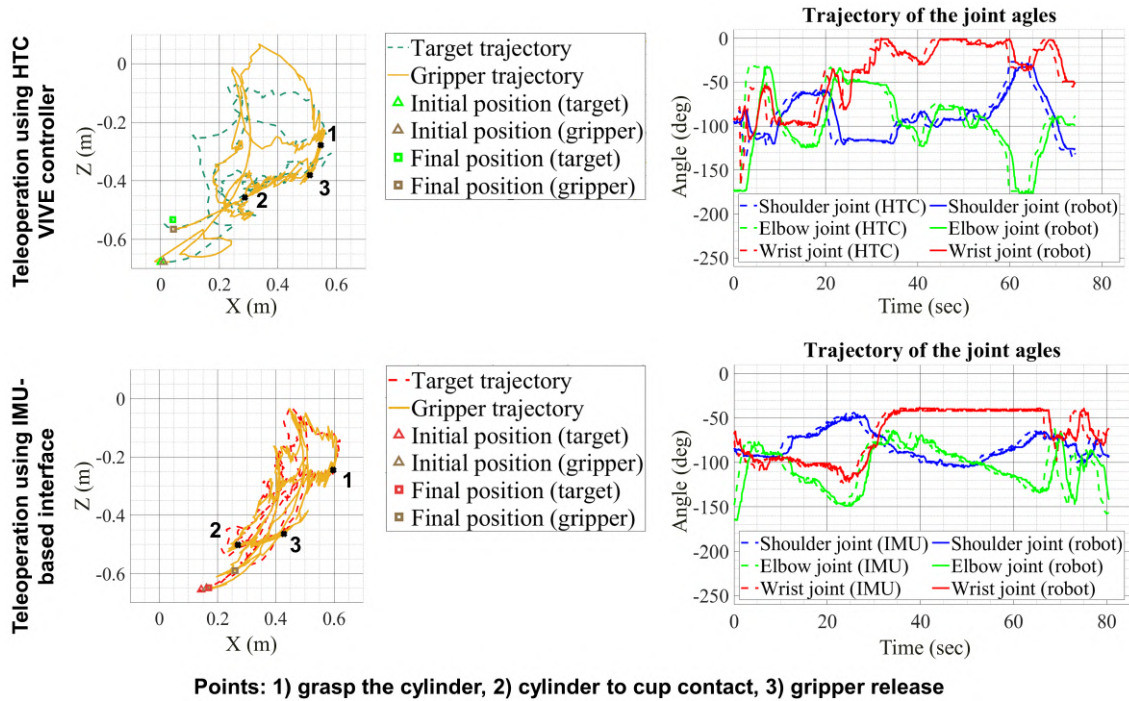


Figure 3-21: The trajectories of the operator wrist position (target trajectory) and the gripper position for the peg-in-hole tasks.

To better evaluate the performance of both devices we calculated the average manipulation speed during the execution of all tasks by each participant. The box-plots for the average speed are shown in Fig. 3-22. ANOVA results showed significant difference between the manipulation velocities ($F = 6.8, p = 0.016 < 0.05$). It means that the operators can control the manipulator faster by 0.034 m/s (by 27%) using the IMU-based interface.

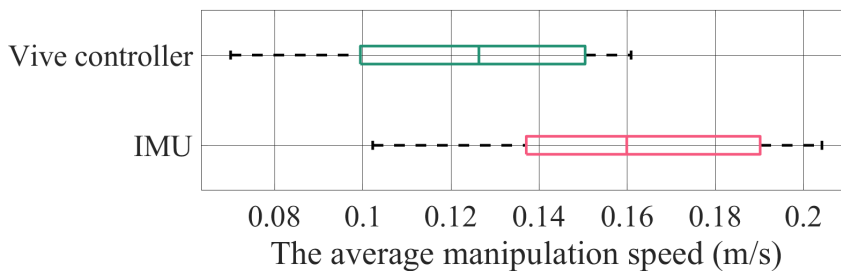


Figure 3-22: The average manipulation speed.

3.9.2 Experiment of Aerial Manipulation in Virtual Mine

Description

As was mentioned in Section 1.2, one of the main potential fields of application for robots equipped with manipulator are search and rescue operations on the reserves, underground tunnels, mines, in areas after natural disasters. Thus, one of the potential scenarios for remote operating could be the robot usage in the underground environment (e.g., mine), where there was a partial collapse of the rocks. The robot explores the tunnel and searches the places where the collapse occurred. Toxic gases (e.g., methane) can accumulate at these areas. During the operation of coal collapse detection (in this case, methane appears most frequently), the robot should deliver and put a gas detector in the center of the gas source. We chose this scenario for the second user study to test the robot's flight control together with manipulation. For this purpose, we used a ready-made model of a virtual mine⁵, some parts of which have been modified in accordance with the conceived scenario. We simulated the collapse of rocks in some areas of the tunnel and added visually noticeable sources of gas (Fig. 3-23(b)). In order to ensure the similarity of control of the real manipulator, we also added window with a view from the camera located on the gripper (Fig. 3-23(a)).

The participants of the experiment had to control the flight of the robot using the HTC VIVE controller and simultaneously to control the manipulator using both methods, as in Subsection 3.9.1. The flight control device was in the right hand, the manipulator control device in the left. As described in Section 3.5, we used the position of the VR controller to control the speed of the robot movement along the three axes X , Y , Z . Trackpad was used to control the drone rotation around the yaw axis. The trigger was used to move the robot to the mode of holding the position, that make possible comfortable control of the manipulator without thinking about controlling the flight during this operation. At the beginning of the experiment, the robot is located in a tunnel near a box with three gas detectors located in different positions (Fig. 3-23(a)). There was a large cave behind the robot in which the

⁵Purple Crystal Mine Asset, available: <https://assetstore.unity.com/packages/3d/characters/purple-crystal-mine-113576>

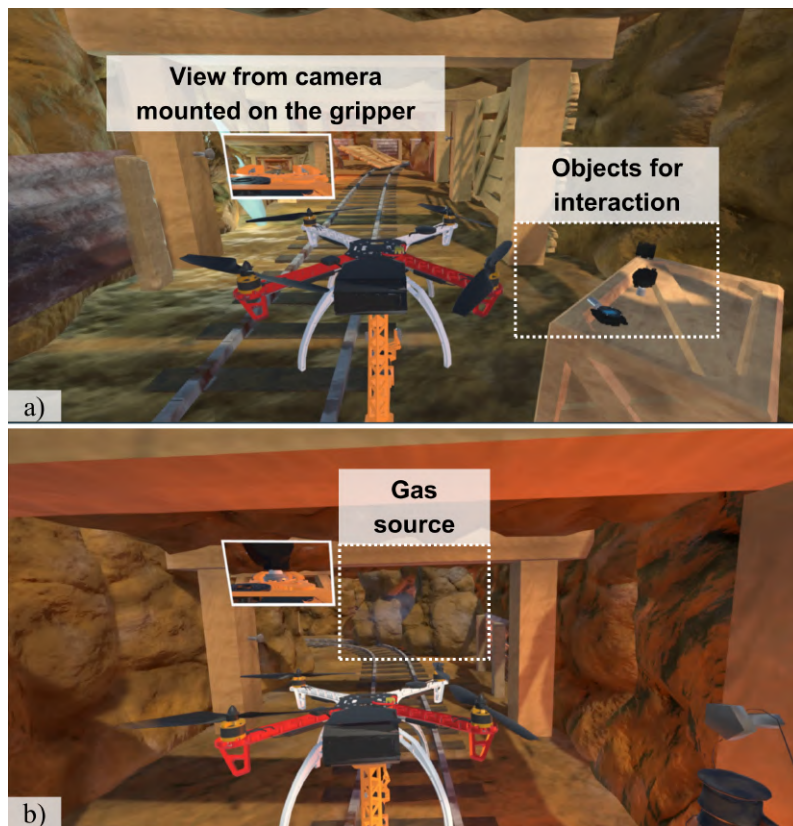


Figure 3-23: The initial position of the robot in virtual mine (a) and the screenshot of the robot near the gas source (b).

subjects tested the control of the robot. According to the experiment scenario, each participant must take a gas detector and fly through the mine tunnel in order to detect the gas sources. Upon found the source, the subject had to place the detector at the epicenter of the gas. Then, the subject returned to the starting position to repeat the procedure. We located 2 gas sources in the mine. While using the first manipulation interface, the subject had to fly through the entire shaft in order to check for the presence of all gas sources. While completing the task using the second control method, the participants already knew the route and the number of sources. Thus, for the purity of the experiment, half of the subjects first tested the wearable interface, and the rest of the participants started from using the HTC VIVE controller. The objects of the environment (walls, ceiling, stones, etc.) contained the primitive colliders (for simulation of physical collisions) to increase attention and accuracy of the participants during the task. When the aerial manipulator collided with objects of the environment (e.g., walls, stones), the robot was returned to the

initial position, and the mission was restarted. The session time took from 10 to 25 minutes per participant (the average time was 15 minutes). After completing the tasks using both devices, we asked participants to respond to a 6-question survey using bipolar Likert-type seven-point scales (Fig. 3-24).

| Questions | Mean | SD |
|--|------|------|
| Q2.1. Is the position of the third-person view for the drone control convenient? | 5.9 | 1.08 |
| Q2.2. Is it difficult to position the robot to interact with the object? | 4.27 | 1.36 |
| | 4 | 1.28 |
| Q2.3. Is it easy to use the whole control system? | 5.54 | 0.89 |
| | 5.91 | 0.99 |
| Q2.4. Were you stressed while completing the task? | 4.09 | 1.88 |
| | 3.72 | 1.66 |
| Q2.5. Did you feel some physical discomfort? | 4.46 | 1.67 |
| Q2.6. Are you tired from operation by control interface? | 3.55 | 1.43 |
| | 3.36 | 1.61 |
| <p>● General question ● VIVE controller ● IMU-based</p> | | |

Figure 3-24: Evaluation of the participant's experience for both control methods in the form of a 7-point Likert scale (1 = completely disagree, 7 = completely agree). Means and SD are presented.

Participants

In total, 12 subjects volunteered in the experiment, ten males and two females, aged from 22 to 43 years old. Two participants had VR experience for the first time, three participants use VR devices regularly, and other people answered that they experienced VR several times. Four subjects did not take part in the first user study.

Results

The goal of the second user study was to evaluate the proposed flight control method and test the whole VR control system for aerial manipulation. Fig. 3-25 shows user evaluation of both control methods based on the answers of the questionnaire in the form of box-plots. The participants noted the convenience of the robot flight control. The advantage of use a VR controller operation is that even an unprepared person is able to cope with UAV control (after training for several minutes), compared to standard radio equipment for UAV control. The proposed method uses intuitive control only with the movement of one hand, whereas for radio equipment it is necessary to use both hands. The only function that took some time to master was controlling the yaw direction of the drone using the touchpad. However, by the second trial, participants were already coping with drone rotation well. While navigating the robot in the mine, 4 out of 12 participants crashed the robot into objects of the environment, two for each type of manipulation.

The grasping of the virtual object caused difficulty for some subjects (Q2.2) that contributed to increased stress during the task (Q2.4, SD is 1.88 and 1.66 for

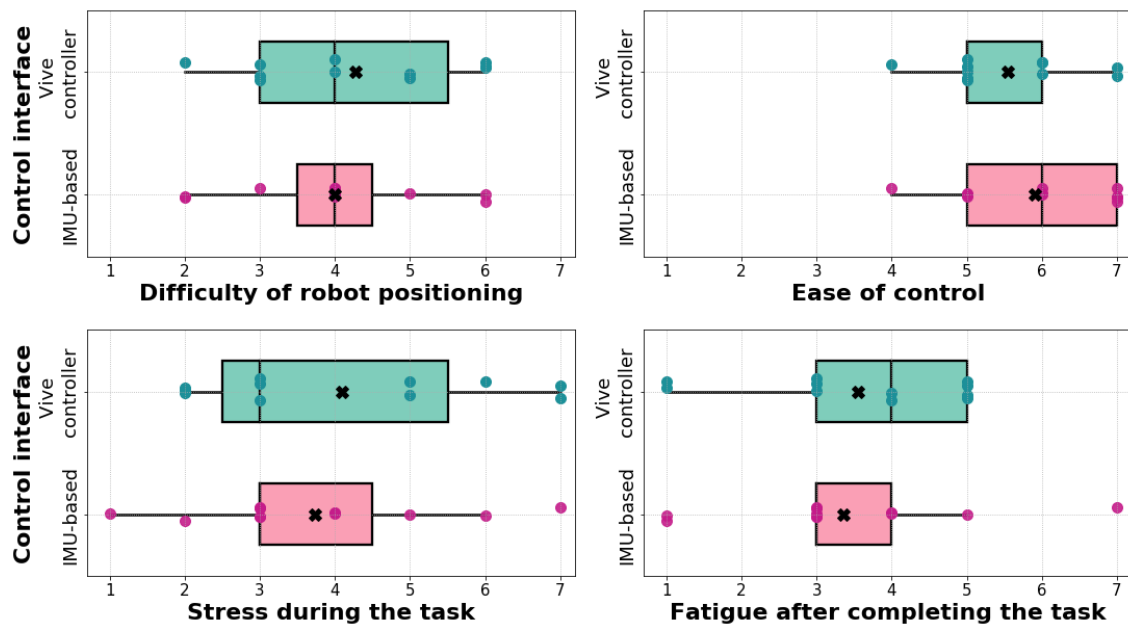


Figure 3-25: User evaluation of both control methods. Average values are marked with crosses. Scatter points represent answer of individual participants.

VR controller and wearable interface, respectively). However, the cause of stress is largely due to the appearance of perceptible physical discomfort from the usage of virtual reality (Q2.5), which was noted among participants, mainly those who had not used VR before. The reasons for the discomfort could be the following factors: not proper initial setting the helmet for a clear image, as well as subject mind confusion caused by the feel of drone movement while, in reality, the operator is stationary. Nevertheless, it was observed that physical discomfort decreased over time as the operator became accustomed to the VR environment. Grasping the object caused certain difficulties for the subjects because, for the precise positioning of the aerial manipulator, it was necessary to rely simultaneously on the additional view from the camera mounted on the gripper that required more concentration. In this regard, the time of the object manipulation was 44.20% of the time to complete the entire task (mean value).

At the same time the subjects noted the convenience of the third-person view during the robot control (Q2.1). While leaving in the comments the wish to move the view from the grasping camera to a more comfortable position (sometimes it interfered with the view of the scene). Despite the discomfort of active movement in the virtual environment and the difficulties of implementing precise interaction of virtual objects in Unity (object grasping), the user study participants highly rated the simplicity of the robot control using developed VR-based teleoperation system (Q2.3), besides SD has the smallest value for question Q2.3.

Fig. 3-26 shows the distribution of task execution time and flight speed of the robot. The task execution time was taken for the activities of grasping of the gas detector, moving to the first gas source, and then placing the sensor at the epicenter of the source. This procedure took less time using the HTC VIVE controller to control the manipulator, also the spread of time values is less. The average flight speed of a virtual drone is practically the same for both modes of manipulator control. Since the participants started the user study by alternating the first device, we can note that the rate of the second trial execution increased by 21.21% for those who started from the VR controller, by 14.53% who used initially the wearable interface. Thus, the speed of the task execution increased for the second trial in

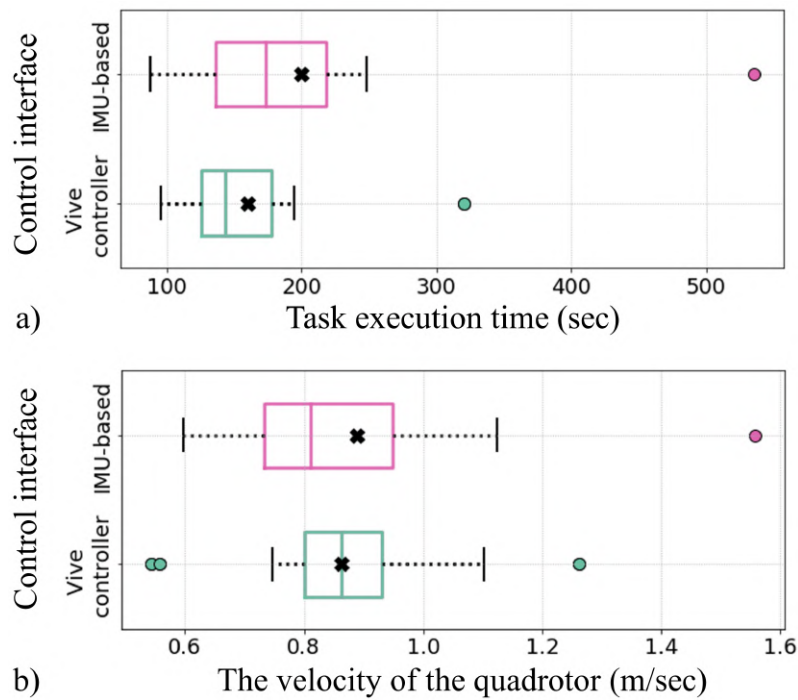


Figure 3-26: Experimental results averaged across all participants. a) Task execution time; b) The drone velocity during the task. Average values are marked with crosses.

any case regardless of which control interface was used by the participant at the beginning.

Trajectories of the aerial manipulator in virtual mine for two subjects are shown in Fig. 3-27. The first participant started tasks completing using the VR controller, the second participant initially used a wearable interface. For these tests, it can be noted that the participants guided the robot along almost identical trajectories, keeping the robot in the center of the tunnel to avoid collision with objects in the environment. The lengths of the trajectories of the first test completion, taking into account the flight in the test room, were 426 and 428 meters for the first and second participants, respectively. For the second trial, the lengths of the trajectories were 215 and 211 meters, respectively. The trajectory of the second trial does not include the flight in the training room and the flight behind the second source of gas, since the participants already knew the location of the gas sources.

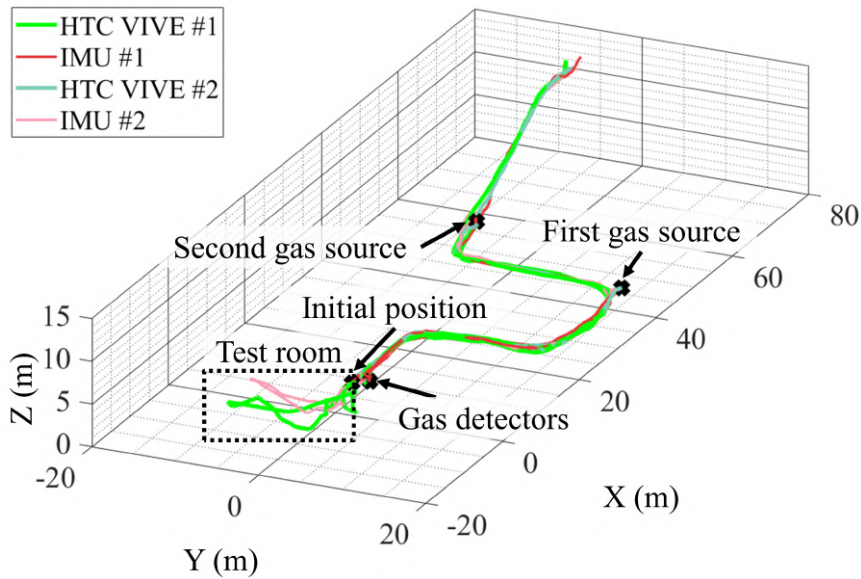


Figure 3-27: The trajectory of the aerial manipulator in virtual mine for the second User Study. The green and red curves represent the trajectories of the first participant, while the pink and turquoise curves represent the trajectories of the other one.

3.10 Concluding Remarks

We proposed a novel VR-based teleoperation algorithm to control flying robots designed for aerial manipulation. For this goal, we developed a wearable interface to read the position of the operator's hand and the position of the bent fingers. Also, a special VR application was designed for comfortable control of the robot. The developed human-robot interaction strategy allows the operator to intuitively control a flying robot and process of aerial manipulation in a virtual environment supplemented by a real-time video stream from the robot. Tactile feedback from vibration motors of the glove effectively complements the visual information of the virtual environment, being a tangible confirmation of contact with the object. The main difficulties of the teleoperation were related to the data transfer from Unity to the manipulator controller. There were the cases when it manifested itself in delays in the execution of real movements of the manipulator.

To compare convenience and technical characteristics of the developed control interface and VR controller we performed the user study of the control of the aerial manipulator placed stationary. In the second user study, the participants tested the

control of the robot flight via HTC VIVE controller in a VR environment representing the mine where the collapse occurred. A total was conducted 29 User Studies in which 21 people took part with knowledge in different areas of robotics.

The participants noted the convenience of controlling the manipulator using the VR application together with the video stream from the camera mounted on the manipulator gripper. The user study results were analyzed using statistical distribution represented by box-plot and ANOVA results. We can summarize that the IMU-based wearable interface has comparable characteristics with HTC VIVE controller and can be a simple alternative for it. One of the major VR controller disadvantage relative to the IMU-based interface is the necessity of an external tracking system limiting its operation space. Thus, the wearable controller could be used from anywhere as it relies only on its own onboard sensors. Moreover, IMU-based interface is a more natural control device and allows the operator to perform remote manipulation faster by 27% with better matching of the manipulator position to the target set-point, that was confirmed by ANOVA results of the first user study. Also, the participants appreciated the convenience of the robot's flight control and the scenario of the second user study noting its relevance for solving real challenges in the area of search and rescue.

In the first user study we noticed that participants leaned forward if they could not reach the object. This intuitive operator action can be prevented by enhancing the haptic feedback functionality of the wearable device. For this, it is possible to add a pattern for the vibration motors of the glove, which will correspond to the presence of the control device in the maximum permissible position. That is, using tactile feedback, we can mark the boundaries of the manipulation workspace, as suggested in the article [Coelho et al., 2020].

In the second user study, participants mentioned physical discomfort during robot flight in VR environment. The cause of VR sickness lies in the individual sensitivity of people to virtual movements when the person himself is in a stationary position. Watanabe and Takahashi [2020] studied the influence of this phenomenon and proposed a solution to reduce the impact of this effect. They developed a head-synced controller which synchronize the drone orientation with respect to the head's

orientation. This technology can be applied to our teleoperation system to reduce the physical discomfort of the operator.

Based on the experimental results, we chose the IMU-based interface as a more effective device for manipulator control. This interface does not need additional base stations, as was necessary when using a combination of smart glove and HTC VIVE trackers. Also, the IMU-based interface provides a reliable and more accurate reading of orientation data of the operator's hand compared to an interface based on the usage of bending sensors. In accordance with the metric discussed in the Section 3.1 IMU-based interface satisfies the factors of productivity and efficiency due to high manipulation speed and short training time. The method of the VR-based teleoperation allows performing unforeseen operations, and using the VR application with live video from the robot camera allows the operator to get information about the current robot state. The last functions satisfy the factor coactivity.

In the future, we plan to test the developed VR-based teleoperation system using only wearable interfaces. For example, it is possible to make a glove equipped with IMU sensor, the orientation angles of which will be used to control the velocities of the UAV, as we performed for the VR controller. A similar approach was used in [Buczyłowski et al., 2020]. Also, it is possible to combine IMU-based interface and a tactile glove to create a single sleeve with built-in sensors for comfortable control of the manipulator. In framework of AeroVR project we used Bluetooth wireless connection, that is acceptable in laboratory conditions. To reach the maximum efficiency of wireless data exchange between all devices in outdoor conditions, it is necessary to conduct studies using different communication methods and special protocols (for example Time Domain Passivity Approach [Coelho et al., 2019]).

Chapter 4

Analysis of Locomotion Algorithm for Landing Gear

4.1 State of the Art

To implement a ground emergency operation in unstructured terrain conditions, a flying robot should perform a safe landing. Conventional aerial vehicles without a landing platform are not able to land on uneven surfaces. Since 2012, the scientific community began the development of the adaptive landing gears for small unmanned aerial vehicles (aircraft, helicopters, and multi-rotors). A number of early articles were devoted to the design and calculation of a chassis designed like a bird legs [Nagendran et al., 2012, Xie et al., 2013]. In 2013, the helicopter landing gear [Manivannan et al., 2013] was demonstrated for landing on uneven surfaces in order to prevent from helicopter rollover, as happened during the crash of a Boeing Vertol CH-46 Sea Knight helicopter¹. Currently, several UAVs are equipped with a special landing platform, for instance, this is a passive landing gear using coupled mechanical design [Baker et al., 2013], a robotic legged landing gear developed in Georgia Institute of Technology with funding from DARPA [2015], and the landing platform with four legs designed to reduce the load during the landing [Stolz et al., 2018]. The first one can land only vertically, though it has some limitations in its

¹Wikipedia Contributors, “Boeing Vertol CH-46 Sea Knight.” Available: https://en.wikipedia.org/wiki/Boeing_Vertol_CH-46_Sea_Knight#Notable_accidents_and_incidents (Retrieved June 14, 2020)

operation. The second one has a landing gear that is equipped with force sensors in robotic leg feet used to sense ground contact and the CoM location. Third landing gear uses force controlled algorithm. This chassis has an innovative actuation, composed of a parallel arrangement of motor and brake, which relieves the motor from large impact loads during hard landings. Besides the legs are equipped by a spring-damper system acting in series to the actuation.

In addition to the landing on uneven surfaces, the ground motion of the flying robot might be necessary to accomplish an additional task (Section 1.1). Nowadays, several successful legged robots for terrestrial movement on the irregular surfaces have been developed, e.g. quadrupedal robots BigDog [Raibert et al., 2008], ANYmal [Hutter et al., 2017], Cheetah [Bledt et al., 2018] and ATHLETE all-terrain vehicle that is designed for Mars exploration [Wilcox et al., 2007]. Most of these robots are bulky and complex multifunctional machines equipped with multi-DoF legs. Compared to these robots it is worth noting two simpler robots: hexapod of Czech Technical University [Čížek et al., 2018] and ALPHRED made at the University of California [Hooks and Hong, 2018]. These robots have legs with 3-DoF, which provide increased stability when walking on 6 legs [Čížek et al., 2018] or additional functionality for performing manipulations with objects [Hooks and Hong, 2018]. Such light robots can be integrated with small UAV.

Among the robots that combine both considered abilities motion in the air and on the ground, can be noted: HyTAQ [Kalantari and Spenko, 2013], HERALD [Latscha et al., 2014], robot HexaWalker² and project Hexapod-Quadcopter Robot [Pitonyak and Sahin, 2017] (Fig. 4-1). HyTAQ is a micro UAV equipped with a rolling cage, which allows carrying out terrestrial locomotion. HERALD is a combination of two snake robots with a quadrotor using a magnetic docking system. HexaWalker is a robot assembled from hexacopter and hexapod without additional sensors. The last of the above mentioned hybrid robots is the prototype of a robot with frame rays, which can be transformed into legs; however, this robot does not have an adaptive landing algorithm.

²HexaWalker. MadLab Industries. 2015, available: <http://madlabindustries.com/hexawalker> (Retrieved April 30, 2020)

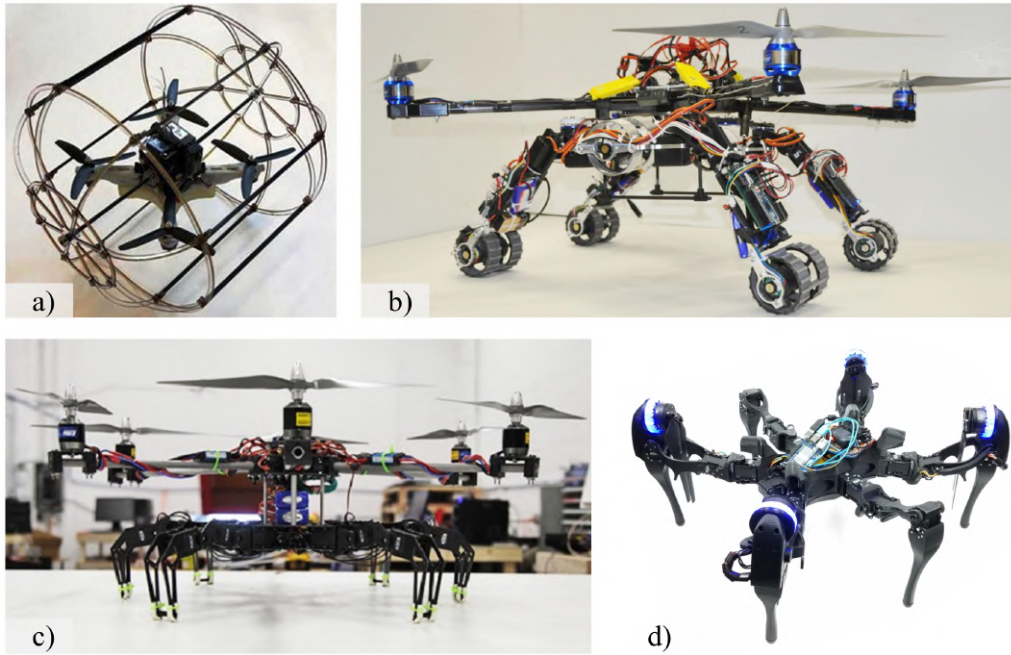


Figure 4-1: The robots capable to fly and move on the ground: (a) HyTAQ [Kalan-tari and Spenko, 2013], (b) HERALD [Latscha et al., 2014], (c) HexaWalker, and (d) Hexapod-Quadcopter Robot [Pitonyak and Sahin, 2017].

In 2017-2018 the DroneGear adaptive landing platform [Sarkisov et al., 2018] was developed in our laboratory for adaptive landing. This robot is equipped with four 2-DoF robotic limbs and has a control system, which can adapt to the uneven surface using data from the embedded torque sensors in the knee joints and IMU sensors in the footpads. The structure of its legs ensures a reliable landing of the UAV. As it was shown, a typical construction of the legged robots contains an extra third DoF in the hip joints of the legs. However, it will considerably increase the weight of our platform, thus drastically reduce the payload. Results of the experiments revealed that the developed landing gear can be successfully used not only for adaptive landing on uneven terrain, but also for complicated relief profile estimation. This has been confirmed by different landing tests (11 deg. and 3 deg. angle slopes, step, and plane). More detailed information about the test of the robot landing can be found in [Sarkisov et al., 2018].

As the next development stage of the DroneGear project we propose a novel non-traditional locomotion algorithm for quadrupedal robots, which have a special configuration of legs similar to DroneGear when legs are located in increments of 90

degrees relative to the central axis of the robot. Name of this approach is LocoGear [G. Yashin et al., 2020]. In the framework of this approach, the robot movement by one step consists of the movement of the robot center along a path consisting of a cycloid and parabola segments, and the movement of the legs along parabolic paths. Calculation and visualization of the algorithm were performed in Maple and MATLAB. Additionally, the experimental tests of the robot moving along a given path were performed. As a ground-truth motion capture VICON system was used.

4.2 System Overview

The robot is a hexacopter with landing gear attached to its bottom (Fig. 4-2 a)). The hexacopter is assembled from DJI Flame Wheel ARF KIT F550 frame with DJI E600 propulsion system and NAZA M flight controller. The landing platform consists of four 2-DoF legs, which are located in increments of 90 degrees relative to the central axis of the robot. The motion of the legs is executed by Dynamixel MX106 servomotors in the hip joints and Dynamixel MX28 servomotors in the knee joints. Also, the knee joints contain embedded optical torque sensors, which are made from compression springs and an encoder, located in a plastic body (Fig. 4-2

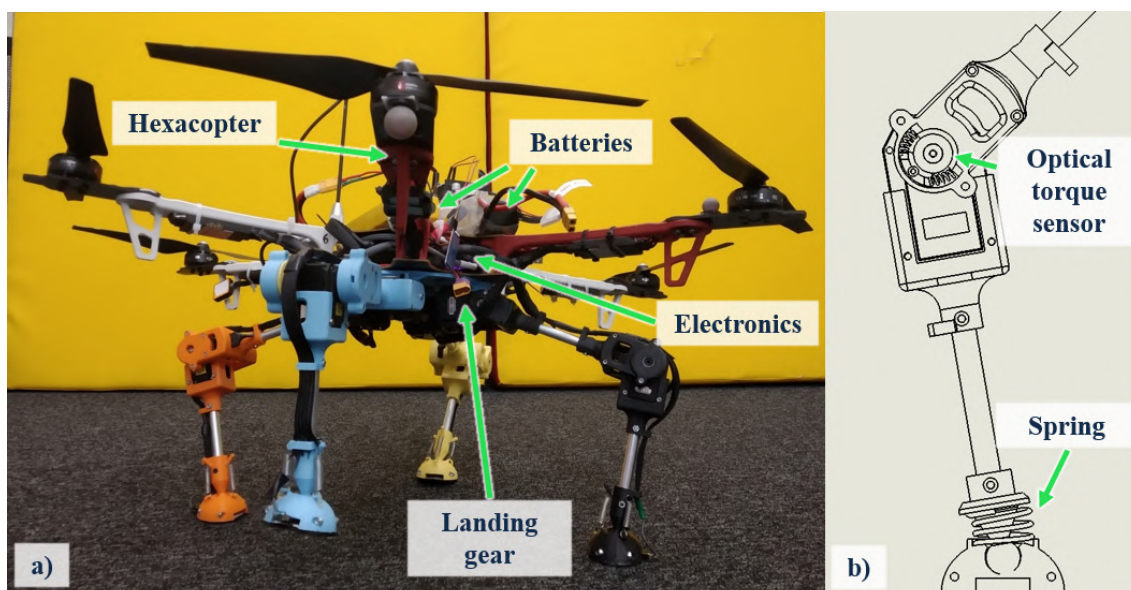


Figure 4-2: The landing platform for the multicopters (a) and the leg structure (b).

b)). These sensors provide passive compliance of the legs. Each leg has a passive footpad, which is connected via a spherical joint to the tip of the second link. The technical characteristics of the robot are presented in [Table 4.1](#).

| | |
|---|------------------|
| Maximum load of DJI E600 motors | 1600 g/axis |
| Maximum torque of Dynamixel MX106T at 12V | 8.4 N·m |
| Maximum torque of Dynamixel MX28T at 12V | 2.5 N·m |
| Work range of angle θ | 0-90 deg. |
| Work range of angle β | 0-100 deg. |
| Work range of angle α | 0-40 deg. |
| Total weight (with batteries) | 5.67 kg |
| The weight of one leg | 0.27 kg |
| Length of the link 1 | 0.164 m |
| Length of the link 2 | 0.156 m |
| Battery for DJI E600 motors | 5500 mAh, 22.2 V |
| Battery for Dynamixel servomotors | 5000 mAh, 11.1 V |

Table 4.1: Technical characteristics of DroneGear.

The legs' movement is controlled by Arduino and MATLAB code with applying [GUI](#). Reading data from the encoders and control of Dynamixel servomotors are implemented using Arduino Due, which receives commands from MATLAB GUI. Data exchange between Arduino and encoders (three channel optical incremental encoder module HEDS-9140#A00, codewheel HEDS-5140#A11) is performed via SPI protocol. Data exchange between Arduino and Dynamixel servomotors is performed using a buffer driver. Wireless communication between Arduino and the computer is implemented using Bluetooth module HC-05. The electrical circuit of the robot is presented in the [Appendix B](#). [GUI](#) displays actual information about current technical parameters of servomotors (voltage, speed, PID coefficients) and data from sensors. In addition, [GUI](#) shows a trajectory of the robot [CoM](#) and the actual position of robot legs in real-time. For this purpose, the code calculates the rotation angles of servo motors for their position specified in the [Cartesian coordinate system \(CCS\)](#). The scheme of the landing gear is shown in [Fig. 4-3](#). For the implementation of the robot movement, we set the motion path of the point, i.e., the [center of the robot \(CoR\)](#), which is located at the point equidistant from the hip joint axes which are belonged to the plane \varkappa_1 . After that, for each leg, we calculate

the position of leg attachment to the body ($X_{or}Y_{or}Z_{or}$, $X_rY_rZ_r$, $X_gY_gZ_g$, $X_bY_bZ_b$) and compute angles θ_i (hip joint) and β_i (knee joint) using forward kinematics.

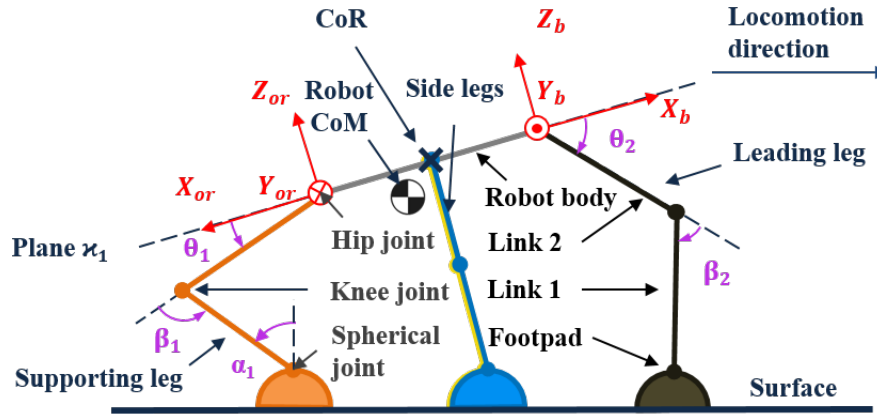


Figure 4-3: The scheme of LocoGear (in this scheme, the yellow leg is hidden behind the blue one).

4.3 Problem Statement

The location of the 2-DoF legs at an angle of 90 degrees to each other provides stable landing and steady location on uneven surfaces. However, such configuration is not suitable for typical locomotion strategy of multi-legged robots. The footpads can deviate from the link on an angle α about 40 degrees that imposes an additional constraint on the robot movement. In addition, the operating range of α is the main physical limitation of the step size of the robot without considering the length of the links. Taking into account the mentioned features of the robot, it was necessary to develop a new special locomotion strategy for the multicopter with the landing platform.

The nature of LocoGear locomotion is moving in a plane which contains the opposite legs (for example, black and orange in XZ plane). In this case, the legs lying in another plane (accordingly, the side legs: red and green in YZ plane) will be transferred to a new position simultaneously, it partially reminds a human walking on crutches. During crutch gait human lifts crutches and moves it forward, then he lifts and moves his legs to the new position, that is accompanied by the swing of the body [Wells, 1979]. In fact, the transfer of the side legs is the most difficult process

for this type of locomotion, since in this short time the supporting and driving legs will have to move the entire weight of the robot from one stable position to the next one. For a more detailed study of this process, we calculate the coordinates of the robot CoM at points of motion trajectory.

In framework of this project we focused on the development of the kinematic-based algorithm for locomotion of robots based on DroneGear’s principal scheme and test of this strategy on the real-life robot for its movement on a flat surface with simple obstacles such as the low steps.

4.4 Locomotion Algorithm

4.4.1 Movement Sequence

The proposed locomotion strategy is developed using heuristic approach based on an experimental search of the stable positions of the robot to perform its motion on one step (see Subsection 4.5.1). The phases of locomotion strategy are shown in Fig. 4-4. The robot movement on one step (Motion cycle) is implemented in five phases: firstly, the robot is leaning on the supporting leg to start motion (Fig. 4-4 (a)), during the second phase the leading leg rises and moves to a new position (Fig. 4-4 (b)), after this LocoGear transfers its CoM on the leading leg via the side leg movement (Fig. 4-4 (d)), at the fourth phase the robot pulls up the supporting leg and puts it on a new position (Fig. 4-4 (f)), finally, the robot is leveled in a new location (Fig. 4-4 (g)). Also, Fig. 4-4 (c, e) show the robot positions before and after CoM transfer respectively. Fig 4-4 (a-h) consist of 2 parts: XZ and XY plane views, additionally XY plane includes the position of the support polygon. Fig. 4-4 (h) contains schematic image of the robot in 3D-space, the trajectories of the robot CoR and CoM, trajectories of the legs during one step.

At each phase of the movement, the projection of the robot CoM is located in the support polygon (formed by external tangents (blue lines) to the circles of the adjacent footpads standing on the ground) in accordance with Fig. 4-4 that ensures a stable position of the robot [Vukobratović and Borovac, 2004]. However, the CoM transfer is a process at the border of stability since only two legs stand on

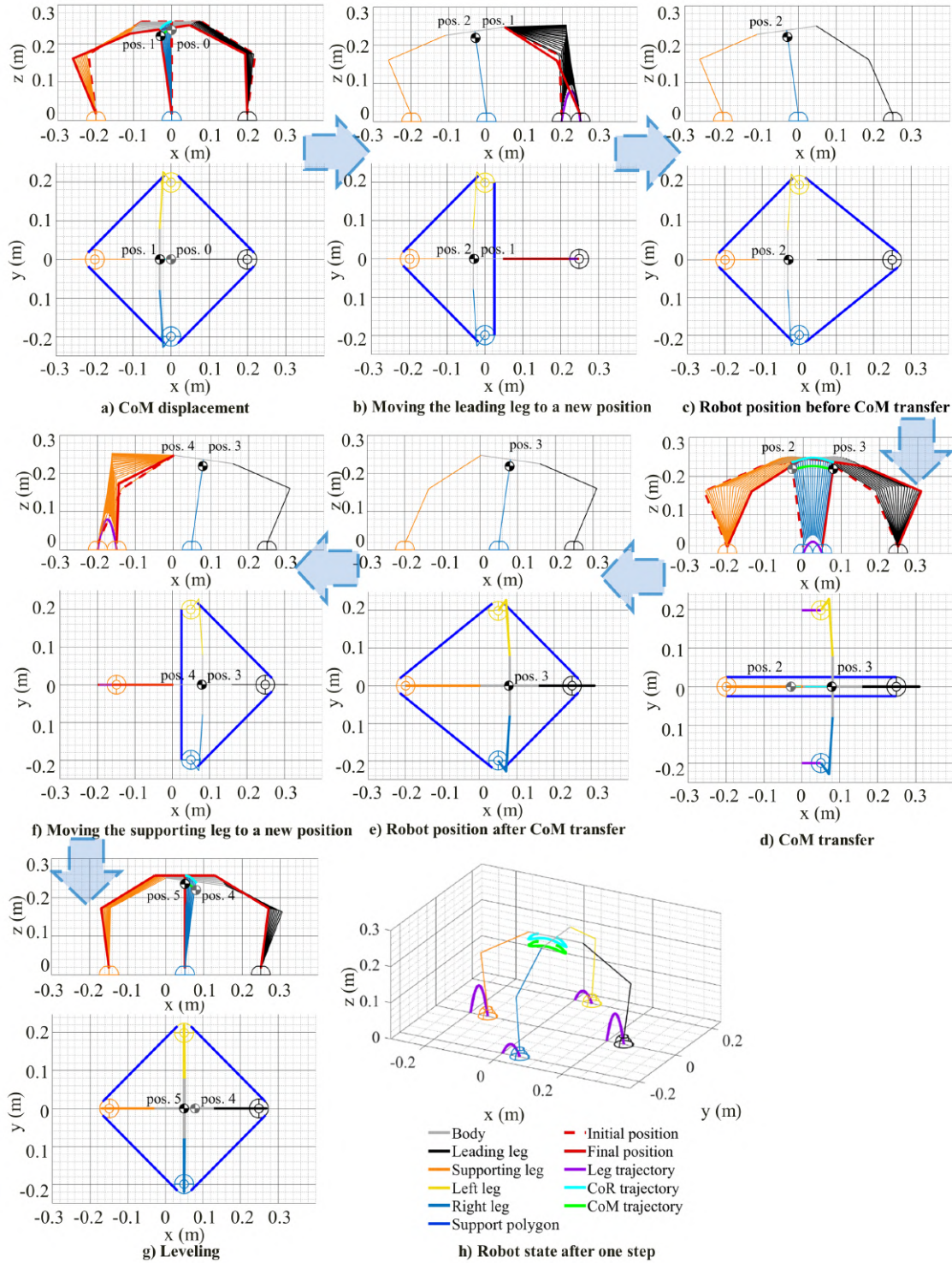


Figure 4-4: The locomotion algorithm. A schematic representation of the robot in profile is shown on the XZ plane. Position of the robot CoM relative to the support polygon (blue line around the footpads position) is shown on the XY plane.

the ground. During this action, the robot CoM must be in a rectangle 0.05 m wide (determined by the diameter of the robot footpad), whereas the CoM deviation in Y direction from the desired position can be up to 0.13 m. The probability of this deviation is caused by the passive spherical joints of the robot, the deviation value depends on CoM height and tangent of the roll angle ($h_{CoM} \cdot tg(\alpha)$). Thus, the CoM transfer should be performed rapidly.

For the proposed strategy we identify three modes of robot movement: the inclination on the supporting or leading leg, movement of one leg to a new position and the third one is the transfer of CoM with the raised side legs. Directly during the last mode of movement, the robot moves to a new position. Each of these modes should be defined by a corresponding equation.

4.4.2 Kinematic Model

Authors of the article [Shao et al., 2011] were inspired by biological motion and tested the mixed parabola method as the traveling paths over obstacles. Their experience showed that using a trajectory containing parabola segments allows to smoothly bend around obstacles, that is necessary for the robot when moving along uneven terrain. Thus, we chose a parabola trajectory for moving legs to a new position. The leg trajectory is defined by parameters of the initial state (x_{l0}, z_{l0}), step length (l_{step_x}), and lifting height of the legs (h_{step}). Likewise, robot inclination is carried out along the parabola, that ensures uniform movement of the robot with a small inclination angle and robot squat depth. CoR trajectory is defined by the initial state (x_{CoR0}, z_{CoR0}), inclination angle (ψ_0), and robot squat depth (h_{sd}). CoR trajectory during inclination, the trajectory of the leading leg at its transfer to a new position and the scheme of LocoGear after these phases are shown in Fig. 4-5. The system of equations for CoR (4.1) and leg parabolas (4.2) are followings:

$$\begin{cases} z_{inc} = c_{inc} \cdot (x_{inc} - x_{inc_pt})^2 + z_{CoR0} \\ x_{inc} \in [x_{CoR0}; x_{CoR0} \pm s \cdot (z_{CoR0} - h_{sd}) \cdot tg(\psi_0)] \\ c_{inc} = \frac{z_{CoR0} - h_{sd}}{((z_{CoR0} - h_{sd}) \cdot tg(\psi_0))^2}, \end{cases} \quad (4.1)$$

$$\begin{cases} z_{lift} = c_{lift} \cdot (x_{lift} - x_{lift_pt})^2 + z_{l0} + h_{obst} \\ x_{lift} \in [x_{l0}; x_{l0} + s \cdot l_{step_x}] \\ c_{lift} = \frac{h_{obst} - h_{step}}{(x_{lift_pt} - x_{l0})^2}, \end{cases} \quad (4.2)$$

where x_{inc_pt} and x_{lift_pt} are the X -coordinates of vertex of a parabola for inclination phase and leg lifting respectively, s takes the value of 1 or -1 depending on the movement direction (forward or backward respectively), h_{obst} is the obstacle height.

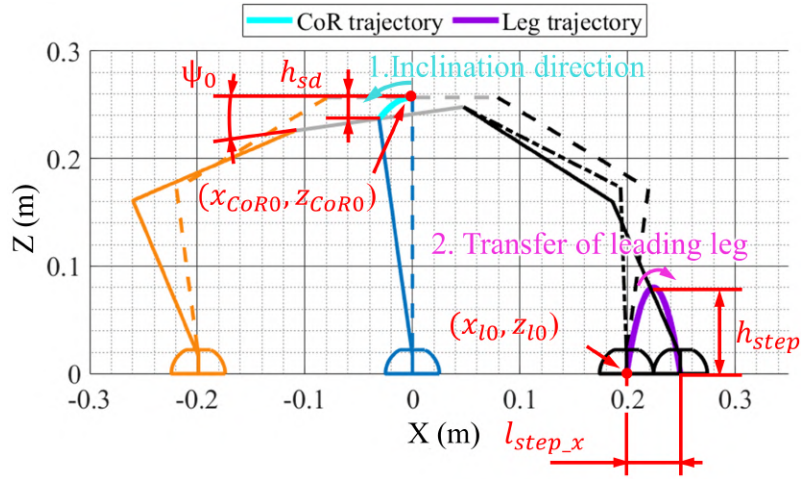


Figure 4-5: The scheme of LocoGear after the inclination and transfer of the leading leg.

In an article devoted to the research of the CoM motion in human walking, Carpentier et al. [2017] showed that the human CoM trajectory follows a curtate cycloid during human walking, and the profile of this cycloid depends on the height of the subjects. Based on this research and our experimental results (see Subsection 4.5.1), we chose a curtate cycloid as the CoR trajectory for CoM transfer in a new position (Fig. 4-6). CoM transfer along the curtate cycloid provides smooth movement of CoM and allows to raise the side legs to a small height. At this phase, the transfer of the side legs in the new position is also carried out along the parabola, but with a lower height ($h_{step} \cdot 3/8$). A shape of the curtate cycloid for CoR motion is represented by the following equations:

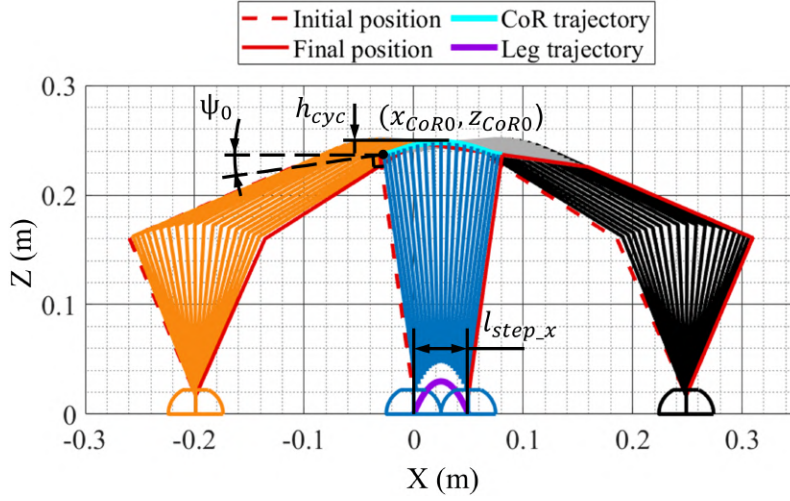


Figure 4-6: The sequences of the robot locomotion along a curtate cycloid (orange, blue and black lines are the intermediate positions of supporting, side and leading legs accordingly).

$$\begin{cases} x = x_{CoR0} + a \cdot \psi - b \cdot \sin(\psi) \\ z = z_{CoR0} + a - b \cdot \cos(\psi), \end{cases} \quad (4.3)$$

where a is the radius of a rolling circle, b is the distance between the center of the rolling circle and the desired point of the path ($b < a$). The robot body takes the position of the tangent line to the selected cycloid. Changing the parameters a and b , we can set the required step size and the maximum lifting height of the robot CoR. Knowing the step size (l_{step_x}), we can calculate the distance between the start and end point of the curtate cycloid in the interval from 0 to 2π . Then we substitute the $\psi = 2\pi$ in the first equation of (4.2) and get the value of the parameter a , and substitute the $\psi = \pi$ in the second equation of (4.2) for calculating b :

$$\begin{cases} a = \frac{l_{step_x} + 2 \cdot z_{CoR0} \cdot \tan(\psi_0)}{2 \cdot \pi} \\ b = h_{cyc} - a, \end{cases} \quad (4.4)$$

where l_{step_x} is step size, ψ_0 is the robot pitch angle in the initial position of the CoR transfer, h_{cyc} is the cycloid height. Using (4.4) we can experimentally determine value h_{cyc} to ensure the transfer of the side legs without touching the ground.

The trajectory between the phases is discretized in such way that the largest

interval between the previous and next values of the servomotors' angles is divided into steps of 1 degree. Accordingly, all servomotors move to the desired position at the same time, which allows performing a smooth movement of the robot.

In accordance with selected movement strategy the adjustment of the robot movement is carried out by selecting the following six parameters: initial state (joint angles at initial position), inclination angle (ψ_0), robot squat depth (h_{sd}), lifting height of the legs (h_{step}), cycloid height (h_{cyc}) and step length (l_{step_x}).

4.4.3 Calculation of the Robot Center of Mass

Fig. 4-7 contains a scheme of landing gear with the location of the CoMs of main robot components. In the initial position, the angles θ and β are the same for all legs and the robot body is parallel to the plane on which the robot stands. At this condition, the center of CCS $X_0Y_0Z_0$ is at equal distances from the centers of the spherical leg joints (point A). The X_0Y_0 plane lies in plane κ_2 which passes through the centers of the spherical joints of the legs.

In Fig. 4-7 $X_{fi}Y_{fi}Z_{fi}$, $X_{l1i}Y_{l1i}Z_{l1i}$, $X_{l2i}Y_{l2i}Z_{l2i}$, $X_bY_bZ_b$, are CCS of footpads, leg links 1 and 2, and the rest of the robot including multicopter (Body) respectively.

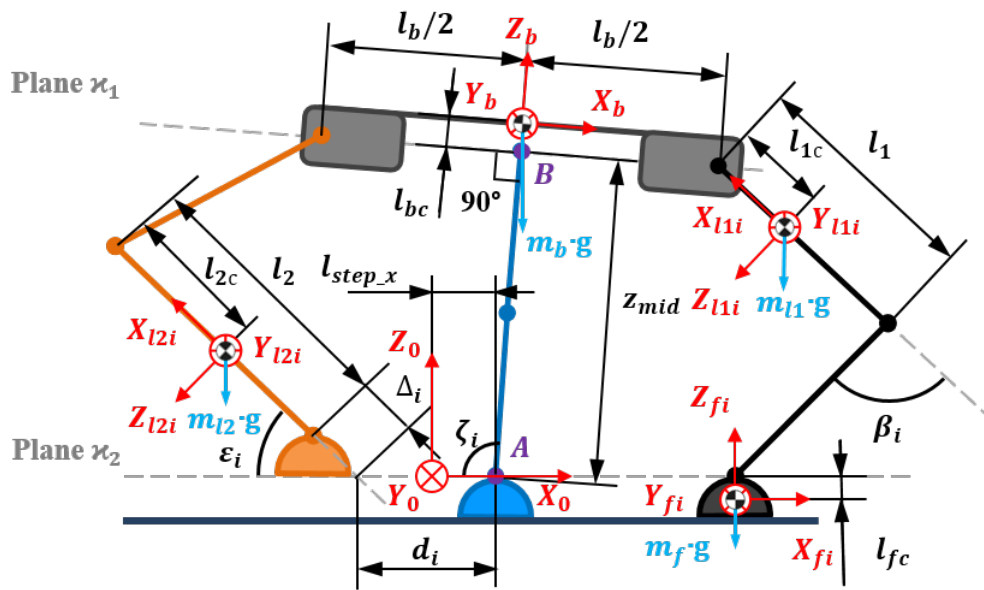


Figure 4-7: The scheme of LocoGear for calculation of the robot CoM.

These CCSs are associated with their CoMs. m_f, m_{l1}, m_{l2}, m_b are masses of footpad, leg link 1, leg link 2 with servomotor located in the knee joint, and Body, which includes the entire mass of the multicopter, the control electronics, battery, the connector of legs to the UAV and hip joint servomotors; l_{fc}, l_{1c}, l_{2c} are the distances from the center of the spherical, knee and hip joints to the CoMs of footpad, link 1 and link 2 respectively; l_{step_x}, l_{step_y} are the distances from the starting point along the X and Y axes; l_{bc} is the distance between point B which is equidistant from the axes of the hip joints and CoM of Body; d_i is the distance between point A and the center of spherical joint of i -th leg or an intersection point of a plane \varkappa_2 with a virtual extension of link 2 in case of i -th leg lift; ζ_i is the angle of inclination of the robot or the angle between the plane \varkappa_2 and the segment AB ; z_{mid} is the distance between point A and B (point B is the CoR), also the segment AB is the perpendicular to plane \varkappa_1 which passes through the centers of the hip joints of the legs. For ease of calculation, we consider that Body CoM is projected at point B that is performed by the symmetrical arrangement of the payload (control electronics and battery) on the robot body relative to the X_b and Y_b axes.

In accordance with the selected algorithm, the robot has three modes of locomotion phases: (a) leading or supporting leg is lifted, (b) side legs are lifted, (c) all legs are on the ground. The third mode can be calculated as a special case of the first or second mode when the distance between each leg and the surface equals zero. Cases (a) and (b) are accompanied by an additional calculation of the gap (Δ_i) between legs and the plane \varkappa_2 . Coordinates of the robot CoM are determined by the following formula:

$$\vec{r}_c = \frac{\sum_i (\vec{r}_i \cdot m_i)}{\sum_i m_i}, \quad (4.5)$$

where \vec{r}_c is the radius vector of the robot CoM, \vec{r}_i and m_i are the radius vector and mass of the i -th component of the robot, respectively. We found \vec{r}_i for each i -th component as a product of the translation (D_i^{i-1}) and rotation (R_i^{i-1}) transformation operators from global CCS $X_0Y_0Z_0$ to CCS of the CoMs of the robot components. These matrices are dependent on the parameters which are shown in Fig. 4-7:

$$\begin{cases} T_{fi}^0 = f(d_i, l_{step_x}, l_{step_y}, l_{fc}, \Delta_i) \\ T_{l2i}^0 = f(d_i, l_{step_x}, l_{step_y}, \zeta_i, \varepsilon_i, l_2, l_{2c}, \Delta_i) \\ T_{l1i}^0 = f(d_i, l_{step_x}, l_{step_y}, \zeta_i, \varepsilon_i, \beta_i, l_1, l_2, l_{1c}, \Delta_i) \\ T_b^0 = f(l_{step_x}, l_{step_y}, \zeta_{i+2}, \zeta_i, z_{mid}, l_{bc}, \Delta_{side_legs}). \end{cases} \quad (4.6)$$

Variables ζ_i , d_i , z_{mid} , ε_i and Δ_i are calculated using trigonometric calculations. Since the actual robot movement occurs during the transfer of the side legs, l_{step} are calculated as the differences between current and previous values d of supporting leg:

$$l_{step} = d_{sup_cur} - d_{step}. \quad (4.7)$$

Since the heuristic method assumes an experimental selection of angles for the phases of movement, it was necessary to find an approach to calculate the robot's trajectory. Thus we can use equations (4.5-4.7) for calculation of CoR position at the stage of the heuristic selection of phase positions (see Subsection 4.5.1). When the robot movement is determined as in Subsection 4.4.2, the transfer matrices 4.6 will depend on CoR coordinates (x, y, z) , joint angles (θ_i, β_i) , geometrical robot parameters (l_i) , and inclination angle (ψ) .

4.4.4 Dynamic Model

An explanatory scheme for the calculation of dynamic loads is shown in Fig. 4-8. In this scheme N_i is the ground reaction force for i-th leg; T_{θ_i} and T_{β_i} are the servomotor torques in hip and knee joints; V_b , V_{1i} , V_{2i} , and V_{fi} are the velocities of the body, link 1, link 2 and the footpad, respectively; ω_b , ω_{1i} , ω_{2i} and ω_{fi} are the angular velocities of the body, link 1, link 2 and the footpad, respectively. The Lagrangian dynamic formulation is the most popular for calculating the motion equations of a walking robots [Formalskii, 1982, Kimura et al., 1989, Lee et al., 2014]. We use this method for the calculation of torques in the robot joints during the motion

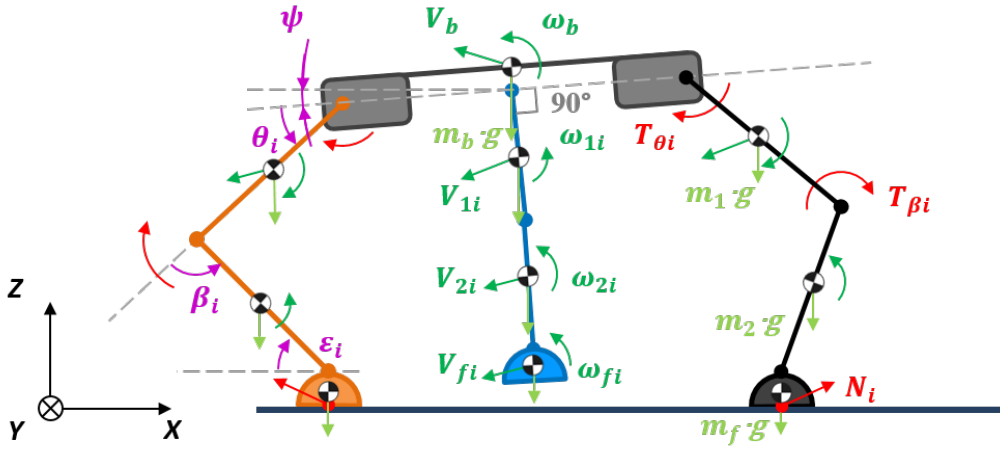


Figure 4-8: The robot scheme for calculation of the joint torques.

(4.8) with known equations of motion Subsection 4.4.2. The following assumptions were made for the calculation: the absence of slippage between footpads and the ground, the friction forces are not taken into account, the estimated dynamic model is performed without considering the springs in the joints.

$$\begin{cases} \frac{d}{dt} \left(\frac{\partial L}{\partial \dot{q}_i} \right) - \frac{\partial L}{\partial q_i} = Q_i \\ q = [x, z, \psi, \theta_l, \beta_l, \theta_s, \beta_s, \theta_{si}, \beta_{si}] \end{cases}, \quad (4.8)$$

where Q_i is the generalized non-conservative force, $L=K-U$ is Lagrangian function, which is equal to the difference between kinetic (K) and potential (U) energies. The calculation of the kinetic and potential energies is presented in the Appendix C. To account the leg raising, we introduced a variable of the leg state H_i , which takes the value 0 or 1 if the leg is on the ground or raised, respectively. Following the article [Boix et al., 2017], we can write the equation for calculation of the generalized forces as follows:

$$Q_i = T + J^T \cdot N_i, \quad (4.9)$$

which can be written in full form as follows:

$$Q = \begin{bmatrix} 0 \\ 0 \\ T_{\theta_s} - T_{\theta_l} \\ 2\dot{T}_{\theta_{si}} \\ 2\dot{T}_{\beta_{si}} \\ T_{\theta_l} \\ T_{\beta_l} \\ T_{\theta_s} \\ T_{\beta_s} \end{bmatrix} + \frac{\partial(x_{f_{si}}, y_{f_{si}}, z_{f_{si}}, x_{fl}, z_{fl}, x_{fs}, z_{fs})}{\partial(x, z, \psi, \theta_l, \beta_l, \theta_s, \beta_s, \theta_{si}, \beta_{si})} \cdot \begin{bmatrix} 2 \cdot N_{x\theta_{si}} \cdot H_{si} \\ 2 \cdot N_{y\theta_{si}} \cdot H_{si} \\ 2 \cdot N_{z\theta_{si}} \cdot H_{si} \\ N_{x\theta_l} \cdot H_l \\ N_{z\theta_l} \cdot H_l \\ N_{x\theta_s} \cdot H_s \\ N_{z\theta_s} \cdot H_s \end{bmatrix}. \quad (4.10)$$

If i -th leg is raised, N_i will be equal to 0 in (4.10). Using forward kinematics, we get the following expressions for calculation of footpad coordinates:

$$x_{fl} = x + \frac{l_b}{2} \cdot \cos(\psi) + l_1 \cdot \cos(\theta_l - \psi) + l_2 \cdot \cos(\beta_l + \theta_l - \psi), \quad (4.11)$$

$$z_{fl} = z + \frac{l_b}{2} \cdot \sin(\psi) - l_1 \cdot \sin(\theta_l - \psi) - l_2 \cdot \sin(\beta_l + \theta_l - \psi) - l_{fg}, \quad (4.12)$$

$$x_{fs} = x - \frac{l_b}{2} \cdot \cos(\psi) - l_1 \cdot \cos(\theta_s + \psi) - l_2 \cdot \cos(\beta_s + \theta_s + \psi), \quad (4.13)$$

$$z_{fs} = z + \frac{l_b}{2} \cdot \sin(\psi) - l_1 \cdot \sin(\theta_s + \psi) - l_2 \cdot \sin(\beta_s + \theta_s + \psi) - l_{fg}, \quad (4.14)$$

$$x_{f_{si}} = x + (l_1 \cdot \sin(\theta_{si}) + l_2 \cdot \sin(\beta_{si} + \theta_{si})) \cdot \sin(\psi), \quad (4.15)$$

$$y_{f_{si}} = l_1 \cdot \cos(\theta_{si}) + l_2 \cdot \cos(\beta_{si} + \theta_{si}) + \frac{l_b}{2}, \quad (4.16)$$

$$z_{f_{si}} = z - (l_1 \cdot \sin(\theta_{si}) + l_2 \cdot \sin(\beta_{si} + \theta_{si})) \cdot \cos(\psi) - l_{fg}. \quad (4.17)$$

Thus, we deduced a system of 9 equations with 13 unknowns (servomotor torques and reaction forces). The problem of the lack of equations can be solved in two ways. (4.8) can be supplemented by three constraint equations between the robot and the floor and solved using Lagrange multipliers [Zamani et al., 2011, Lee, 2013]. In the second approach we can write the equation of conservation of momentum in accordance with the kinetostatic methods [Li et al., 2015]. Based on the second method

we wrote three equations of the equality to zero the robot main angular momentums around X_{CoR} and Y_{fi} relative to the center of pressure of i -th footpad. These expressions were derived individually for each three types of movement (inclination, leg raising, and CoM transfer):

$$\begin{cases} \sum M_{yfi} = 0, i = 1..3 \\ \sum M_{xCoR} = 0. \end{cases} \quad (4.18)$$

Knowing the law of motion of the robot in space, we derived the expressions for calculation of the servomotor torques using Maple. Fig. 4-9 shows the change of the angles of the hip and knee joints, inclination angle, the servomotors torques in time, and the sequences of the robot locomotion during Motion cycle with raising the leading leg on the obstacle. At the first stage, we observe a sharp decrease in the servomotor loads of the leading and supporting legs, since at this time interval the robot deviates from the equilibrium position and takes the necessary position under the influence of gravity. In this case, the load on the side legs varies slightly due to the robot inclination at a small angle. During phases 2 and 4, the torque increases for the legs remaining on the ground. At the third phase, the load is redistributed from the supporting leg to the lead. It is also worth noting the presence of jumps in loads during the transition of one phase to another. This is due to the fact that in the proposed dynamic model, when the leg is raising or lowering, the reaction force abruptly disappears or appears at the contact point of the moved leg. During the fifth stage we observe the increasing of the servomotor torques caused by robot movement in the equilibrium position.

4.4.5 Simulation of the Robot Motion

For estimation of the ability of the robot motion on uneven surface we consider a special case when the robot moves on the plane with a rectangular step of 0.04 m high (h_{obst}). This case can be scaled with addition of the map with different relief features, which should be characterized by their coordinates and shape parameters.

The boundary of the rectangular step is defined by length (l_{obst}), width (w_{obst}),

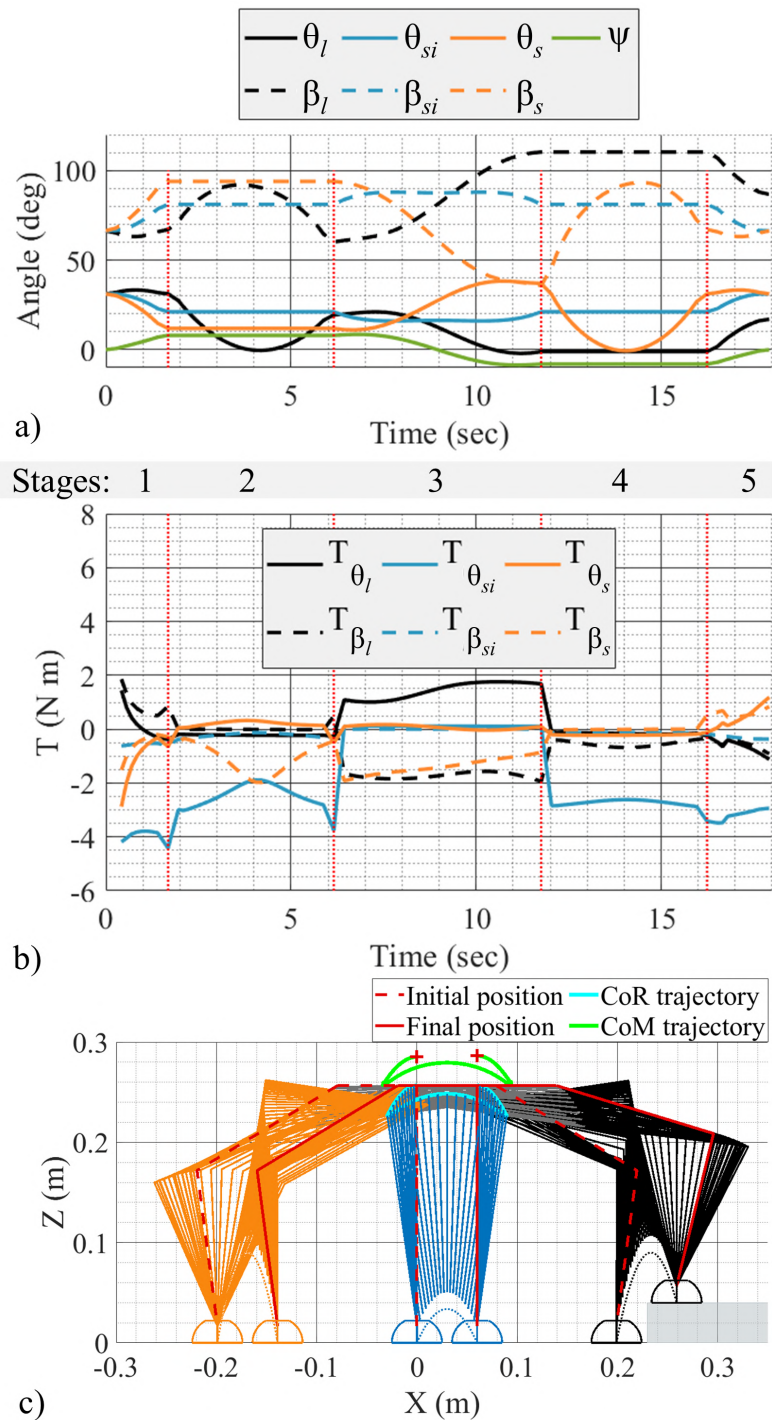


Figure 4-9: Joint and inclination angles (a), servomotor torques (b) vs. time, and the sequences of the robot locomotion (c) during the robot movement to step by the leading leg on the obstacle.

height (h_{obst}) and coordinates (x_{obst}, y_{obst}) , which correspond to the obstacle corner with the smallest coordinates along the axes X and Y . On the Fig. 4-10 we showed the movement of the robot along random trajectory after the landing on the step (yellow and black were located on the obstacle). The obstacle under the robot's foot is taken into account when the foot is moved to a new position; for this we check intersection of the pad setpoint with obstacle's surface. In case of the presence of intersection, the leg trajectory is calculated taking into account the non-zero height of obstacle in (4.2).

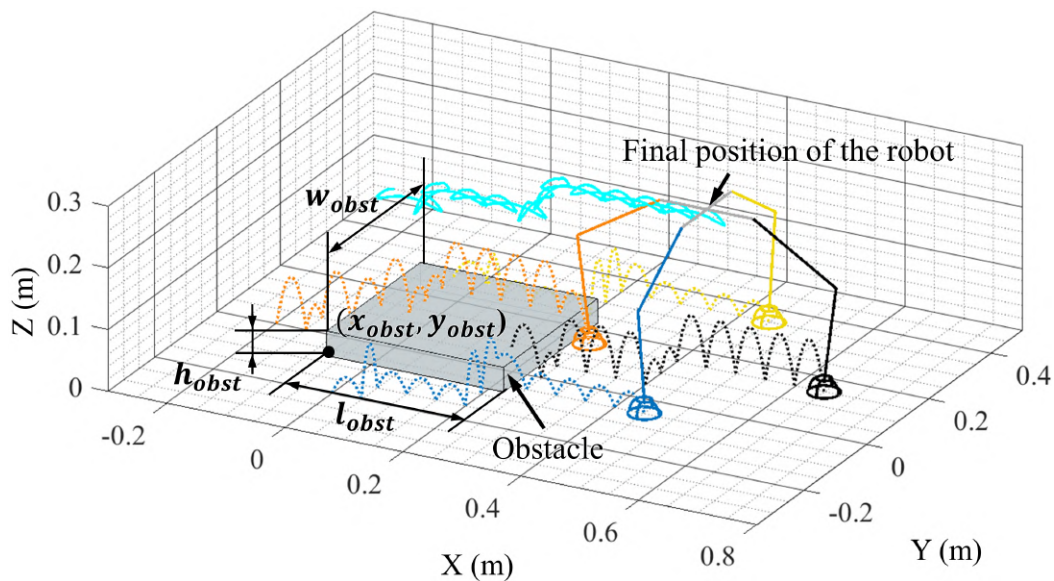


Figure 4-10: The movement of the robot along random trajectory after landed on the step (blue, black, orange and yellow dashed lines are the trajectories of legs, turquoise line is the motion trajectory of CoR).

4.5 Experimental Results

In the scope of the robot locomotion analysis, we conduct a series of experiments to define the optimal trajectory of the **Motion cycle**, then we test the robot motion among the predetermined trajectory. Video clip dedicated to LocoGear algorithm can be found at the following link: https://youtu.be/Ug_XYDpnK10. In this video we show the landing procedure of the flying robot, visualizations of the LocoGear **Motion cycle** and locomotion algorithm dealing with an obstacle. Finally, we demonstrate the motion of the robot along the line.

4.5.1 Parameter Configuration

In the framework of the heuristic analysis of the robot locomotion, we wrote GUI, which is shown in Fig. 4-11. Using this interface, we can manually enter the desired position of all legs, control each servomotor's position and the direction of movement of the robot, move the robot in each separate phase, and switch between landing and walking modes. In accordance with the target servomotor's positions, the GUI displays a schematic representation of the robot and the trajectory of the robot CoM. For the primary coordinates selection of the phases of the Motion cycle, we carried out three stages of testing using developed interface.

Firstly, we defined the stable positioning of the robot on three legs. To achieve this, we did experiment on different combinations of the distance d_i between side legs and distances between point A and supporting leg during the robot inclination on this leg from the initial position.

In the second step, we analyze the forward movement of the leading leg. In

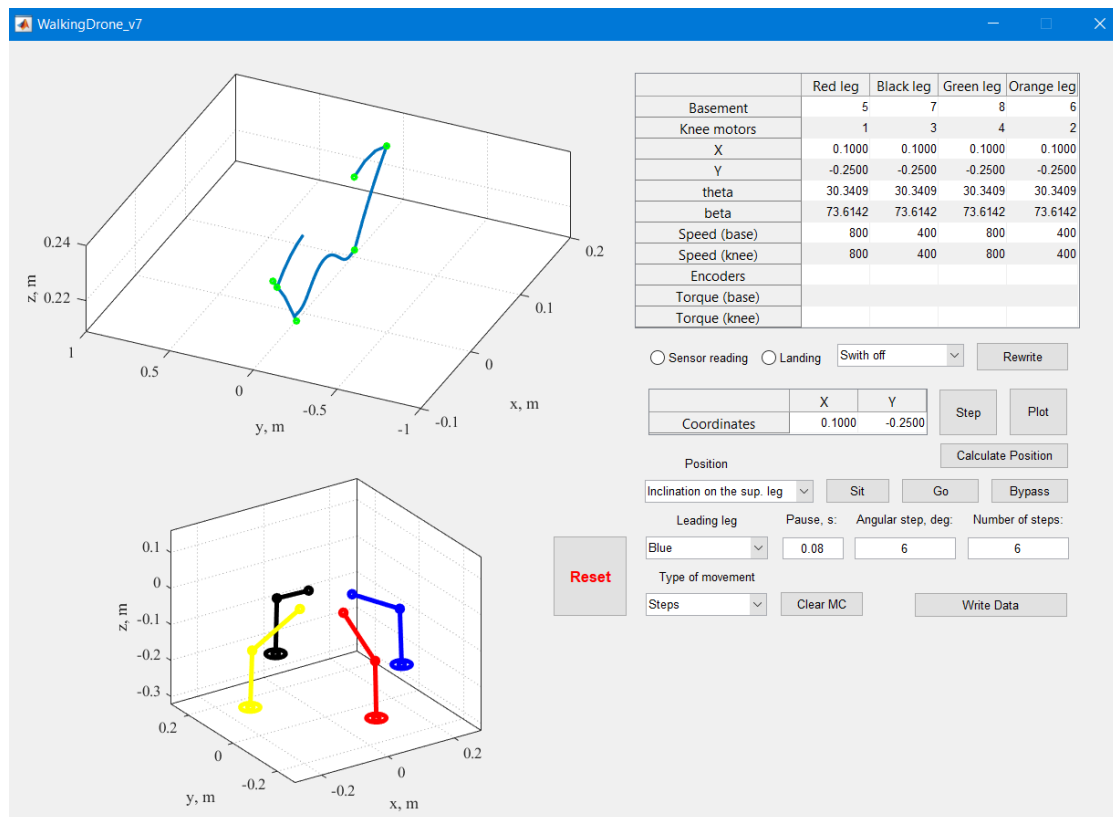


Figure 4-11: GUI to control DroneGear at the heuristic analysis.

this case, incorrect positioning leads to instability and probable swaying back and forth. Stability is provided when the CoM projection is in the supporting polygon. The small distance between the leg and point A (d_i) can lead to rolling over. A larger value of this parameter reduces the step size, and accordingly, the movement speed. Increasing d_i reduces the distance between the robot body and ground, and respectively working ranges of θ and β are decreased as well, that directly influences on the step size.

The most challenging phase of the Motion cycle is the moving of the robot CoM from the supporting leg to the leading leg. The robot moves to a new position immediately during this step, thus, the previous phases are the preparation to the motion. At this phase, the robot should lift the side legs up and quickly move the CoM to a new position, so as not to incline to the side until the end of the movement. Thus, at this moment, the motors of the supporting and leading legs undergo maximum load. If the trajectory is incorrectly selected, the robot tries to lift up and remains in place, which is possible with an excessively large distance d_i . Also, the robot can tip over if the distance between the ground and the side legs is too small. This is due to the fact that the robot has time to slightly tilt to the side and one of the legs remains in the same place, while the leading leg will pull the robot behind it.

Photos of each phase of the Motion cycle are shown in Fig. 4-12. Fig. 4-12 (e) demonstrates a slight side movement during this step. Fig. 4-12 (h) also shows a slight inclination of the robot to the right. At other phases, the robot motion is performed stably. In all experiments, we visually detected the deviation from the desired position. After that, we check data about real angles from encoders of torque sensors in knee joints. In Fig. 4-13 the desired and real values (from encoders) of β are shown for seven phases of motion on one step. The deviation of β_{green} from the desired position at the end of the cycle occurred due to the fact that the robot took the final position with an inclination to the side leg.

We compared the calculated trajectory of the robot CoM (Curve 1) with the real movement of the CoR (Curve 2) at the stage of the heuristic selection of phase positions that is shown in Fig. 4-14 (a, b). The numbers on these images correspond

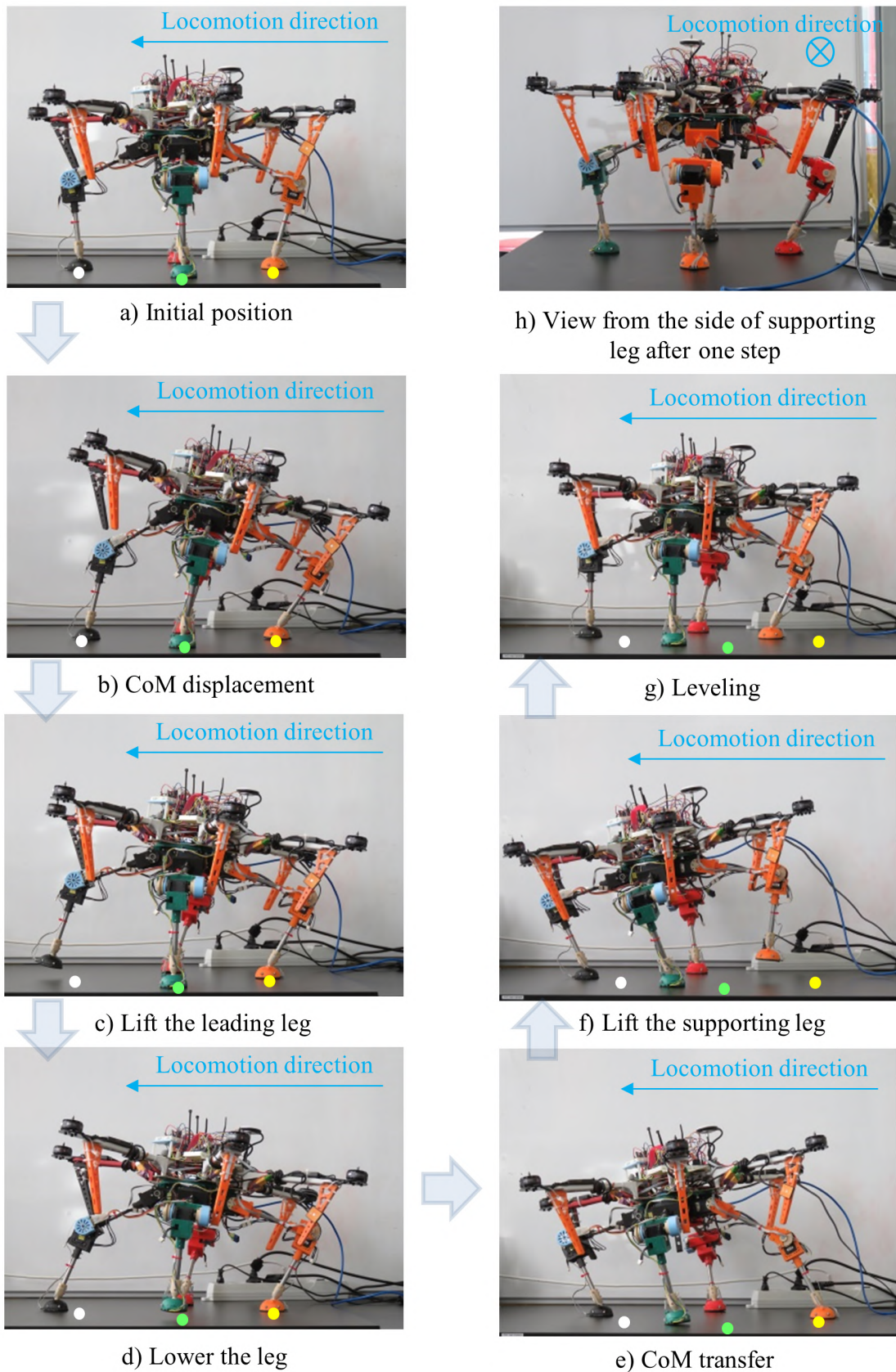


Figure 4-12: The phases of the *Motion cycle* (the white and yellow points are the initial positions of the leading and left leg respectively).

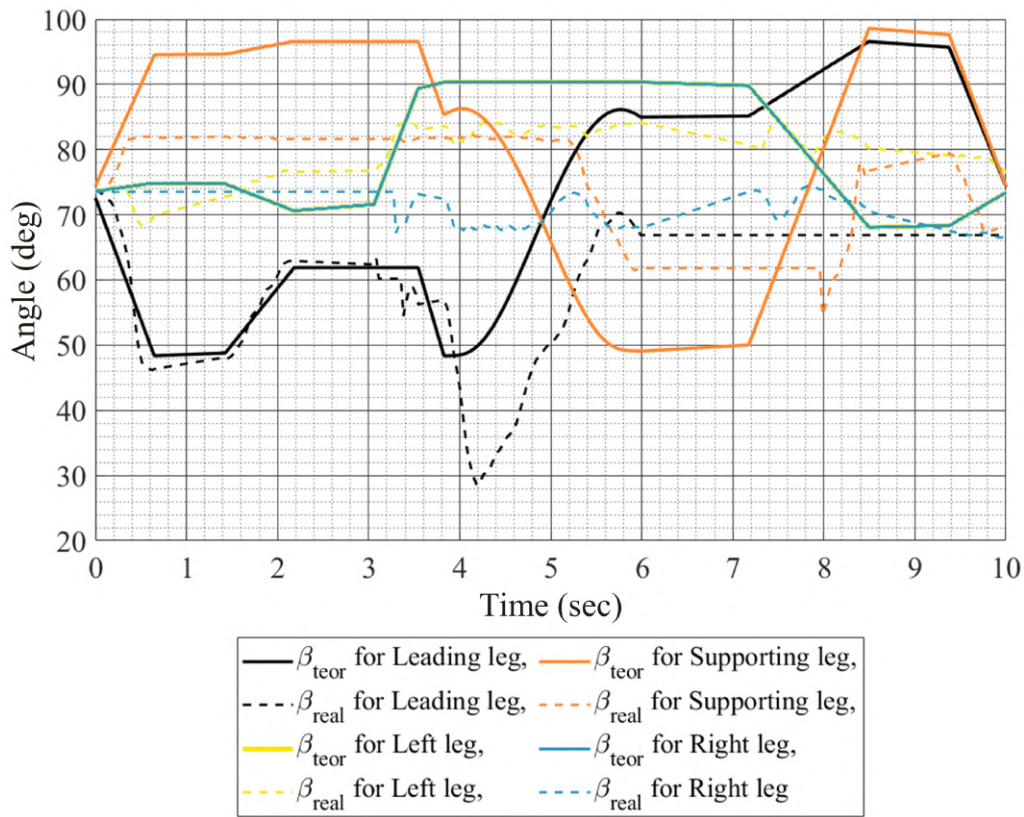


Figure 4-13: The desired and real values of β during one Motion cycle.

to the five phases of Motion cycle. The initial position of Curve 1 is combined with the initial position of Curve 2 for easy comparison. The robot was tested on a rough surface. Tracking of the robot position is performed using the VICON Mocap. The position of point 1 is different because at this point the CoM is shifted due to the increased load on the springs in the torque sensors. Curve 1 and Curve 2 have similar behavior; however, the curves have a significant difference at phases 3 and 4. The reason for this is that after the CoM transfer the robot deviated to the left before touching the ground with the side legs (Fig. 4-14 (b)). Oscillations during locomotion in the YZ plane occur because of the presence of the spring in the spherical and knee joints.

Since the curve connecting positions 2 and 3 (Fig. 4-14 (b)) resembles a sinusoid or curtate cycloid, it makes sense to set the motion equation for the CoM transfer in according to one of these curves. Based on [Carpentier et al., 2017] and the results of the heuristic selection, a curtate cycloid was chosen as the trajectory of the CoM

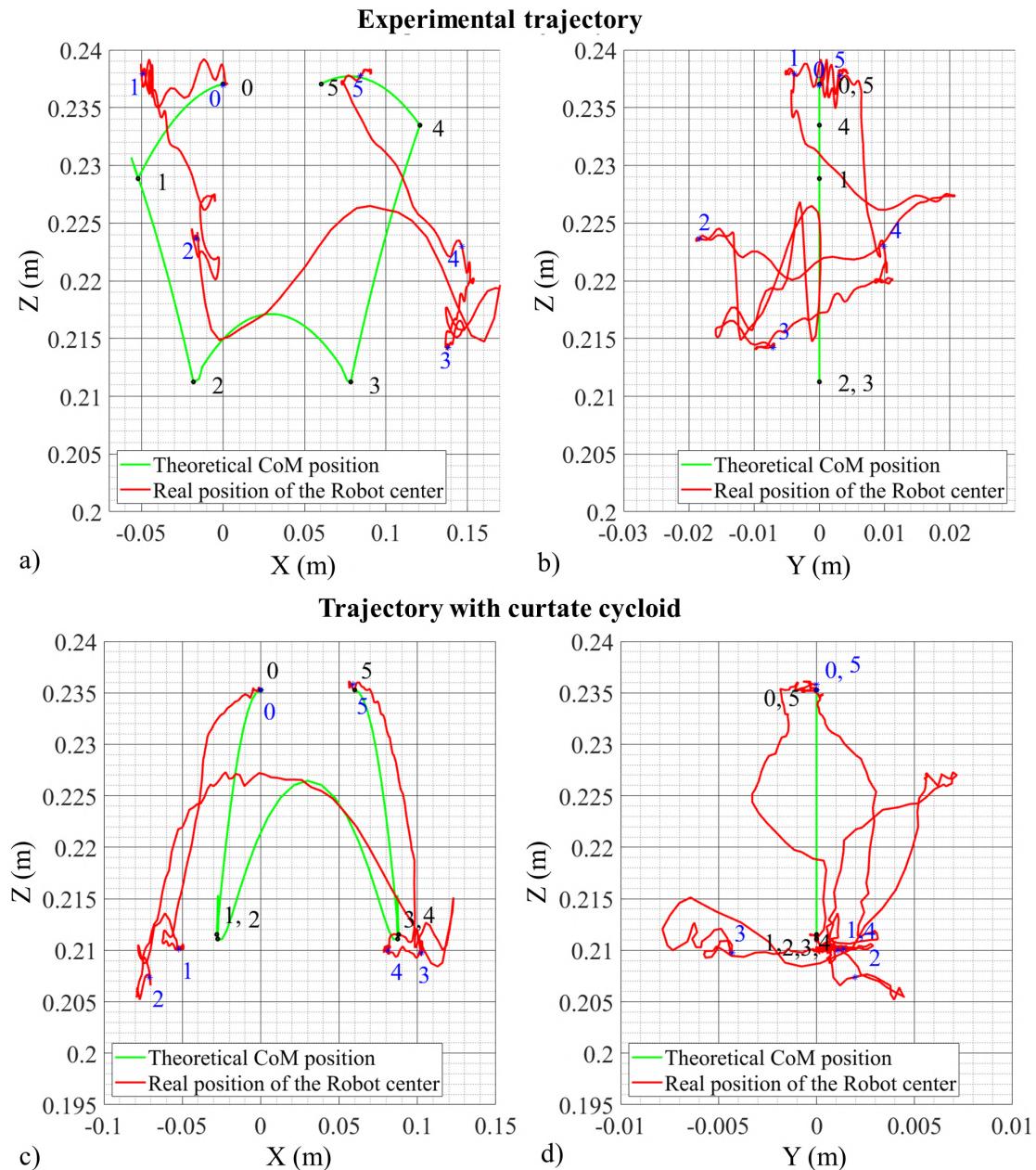


Figure 4-14: Trajectories for 2 experiments of the *Motion cycle* in XZ frame (a, c) and YZ frame (b, d).

transfer. In Fig. 4-14 (c, d) Curve 1 and 2 are shown for the developed algorithm. Profile of Curve 2 coincides with Curve 1 in frame XZ , however, oscillations at phases 3 and 4 are still existed due to springs in the joints (Fig. 4-14 (d)). An additional reason for these disturbances can relate to the backlash in the gears of the Dynamixel servomotors.

4.5.2 Experiment of the Path Following

The experiment presents the robot movement along a straight line. For this goal, the robot should repeat *Motion cycle* ten times. The size of one step equals 0.06 m, thus the total path length should be 0.6 m. In Fig. 4-15 we showed the results of five experiments (# 1 and # 2 for *Motion cycle* without cycloid, trajectory # 3, 4, 5 with using cycloid during the CoM transfer).

For experiments #1 and #2 the standard deviation yaw angle of the end position

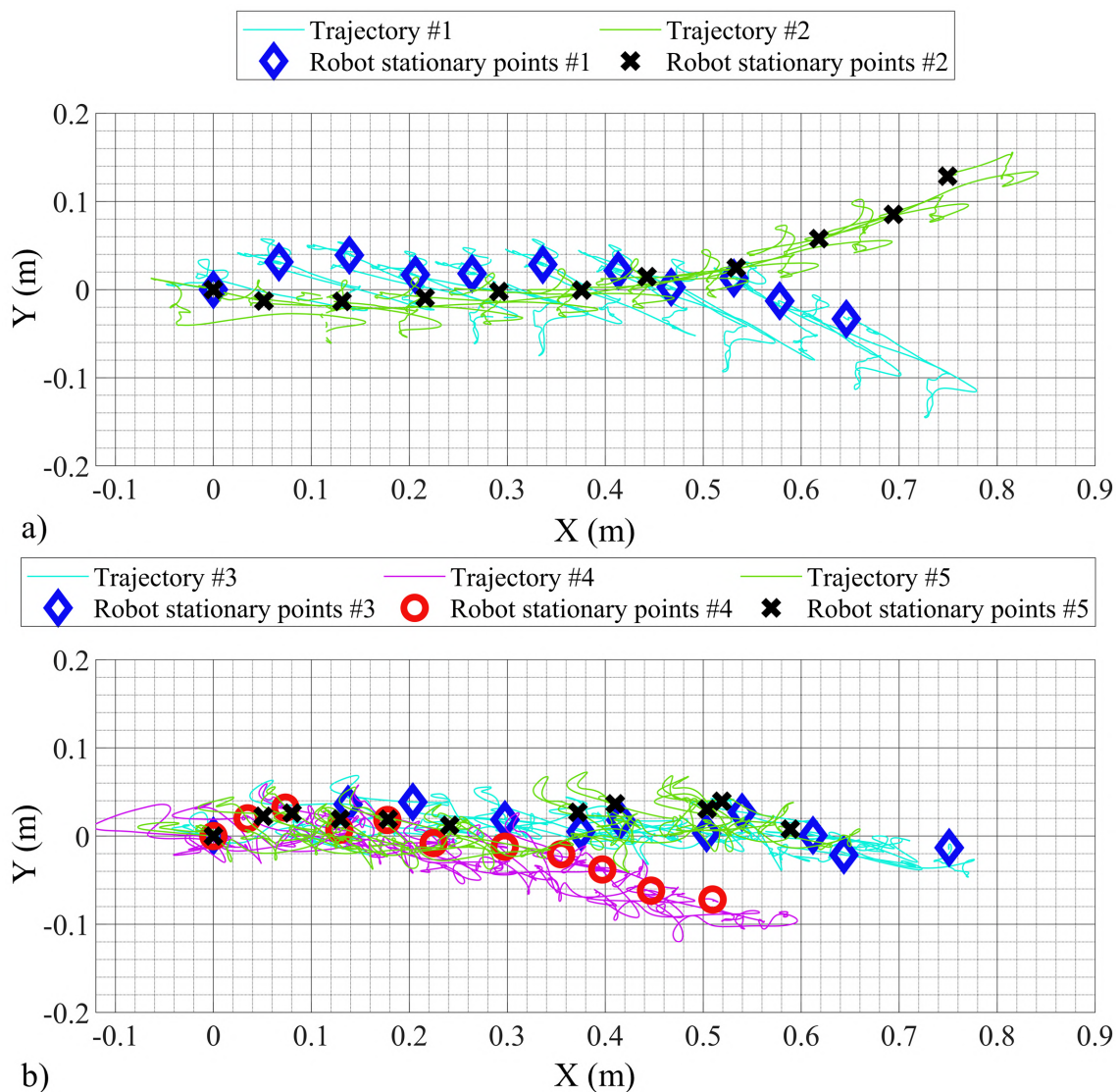


Figure 4-15: Real movement paths of the CoR for five experiments at the specifying rectilinear movement (a) for *Motion cycle* without cycloid, b) with using cycloid during the CoM transfer).

of **Motion cycle** from the predetermined path is 11.2 degree at 2.07 cm step size standard deviation. At first experiment the robot movement deviated to the right while the movement was fairly stable. During the second experiment, the swinging motion from side to side was experienced permanently. At the same time, we observe stable motion with some symmetric deviation of the end position of **Motion cycle** from the predetermined path, but the deviation to the left dominates at the end of the movement. This behavior corresponded to the previous results when the deviation of the robot to the left side was noted. In both experiments, there is also a tendency of the robot moving a longer distance than planned. This is due to the fact that at the transfer of the side legs the leading and supporting legs are under increased load, and the distance between them slightly increases due to slippage and compliance of the springs in the joints. For experiments # 3, 4 and 5 with the **CoM** transfer along the curtate cycloid, we observe more stable locomotion, the standard deviations of yaw angle and step length are of 9 degree and 0.98 cm, respectively. The average speed of robot motion is equal to 0.75 cm/sec. In some cases, the robot performs one-time deviations from the trajectory (Trajectory # 4). The reason for this is the side shift of Body **CoM** due to the presence of the springs in the joints. The development of a feedback controller based on the data from the encoders can correct each position of the robot path and reduce the impact of springs located in the joints.

4.6 Concluding Remarks

We considered the selection of the parameters of the locomotion algorithm for an acceptable stable robot movement using a heuristic approach, data from angular encoders and data tracking the robot movement along a specified path using the **Mocap**. Based on the obtained results, we chose parabolas as a trajectory for the leg motion and robot inclination, and curtate cycloid as **CoR** path during the **CoM** transfer. For this goal we described the dynamic model of the landing platform and performed simulation of the robot motion. The experimental results confirmed that landing gear could move along the straight line with 0.98 cm the standard deviations

of length in each step and standard deviation in yaw of 9 degrees.

The developed landing platform capable of landing and walking is the demonstration of the possibilities of the robot equipped with multifunctional robotic limbs. As part of future improvements, it is necessary to create a full mathematical model of the robot taking into account the influence of springs in the joints and apply the reinforcement learning algorithms for more effective optimization of the CoR trajectory parameters and landing algorithm. For this goal, we already have a full 3D-model of the robot, motion equations and set of built-in sensors.

The problem of compliance and elasticity of the leg joints due to construction of servomotors can be solved using a disturbance observer and the linear quadratic regulator as it was proposed by [Kim et al. \[2018\]](#). The legs of the robot presented in this article are driven by Dynamixel PRO servomotors, which are more powerful than Dynamixel MX106 servomotors in the hip joints of DroneGear. Researchers designed the estimator based on disturbance observer to enhance compliance capability by actuating joints in the direction of the estimated disturbance. Also, they used an LQR-based controller with a flexible joint model to suppress the vibration caused by joint elasticity.

Another way to damp the oscillations that occur during the movement of the robotic limb is to replace the servomotors with force controlled actuators. Such motors provide to control the torque and quickly react to the dynamic loads caused by inertial forces. This type of actuators are used in many modern legged robots (e.g., Cheetah [[Bledt et al., 2018](#)], ANYmal [[Hutter et al., 2016](#)], and ALPHRED [[Hooks et al., 2020](#)]). However, the force controlled actuators have large dimensions, which means more weight. The smallest robot weight of the above is 17.9 kg (ALPHRED), which is more than 3 times the weight of the DroneGear robot (5.67 kg). Thus, it would be necessary to replace the propulsion system and, accordingly, the dimensions of the robot would increase. This statement is also true for the design of the AeroVR robot arm, which is confirmed by the use of compact servomotors in such a large project as ARCAS and AEROARMS [[Ollero and Siciliano, 2019](#)].

Chapter 5

Conclusion

5.1 Research Outcomes

In the framework of this thesis we developed the two prototypes of robots for the operation in the cluttered environment. This group of robots consists of AeroVR and DroneGear robots. The first robot is designed to carry out aerial manipulation with objects in a remote environment under VR-based teleoperation control with the usage of a comfortable wearable interface. The second robot is equipped with a multifunctional landing platform to perform a combined method of the robot movement in the space that can be used for various purposes without additional energy costs. As a result, conducted developments are the response to the main research question:

"How to improve the functional efficiency and control method of the unmanned aerial vehicles equipped with robotic limbs?"

To answer this research question we extended the functional abilities of the usual landing platforms with four legs by developing LocoGear algorithm without mechanical improvements (e.g., increasing the number of DoF of the legs). This solution provides the possibility to move on the terrain without increasing the weight of the flying robot. The locomotion process is less energy-consuming compared to flight. This advantage increases the time of the robot's autonomy. The control algorithms

for both robots were designed, simulated, and tested. Two robotic systems assembled of a multi-rotor aircraft equipped with robotic limbs have been considered. The kinematic models of robots were calculated using methods of forward and inverse kinematics. The dynamic model of the AeroVR robot was designed in Simulink, the dynamic model of DroneGear robot was calculated in Maple and MATLAB. The GUIs were developed for visualization of the robot movement in order to adjust the parameters of the control algorithms in various operating points and estimation of the dynamic loads at these points. Finally, the performance of both robots was tested in laboratory conditions with a ground-truth VICON Mocap.

To provide comfortable control of the robot during aerial manipulation in a remote environment, we proposed a VR-based teleoperation algorithm. The position-position control was used for manipulator control by a wearable interface of the operator. To control the robot flight by VR controller we applied the position-velocity control. Also, a special VR application was designed for comfortable human-robot interaction. The proposed teleoperation strategy allows the operator to intuitively control a flying robot and process of aerial manipulation in a virtual environment supplemented by a real-time video stream from the robot. This control method can be used to control the DroneGear robot. For this purpose, we can also use the VR controller with the position-velocity control. New commands can be assigned, for example, to the side buttons of the controller. Also, using the VR-based teleoperation system, it is possible to implement control a group of robots by providing commands for switching between robots in the VR application.

The first supporting research question was formulated as follows:

"How can the operator remotely control the aerial manipulator in comfortable way?"

To answer this question and propose a solution to this research task, we designed a VR-based teleoperation system to control a flying robot for aerial manipulation in a remote environment. Several designed wearable interfaces were tested. These are the combination of HTC VIVE trackers and designed glove, the usage of several flexible sensors and IMU sensor, and IMU-based interface. All of these sensor

systems were used to collect data about the orientation of the operator's hand. A series of experiments showed that IMUs-based interface with Madgwick filter for manipulator control could be analog to the HTC VIVE trackers. UAV control was performed using HTC VIVE joystick. For a better perception of the current robot state and the surrounding environment, a digital twin of the robot and video from the camera located on the manipulator gripper are projected into HMD in real-time. Essential aspects of the developed method are the simplicity of usage of the wearable interface and the time of operator training in controlling the robot. According to ANOVA statistical analysis of the first user study IMU-based interface is a more natural control device ($F(1, 28) = 5.04$, $p = 0.03 < 0.05$) and allows the operator to perform remote manipulation faster by 27% ($F(1, 22) = 6.8$, $p = 0.016 < 0.05$) with better matching of the manipulator position to the target set-point. Also, the participants appreciated the convenience of the robot's flight control. The developed system demonstrated a robust data transmission to the Unity application. The flight tests of the developed robot showed a stable UAV behavior while grasping of the target object. The average deviations in pitch and roll directions were 2.03 and 0.83 degrees, respectively. The proposed system can considerably improve the quality of aerial manipulations and accelerate the exploitation of this technology in real life.

The second supporting research question was as follows:

"How can the UAV equipped with landing gear walk without structure improvements?"

DroneGear is the first prototype of the flying robot capable to fly, land on an uneven surface, and walk on the ground to the desired position. For this purpose, we performed the theoretical and experimental analysis of a novel locomotion strategy LocoGear developed for the multicopter landing gear with four 2-DoF robotic legs equipped by embedded torque sensors at knee joints. The robot was adjusted via a developed GUI in MATLAB, which sends control commands to Arduino Due using Bluetooth connection.

Using a heuristic approach, we selected the parameters of the locomotion algorithm for an acceptable stable robot movement using data from angle encoders and

tracking the robot movement along a specified path using the *Mocap*. Based on the obtained results, we chose parabolas as a trajectory for the legs motion and robot inclination, and curtate cycloid as *CoR* path during the *CoM* transfer. We estimated the servomotor torques during *Motion cycle* using Lagrangian dynamic formulation and kinetostatic methods.

The results of the experiments confirmed that landing gear could stably move along the line with 0.98 cm the standard deviations of length in each step and standard deviation in yaw at 9 deg. This robot was tested in laboratory conditions during walking on a flat surface and when the robot goes down from the 35-mm height step after landing. The proposed *UAV* equipped with self-moving landing platforms can considerably improve the effectiveness of rescue operations and make exploration of hard to reach places possible.

Some limitations of the proposed approaches appeared at the validation experiments. The study of high speed aerial manipulation and robot motion is not yet conducted. The movements of the robotic limbs were performed at a low speed (up to 0.6 rad/sec) to cancel sudden movements of the robot, which can potentially lead to unstable behavior. The stability of the robot's functioning has been confirmed empirically. The robot did not crash even if the robotic arm was quickly moved from the lower position to the extended position. However, the robot can interact with objects no more than 0.2 kg in extended manipulator position due to increased dynamic load on the *UAV*'s propulsion system. The teleoperation performance can be limited by inaccurate sensors information, operation of the devices with a low battery level, or communication delays. In the case of robot locomotion and landing, it is necessary to design and assemble a robot prototype at an industrial level with the precision mechanics to eliminate the influence of the backlash of the servomotor gears and inaccurate data collection from sensors. Also, the performance of the landing platform can be improved by replacing Arduino microcontroller on the more powerful ones, such as STM32.

The specific theoretical contribution of this thesis provided in the topics of robot design (in the particular design of the lightweight robotic arms), aerial manipulation, locomotion algorithms, design of wearable devices, and teleoperation methods.

5.2 Future Outlook

This section outlines three future research and commercialization opportunities (see Fig. 5-1), with each forming a significant modification in the functionality of the developed robots:

1. The study of group behavior of the robots for search and rescue operations with using the vehicle as a carrier of a group of robots.
2. Development of a multi-functional hybrid robot capable of landing, walking and manipulating objects.
3. The usage flying robots with autonomous mobile platform for the detection of plant diseases and subsequent sampling in the gardens of fruit trees, parks, and forestry.

The first potential research includes the usage of two or more robots, which can be used with the mobile carrier as a transportation and charging station. DroneGear robot can be capable of land in an unstructured environment. After that, this robot should find a way to the target area and move there on an uneven surface. When the robot finds something strange, the robot will send geolocation data and information about the area of interest to the second AeroVR robot. For example, it can be a puddle with a strange fluid or injured person. The second robot equipped by the robotic arm will arrive at the specified coordinates and carried out sampling or deliver the aid kit accordingly.

In the case of developing a hybrid robot, it is necessary to design limbs equipped with multi-functional grips/paws. IMU, torque sensors, resistive force sensors, optical sensors, and cameras can be used to collect data about the operation of the manipulators and the robot as a whole. The robot control system must adapt to the conditions of the landing place, so it makes sense to apply a reinforcement learning algorithm. To carry out a large number of environmental simulations and teach the model to correctly land on various surfaces, it is necessary to develop a mathematical model of the robot, which can be done in the Simulink or Gazebo software packages. Hybrid robots are a new potential area of technological research. For example, cur-

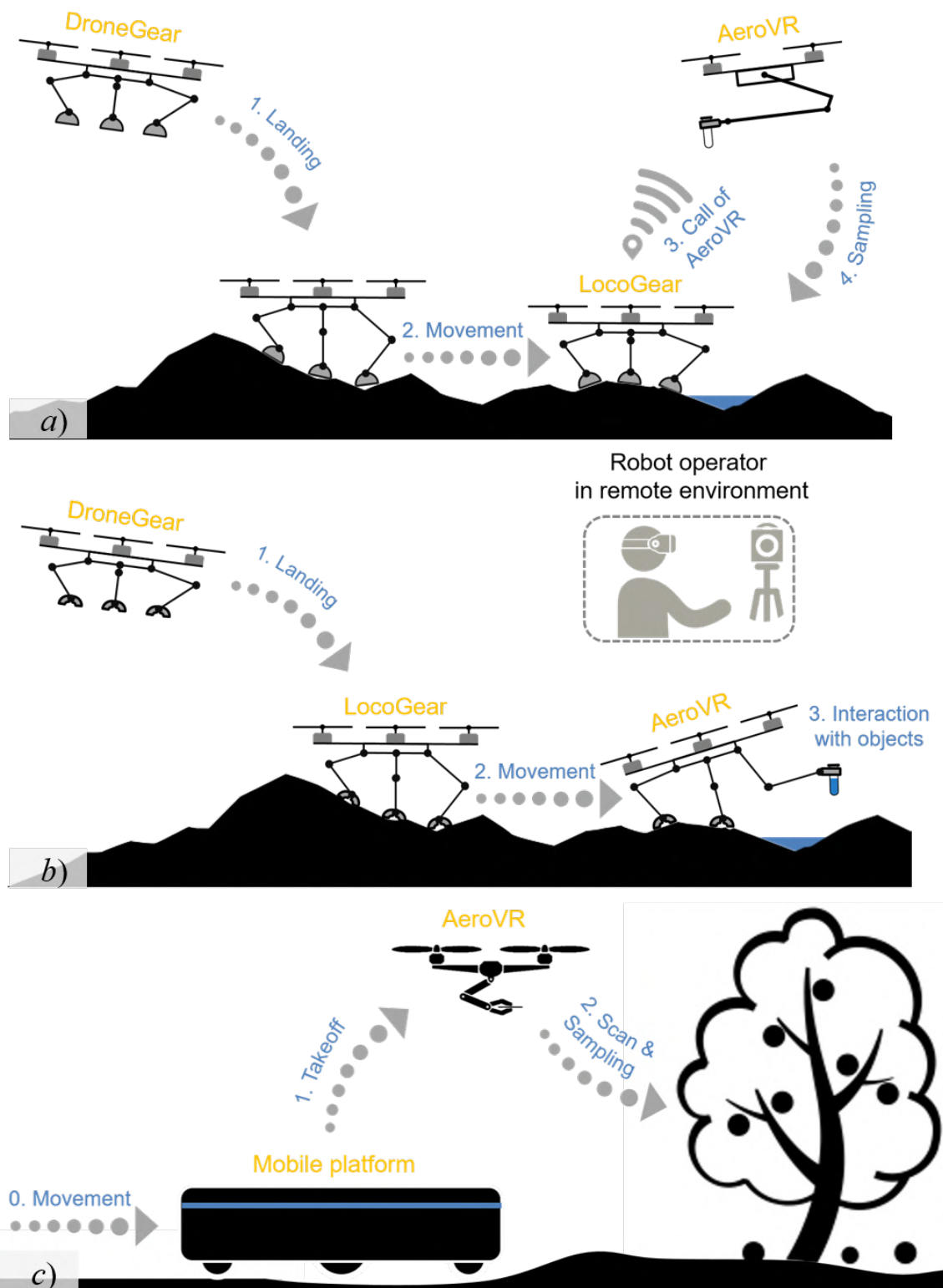


Figure 5-1: Group behavior of the robots for search and rescue operations (a), usage of the multi-functional hybrid robot (b), the detection of plant diseases and sampling using the flying robot with robotic limbs (c).

rently there is exist a European project GRIFFIN¹ on the development robot, which will be able to fly minimizing energy consumption, to perch on curved surfaces, and to perform dexterous manipulation. If we generalize the characteristics that a hybrid robot should have, then, using only onboard equipment and algorithms based on pre-trained models, the hybrid robot must search for the optimal surface on an unknown terrain for a correct landing with the possibility of subsequent take-off and the continuation of the necessary operations for air manipulation.

The third research interest was inspired by two projects performed in our laboratory. The first project was dedicated to the autonomous inventory of warehouses using a group of robots consists of the mobile platform and quadrotor [Kalinov et al., 2019, Kalinov et al., 2020]. The second project narrates about the detection of apple tree diseases in hyperspectral NIR and MIR areas [Shadrin et al., 2020]. These technologies can be combined as follows: the mobile platform is the carrier and charging station for the group of the flying robots with robotic limbs; each UAV is positioned respectively to this platform; also the flying robots are additionally equipped with a multispectral camera; thus this robot will be able to scan trees in the garden and to perform sampling of the leaf or fruit via one or several manipulators.

To implement any of the above projects, we can highlight several key technologies in the field of machine learning, sensors, and mechatronics. Firstly there is necessary to apply reinforcement learning algorithms to achieve safe interaction with the surrounding environment. It can be based on mathematical modeling of the robots and on visual and sensor fusion data analysis for each of the three scenarios. Secondly, to achieve the reliability of the robots, the long continuous autonomy functioning, and maximum payload, it is necessary to perform optimization of the whole robot construction, including the body, legs, actuators, and provide installation of the spring-damper elements in movable joints. In the third stage, since it is necessary to analyze the environment continuously for all three cases, it may be required to use advanced computer vision algorithms for orientation in an unstructured environment. Finally, the group behavior of robots is one more important task for ensuring effective functioning in the proposed scenarios. To reach the maximum efficiency of

¹GRIFFIN, available: <https://griffin-erc-advanced-grant.eu/> (Retrieved June 15, 2020)

wireless data exchange between all devices, it is necessary to conduct studies using various communication methods in addition to Bluetooth.

Appendix A

Electrical Circuit of IMU-based Wearable Interface

The electrical circuit of the IMU-based interface is shown in Fig. A-1. A wearable interface consists of microcontroller Arduino Nano, three IMU sensors GY-91, two flex bending sensors, five coin vibration motors, 7.5V Li-Po battery, and Bluetooth

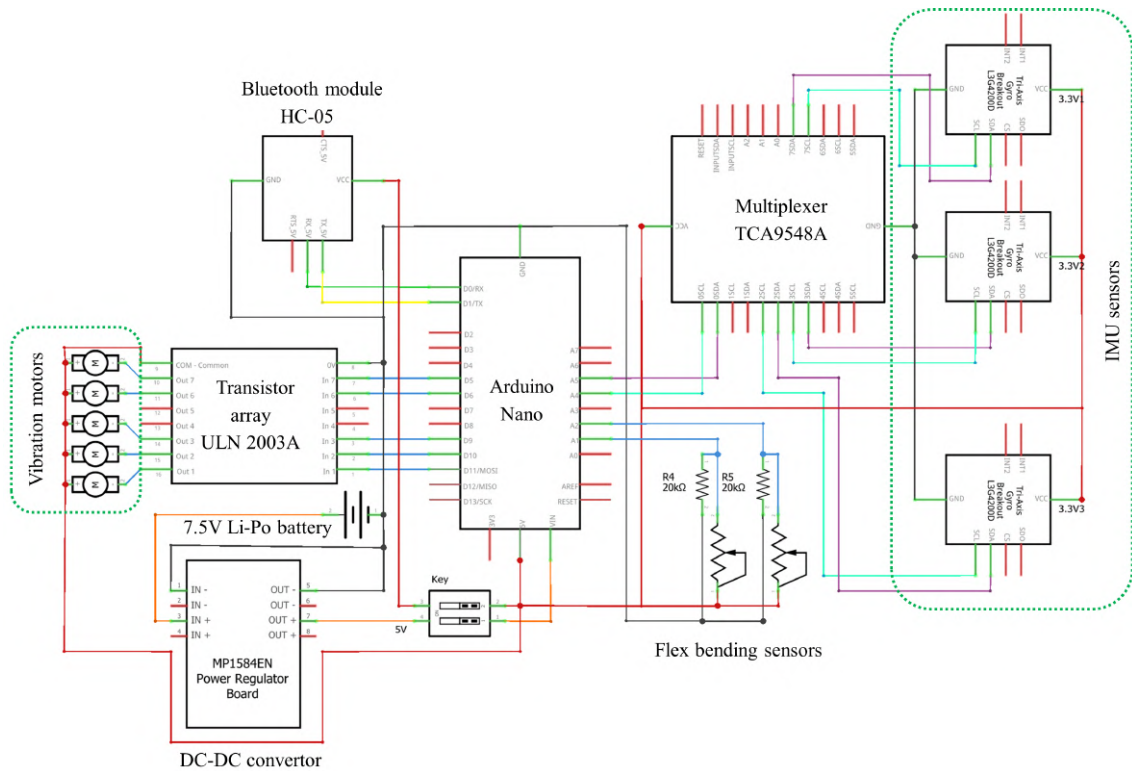


Figure A-1: The electrical circuit of the IMU-based interface.

module HC-05. The data exchange with IMU sensors GY-91 is carried out using the I2C protocol via multiplexer TCA95448A. The flex sensors are connected to the controller using 20 k Ω resistors. The vibration motors are connected to the PWM digital contacts of Arduino via transistor array ULN 2003A. The power supply of the interface from the battery is carried out using a compact MP1584EN DC-DC converter.

Appendix B

Electrical Circuit of DroneGear

In Fig. B-1 the electrical circuit of DroneGear is shown. Control of the Dynamixel servomotors is carried out by Arduino Due via buffer chip 74LS241. The

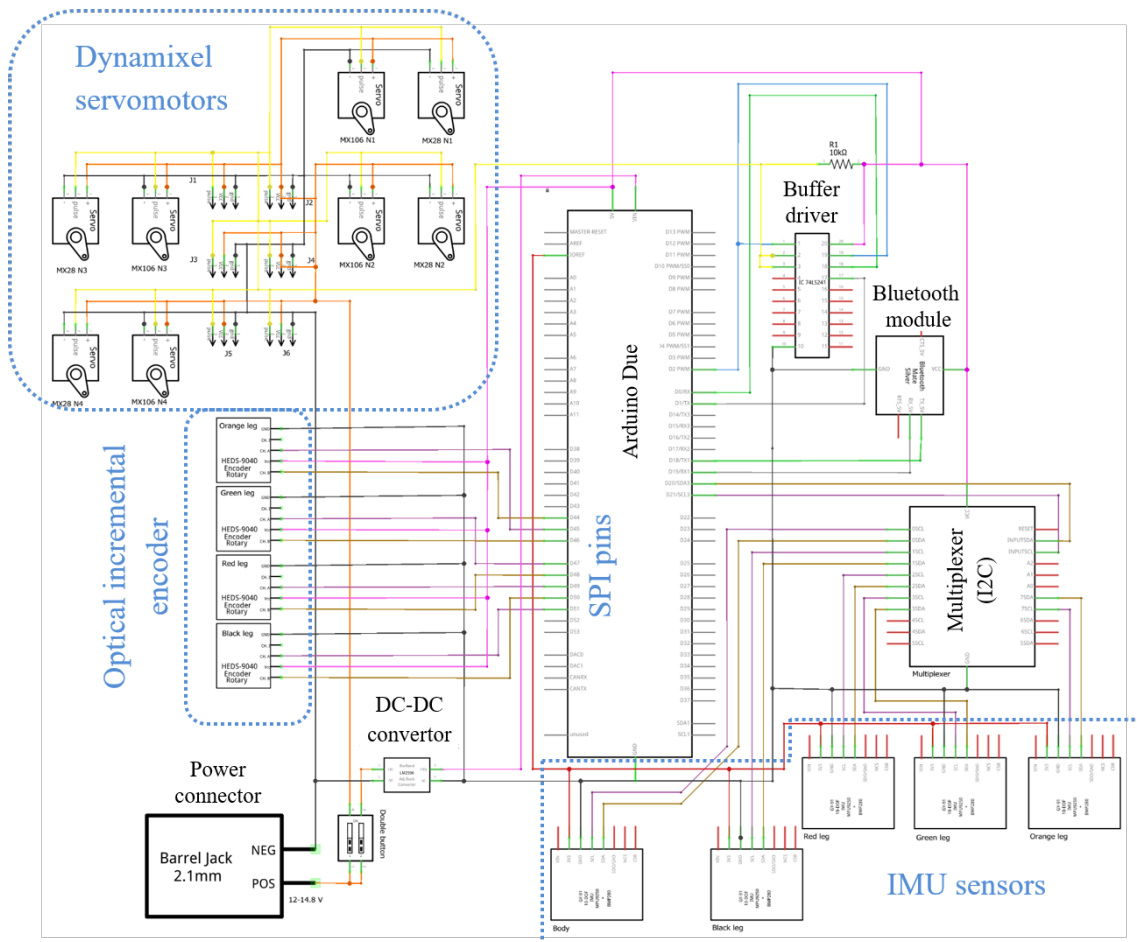


Figure B-1: The electrical circuit of DroneGear.

data exchange with IMU sensors GY-91 embedded in the footpads is carried out using I2C protocol via multiplexer TCA95448A. The data exchange with optical encoders embedded in the knee joints is carried out using the SPI protocol. As wireless communication, we used Bluetooth module HC-05. The electric circuit contains two lines with voltage 12 and 5 volts to power the servomotors and the microcontroller respectively. The microcontroller serves as an energy source for the sensors and the Bluetooth module.

Appendix C

Potential and Kinetic Energies of Landing Platform

The full potential energy of the robot has the following equation:

$$U = 2 \cdot U_{si} + U_l + U_s + U_b, \quad (\text{C.1})$$

where U_{si} , U_l , U_s , and U_b are the potential energies of side, lead, support legs, and body respectively. Full potential energy of the body:

$$U_b = m_b \cdot g \cdot z. \quad (\text{C.2})$$

Potential energy of the side leg:

$$\begin{aligned} U_{si} = & (m_2 \cdot g \cdot (z - l_1 \cdot \sin(\theta_{si}) - l_{2c} \cdot \sin(180 - \beta_{si} - \theta_{si})) \\ & + m_f \cdot g \cdot (z - l_1 \cdot \sin(\theta_{si}) - l_2 \cdot \sin \varepsilon_{si} - l_{fc} \cdot (\sin(180 - \beta_{si} - \theta_{si}))^{H_{si}})) \\ & + m_1 \cdot g \cdot (z - l_{1c} \cdot \sin(\theta_{si})) \cdot \cos(\psi). \end{aligned} \quad (\text{C.3})$$

Potential energy of the lead leg:

$$\begin{aligned}
 U_l = m_2 \cdot g \cdot & \left(z + \frac{l_b}{2} \cdot \sin \psi - l_1 \cdot \sin (\theta_l - \psi) \right. \\
 -l_{2c} \cdot \sin (180 - \beta_l - (\theta_l - \psi)) & \left. \right) + m_f \cdot g \cdot \left(z + \frac{l_b}{2} \cdot \sin \psi - l_1 \cdot \sin (\theta_l - \psi) \right. \\
 -l_2 \cdot \sin (180 - \beta_l - (\theta_l - \psi)) & - l_{fc} \cdot (\sin (180 - \beta_l - (\theta_l - \psi)))^{H_l} \\
 +m_1 \cdot g \cdot & \left. \left(z + \frac{l_b}{2} \cdot \sin \psi - l_{1c} \cdot \sin (\theta_l - \psi) \right) \right). \tag{C.4}
 \end{aligned}$$

Potential energy of the support leg:

$$\begin{aligned}
 U_s = m_2 \cdot g \cdot & \left(z - \frac{l_b}{2} \cdot \sin \psi - l_1 \cdot \sin (\theta_s + \psi) \right. \\
 -l_{2c} \cdot \sin (180 - \beta_s - (\theta_s + \psi)) & \left. \right) + m_f \cdot g \cdot \left(z - \frac{l_b}{2} \cdot \sin \psi - l_1 \cdot \sin (\theta_s + \psi) \right. \\
 -l_2 \cdot \sin (180 - \beta_s - (\theta_s + \psi)) & - l_{fc} \cdot (\sin (180 - \beta_s - (\theta_s + \psi)))^{H_s} \\
 +m_1 \cdot g \cdot & \left. \left(z - \frac{l_b}{2} \cdot \sin \psi - l_{1c} \cdot \sin (\theta_s + \psi) \right) \right). \tag{C.5}
 \end{aligned}$$

In these equations and later H_i is the variable of the leg state (State variable), which takes the value 0 or 1 if the leg is on the ground or raised respectively. Since the movement of the right and left legs are the same, we write equations for one side leg. For convenience, we will consider the movement of the robot in the positive direction of the X -axis (in the plane XZ), since the movement of the robot in the direction of the Y -axis has the same form. To find the kinetic energy, we write the equations for the velocities of all robot parts. The projections of the speed of link 1 of the side leg:

$$V_{1six} = \dot{x} - l_{1\bar{n}} \cdot \sin (\theta_{si}) \cdot \cos (\psi) \cdot \dot{\psi} - l_{1\bar{n}} \cdot \cos (\theta_{si}) \cdot \dot{\theta}_{si} \cdot \sin (\psi), \tag{C.6}$$

$$V_{1siy} = \pm \left(-l_{1\bar{n}} \cdot \sin (\theta_{si}) \cdot \dot{\theta}_{si} \right), \tag{C.7}$$

$$V_{1siz} = \dot{z} + l_{1\bar{n}} \cdot \sin(\theta_{si}) \cdot \sin(\psi) \cdot \dot{\psi} - l_{1\bar{n}} \cdot \cos(\theta_{si}) \cdot \dot{\theta}_{si} \cdot \cos(\psi). \quad (\text{C.8})$$

The projections of the speed of link 2 of the side leg:

$$\begin{aligned} V_{2siox} = & \dot{x} - (l_1 \cdot \sin(\theta_{si}) \\ & - l_{2c} \cdot \sin(\theta_{si} + \beta_{si})) \cdot \cos(\psi) \cdot \dot{\psi} - (l_1 \cdot \cos(\theta_{si}) \cdot \dot{\theta}_{si} \\ & - l_{2c} \cdot \cos(\theta_{si} + \beta_{si}) \cdot (\dot{\theta}_{si} + \dot{\beta}_{si})) \cdot \sin(\psi), \end{aligned} \quad (\text{C.9})$$

$$V_{2siy} = \pm \left(-l_1 \cdot \sin(\theta_{si}) \cdot \dot{\theta}_{si} + l_{2c} \cdot \sin(\theta_{si} + \beta_{si}) \cdot (\dot{\theta}_{si} + \dot{\beta}_{si}) \right), \quad (\text{C.10})$$

$$\begin{aligned} V_{2siz} = & \dot{z} + (l_1 \cdot \sin(\theta_{si}) + l_{2c} \cdot \sin(\theta_{si} + \beta_{si})) \cdot \sin(\psi) \cdot \dot{\psi} \\ & - \left(l_1 \cdot \cos(\theta_{si}) \cdot \dot{\theta}_{si} + l_{2c} \cdot \cos(\theta_{si} + \beta_{si}) \cdot (\dot{\theta}_{si} + \dot{\beta}_{si}) \right) \cdot \cos(\psi). \end{aligned} \quad (\text{C.11})$$

The projections of the speed of link 1 of the lead leg:

$$V_{1lx} = \dot{x} - \frac{l_b}{2} \cdot \sin(\psi) \cdot \dot{\psi} - l_{1c} \cdot \sin(\theta_l - \psi) \cdot (\dot{\theta}_l - \dot{\psi}), \quad (\text{C.12})$$

$$V_{1lz} = \dot{z} + \frac{l_b}{2} \cdot \cos(\psi) \cdot \dot{\psi} - l_{1c} \cdot \cos(\theta_l - \psi) \cdot (\dot{\theta}_l - \dot{\psi}). \quad (\text{C.13})$$

The projections of the speed of link 2 of the lead leg:

$$\begin{aligned} V_{2lix} = & \dot{x} - \frac{l_b}{2} \cdot \sin(\psi) \cdot \dot{\psi} - l_1 \cdot \sin(\theta_l - \psi) \cdot (\dot{\theta}_l - \dot{\psi}) \\ & + l_{2c} \cdot \sin(\beta_l + \theta_l - \psi) \cdot (\dot{\beta}_l + \dot{\theta}_l - \dot{\psi}), \end{aligned} \quad (\text{C.14})$$

$$\begin{aligned} V_{2liz} = & \dot{z} + \frac{l_b}{2} \cdot \cos(\psi) \cdot \dot{\psi} - l_1 \cdot \cos(\theta_l - \psi) \cdot (\dot{\theta}_l - \dot{\psi}) \\ & - l_{2c} \cdot \cos(\beta_l + \theta_l - \psi) \cdot (\dot{\beta}_l + \dot{\theta}_l - \dot{\psi}). \end{aligned} \quad (\text{C.15})$$

The projections of the speed of link 1 of the support leg:

$$V_{1sx} = \dot{x} + \frac{l_b}{2} \cdot \sin(\psi) \cdot \dot{\psi} + l_{1c} \cdot \sin(\theta_s + \psi) \cdot (\dot{\theta}_s + \dot{\psi}), \quad (\text{C.16})$$

$$V_{1sz} = \dot{z} - \frac{l_b}{2} \cdot \cos(\psi) \cdot \dot{\psi} - l_{1c} \cdot \cos(\theta_s + \psi) \cdot (\dot{\theta}_s + \dot{\psi}). \quad (\text{C.17})$$

The projections of the speed of link 2 of the support leg:

$$\begin{aligned} V_{2sx} = \dot{x} + \frac{l_b}{2} \cdot \sin(\psi) \cdot \dot{\psi} + l_1 \cdot \sin(\theta_s + \psi) \cdot (\dot{\theta}_s + \dot{\psi}) \\ + l_{2c} \cdot \sin(\beta_s + \theta_s + \psi) \cdot (\dot{\beta}_s + \dot{\theta}_s + \dot{\psi}), \end{aligned} \quad (\text{C.18})$$

$$\begin{aligned} V_{2sz} = \dot{z} - \frac{l_b}{2} \cdot \cos(\psi) \cdot \dot{\psi} - l_1 \cdot \cos(\theta_s + \psi) \cdot (\dot{\theta}_s + \dot{\psi}) \\ - l_{2c} \cdot \cos(\beta_s + \theta_s + \psi) \cdot (\dot{\beta}_s + \dot{\theta}_s + \dot{\psi}). \end{aligned} \quad (\text{C.19})$$

The movement of the side legs is performed along three axes, while the movement of the leading and supporting legs is performed in the plane XZ , since we will consider the case of the movement of the robot without deviations to the side (in Y -direction) for a general assessment of dynamic loads. We use stiff springs in spherical joints; thus, we can ignore the tilt of the pad due to gravity. Then the square of the speed of the footpads (V_{fi}) can be determined by the replacement l_{2c} by $(l_2 + l_{fc})$ in the expression for the velocity of link 2 (V_{2i}) (C.9-C.11, C.14, C.15, C.18, C.19). The full kinetic energy of the robot has the following equation:

$$K = 2 \cdot K_{si} + K_l + K_s + K_b. \quad (\text{C.20})$$

Kinetic energy of the body:

$$K_b = \frac{m_b \cdot (\dot{x}^2 + \dot{z}^2)}{2} + \frac{J_b \cdot \dot{\psi}^2}{2}. \quad (\text{C.21})$$

Kinetic energy of the lead leg:

$$\begin{aligned}
 K_l = & \left(\frac{m_1 \cdot V_{2l}^2}{2} + \frac{m_f \cdot V_{fl}^2}{2} \right. \\
 & \left. + \frac{(J_f + m_f \cdot (l_2 + l_{fc})) \cdot (\dot{\theta}_l + \dot{\beta}_l - \dot{\psi})^2}{2} \right) \cdot H_l \\
 & + \frac{m_2 \cdot V_{1l}^2}{2} + \frac{J_1 \cdot (\dot{\theta}_l - \dot{\psi})^2}{2} + \frac{J_2 \cdot (\dot{\theta}_l + \dot{\beta}_l - \dot{\psi})^2}{2}.
 \end{aligned} \tag{C.22}$$

Kinetic energy of the support leg:

$$\begin{aligned}
 K_s = & \left(\frac{m_1 \cdot V_{2s}^2}{2} + \frac{m_f \cdot V_{fs}^2}{2} \right. \\
 & \left. + \frac{(J_f + m_f \cdot (l_2 + l_{fc})) \cdot (\dot{\theta}_s + \dot{\beta}_s + \dot{\psi})^2}{2} \right) \cdot H_s \\
 & + \frac{m_2 \cdot V_{1s}^2}{2} + \frac{J_1 \cdot (\dot{\theta}_s + \dot{\psi})^2}{2} + \frac{J_2 \cdot (\dot{\theta}_s + \dot{\beta}_s + \dot{\psi})^2}{2}.
 \end{aligned} \tag{C.23}$$

Using the Huygens-Steiner theorem to calculate the inertia moments for side legs, we write the equations for kinetic energies of the side leg:

$$\begin{aligned}
 K_{si} = & \frac{m_2 \cdot V_{1si}^2}{2} + \frac{J_1 \cdot \theta_{si}^2}{2} + \frac{J_2 \cdot (\dot{\theta}_{si} + \dot{\beta}_{si})^2}{2} + H_{si} \cdot \left(\frac{m_1 \cdot V_{2si}^2}{2} + \frac{m_f \cdot V_{fsi}^2}{2} \right. \\
 & + 0.5 \cdot (J_f + m_f \cdot (l_2 + l_{fc})) \cdot (\dot{\theta}_{si} + \dot{\beta}_{si})^2 + \left(J_{fx} \cdot \sin^2 \left(\theta_{si} + \beta_{si} - \frac{\pi}{2} \right) \right. \\
 & \left. \left. + m_f \cdot (l_1 \cdot \sin \theta_{si} + (l_2 + l_{f\bar{n}}) \cdot \sin(\theta_{si} + \beta_{si}))^2 \right) \cdot \dot{\psi}^2 \cdot 0.5 \right. \\
 & \left. + \dot{\psi}^2 \cdot 0.5 \cdot H_{si} \cdot \left(J_{fx} \cdot \sin^2 \left(\theta_{si} + \beta_{si} - \frac{\pi}{2} \right) \right. \right. \\
 & \left. \left. + m_f \cdot (l_1 \cdot \sin \theta_{si} + (l_2 + l_{f\bar{n}}) \cdot \sin(\theta_{si} + \beta_{si}))^2 \right) + \left(J_{1x} \cdot \sin^2 \left(\frac{\pi}{2} - \theta_{si} \right) \right. \right. \\
 & \left. \left. + m_1 \cdot \left((1 - H_{si}) \cdot l_2 \cdot \sin(\theta_{si} + \beta_{si}) + \left((1 - H_{si}) \cdot l_1 + (-1)^{(1-H_{si})} \cdot l_{1\bar{n}} \right) \cdot \sin \theta_{si} \right)^2 \right) \right. \\
 & \left. \cdot \dot{\psi}^2 \cdot 0.5 + 0.5 \cdot \left(J_{2x} \cdot \sin^2 \left(\theta_{si} + \beta_{si} - \frac{\pi}{2} \right) \right. \right. \\
 & \left. \left. + m_2 \cdot \left(H_{si} \cdot l_1 \cdot \sin \theta_{si} + \left((1 - H_{si}) \cdot l_2 + (-1)^{(1-H_{si})} \cdot l_{2\bar{n}} \right) \cdot \sin(\theta_{si} + \beta_{si}) \right)^2 \right) \right) \cdot \dot{\psi}^2.
 \end{aligned} \tag{C.24}$$

In (C.21-C.24) J_b , J_1 , J_2 , J_f are inertia moments of the body, link 1, link 2 and the footpad around an axis passing through their CoMs and parallel to the Y -axis; J_{1x} , J_{2x} , J_{fx} are inertia moments of the link 1, link 2 and the footpad around an axis passing through their CoMs and parallel to the X -axis. In (C.21-C.24) some parts of kinetic energies are multiplied by state variable H_i , because the movement of the second links can be rotational or compound, and the footpads can be in quiescence or carry out compound movement for the contact with the ground or legs in the air respectively.

Bibliography

- [1] Amazon. Amazon Prime Air, 2016. URL <https://www.amazon.com/Amazon-Prime-Air/b?ie=UTF8&node=8037720011/>.
- [2] Víctor Hugo Andaluz, Washington X Quevedo, Fernando A Chicaiza, José Varela, Cristian Gallardo, Jorge S Sánchez, and Oscar Arteaga. Transparency of a bilateral tele-operation scheme of a mobile manipulator robot. In *International Conference on Augmented Reality, Virtual Reality and Computer Graphics*, pages 228–245. Springer, 2016. doi:10.1007/978-3-319-40621-3_18.
- [3] Moritz Arns and Dan Zhang. Novel reconfigurable delta robot dual-functioning as adaptive landing gear and manipulator. 2019. URL <https://yorkspace.library.yorku.ca/xmlui/handle/10315/36342>.
- [4] Samuel Baker, Dean Soccol, Adam Postula, and Mandyam V Srinivasan. Passive landing gear using coupled mechanical design. In *Proc. Australas. Conf. Robot. Autom.*, pages 1–8, 2013. URL <http://www.araa.asn.au/acra/acra2013/papers/pap175s1-file1.pdf>.
- [5] Carmine Dario Bellicoso, Luca Rosario Buonocore, Vincenzo Lippiello, and Bruno Siciliano. Design, modeling and control of a 5-dof light-weight robot arm for aerial manipulation. In *2015 23rd Mediterranean Conference on Control and Automation (MED)*, pages 853–858. IEEE, 2015. doi:10.1109/MED.2015.7158852.
- [6] Markus Bernard, Konstantin Kondak, Ivan Maza, and Anibal Ollero. Autonomous transportation and deployment with aerial robots for search and rescue missions. *Journal of Field Robotics*, 28(6):914–931, 2011. doi:10.1002/rob.20401.
- [7] Gerardo Bleedt, Matthew J Powell, Benjamin Katz, Jared Di Carlo, Patrick M Wensing, and Sangbae Kim. Mit cheetah 3: Design and control of a robust, dynamic quadruped robot. In *2018 IEEE/RSJ International Conference on Intelligent Robots and Systems (IROS)*, pages 2245–2252. IEEE, 2018. doi:10.1109/IROS.2018.8593885.
- [8] Karen Bodie, Maximilian Brunner, Michael Pantic, Stefan Walser, Patrick Pfändler, Ueli Angst, Roland Siegwart, and Juan Nieto. An omnidirectional aerial manipulation platform for contact-based inspection. *arXiv preprint arXiv:1905.03502*, 2019. doi:10.15607/RSS.2019.XV.019.

- [9] Daniel Melia Boix, Keng Goh, and James McWhinnie. Modelling and control of helicopter robotic landing gear for uneven ground conditions. In *2017 Workshop on Research, Education and Development of Unmanned Aerial Systems (RED-UAS)*, pages 60–65. IEEE, 2017. doi:[10.1109/RED-UAS.2017.8101644](https://doi.org/10.1109/RED-UAS.2017.8101644).
- [10] Adam Przemysław Buczyłowski, Maciej Rećko, Adam Wolniakowski, and Karol Haraburda. A hand-held teleoperation device for the control of the mars rover analogue manipulator. *International Journal of Mechanical Engineering and Robotics Research*, 9(7), 2020. doi:[10.18178/ijmerr.9.7.1018-1023](https://doi.org/10.18178/ijmerr.9.7.1018-1023).
- [11] Stephen Burns. Drone meets delivery truck, 2017. URL <https://www.ups.com/us/es/services/knowledge-center/article.page?kid=cd18bdc2/>.
- [12] R Cano, C Pérez, F Pruano, A Ollero, and G Heredia. Mechanical design of a 6-dof aerial manipulator for assembling bar structures using uavs. 2013.
- [13] Justin Carpentier, Mehdi Benallegue, and Jean-Paul Laumond. On the centre of mass motion in human walking. *International Journal of Automation and Computing*, 14(5):542–551, 2017. doi:[10.1007/s11633-017-1088-5](https://doi.org/10.1007/s11633-017-1088-5).
- [14] Ting Kwok Chan, Ying Kin Yu, Ho Chuen Kam, and Kin Hong Wong. Robust hand gesture input using computer vision, inertial measurement unit (imu) and flex sensors. In *2018 IEEE International Conference on Mechatronics, Robotics and Automation (ICMRA)*, pages 95–99. IEEE, 2018. doi:[10.1109/ICMRA.2018.8490559](https://doi.org/10.1109/ICMRA.2018.8490559).
- [15] Haoyao Chen, Fengyu Quan, Linxu Fang, and Shiwu Zhang. Aerial grasping with a lightweight manipulator based on multi-objective optimization and visual compensation. *Sensors*, 19(19):4253, 2019. doi:[10.3390/s19194253](https://doi.org/10.3390/s19194253).
- [16] Petr Čížek, Jiří Kubík, and Jan Faigl. Online foot-strike detection using inertial measurements for multi-legged walking robots. In *2018 IEEE/RSJ International Conference on Intelligent Robots and Systems (IROS)*, pages 7622–7627. IEEE, 2018. doi:[10.1109/IROS.2018.8594010](https://doi.org/10.1109/IROS.2018.8594010).
- [17] Andre Coelho, Christian Ott, Harsimran Singh, Fernando Lizarralde, and Konstantin Kondak. Multi-dof time domain passivity approach based drift compensation for telemanipulation. In *2019 19th International Conference on Advanced Robotics (ICAR)*, pages 695–701. IEEE, 2019. doi:[10.1109/ICAR46387.2019.8981661](https://doi.org/10.1109/ICAR46387.2019.8981661).
- [18] Andre Coelho, Harsimran Singh, Konstantin Kondak, and Christian Ott. Whole-body bilateral teleoperation of a redundant aerial manipulator. *arXiv preprint arXiv:2001.10779*, 2020. URL <https://arxiv.org/abs/2001.10779>.
- [19] John J Craig. *Introduction to robotics: mechanics and control, 3/E*. Pearson Education India, 2009.

- [20] Todd W Danko and Paul Y Oh. Toward coordinated manipulator-host visual servoing for mobile manipulating uavs. In *2014 IEEE International Conference on Technologies for Practical Robot Applications (TePRA)*, pages 1–6. IEEE, 2014. doi:10.1109/TePRA.2014.6869149.
- [21] Todd W Danko, Kenneth P Chaney, and Paul Y Oh. A parallel manipulator for mobile manipulating uavs. In *2015 IEEE international conference on technologies for practical robot applications (TePRA)*, pages 1–6. IEEE, 2015. doi:10.1109/TePRA.2015.7219682.
- [22] DARPA. Robotic landing gear could enable future helicopters to take off and land almost anywhere, October 2015. URL <https://www.darpa.mil/news-events/2015-09-10>.
- [23] Abdulmotaleb El Saddik. Digital twins: The convergence of multimedia technologies. *IEEE multimedia*, 25(2):87–92, 2018. doi:10.1109/MMUL.2018.023121167.
- [24] Manuel Ferre, Rafael Aracil, and Miguel A Sanchez-Uran. Stereoscopic human interfaces. *IEEE Robotics & Automation Magazine*, 15(4):50–57, 2008. doi:10.1109/MRA.2008.929929.
- [25] A.M. Formalskii. *The movement of anthropomorphic mechanisms*. Publisher "Science", 1982. Rus: A.M. Формальский. Перемещение антропоморфных механизмов. Издательство "Наука".
- [26] Vaibhav Ghadiok, Jeremy Goldin, and Wei Ren. Autonomous indoor aerial gripping using a quadrotor. In *2011 IEEE/RSJ International Conference on Intelligent Robots and Systems*, pages 4645–4651. IEEE, 2011. doi:10.1109/IROS.2011.6094690.
- [27] Maki K Habib. *Humanitarian demining: The problem, difficulties, priorities, demining technology and the challenge for robotics*. Citeseer, 2008.
- [28] Guillermo Heredia, AE Jimenez-Cano, I Sanchez, Domingo Llorente, V Vega, J Braga, JA Acosta, and Aníbal Ollero. Control of a multi-rotor outdoor aerial manipulator. In *2014 IEEE/RSJ International Conference on Intelligent Robots and Systems*, pages 3417–3422. IEEE, 2014. doi:10.1109/IROS.2014.6943038.
- [29] Joshua Hooks and Dennis Hong. Implementation of a versatile 3d zmp trajectory optimization algorithm on a multi-modal legged robotic platform. In *2018 IEEE/RSJ International Conference on Intelligent Robots and Systems (IROS)*, pages 3777–3782. IEEE, 2018. doi:10.1109/IROS.2018.8593968.
- [30] Joshua Hooks, Min Sung Ahn, Jeffrey Yu, Xiaoguang Zhang, Taoyuanmin Zhu, Hosik Chae, and Dennis Hong. Alphred: A multi-modal operations quadruped robot for package delivery applications. *IEEE Robotics and Automation Letters*, 5(4):5409–5416, 2020. doi:10.1109/LRA.2020.3007482.

- [31] Marco Hutter, Christian Gehring, Dominic Jud, Andreas Lauber, C Dario Bellicoso, Vassilios Tsounis, Jemin Hwangbo, Karen Bodie, Peter Fankhauser, Michael Bloesch, et al. Anymal-a highly mobile and dynamic quadrupedal robot. In *2016 IEEE/RSJ International Conference on Intelligent Robots and Systems (IROS)*, pages 38–44. IEEE, 2016. doi:[10.1109/IROS.2016.7758092](https://doi.org/10.1109/IROS.2016.7758092).
- [32] Marco Hutter, Christian Gehring, Andreas Lauber, Fabian Gunther, Carmine Dario Bellicoso, Vassilios Tsounis, Péter Fankhauser, Remo Diethelm, Samuel Bachmann, Michael Blösch, et al. Anymal-toward legged robots for harsh environments. *Advanced Robotics*, 31(17):918–931, 2017. doi:[10.1080/01691864.2017.1378591](https://doi.org/10.1080/01691864.2017.1378591).
- [33] Nursultan Imanberdiyev and Erdal Kayacan. A fast learning control strategy for unmanned aerial manipulators. *Journal of Intelligent & Robotic Systems*, 94(3-4):805–824, 2019. doi:[10.1007/s10846-018-0884-7](https://doi.org/10.1007/s10846-018-0884-7).
- [34] Werner Alexander Isop, Christoph Gebhardt, Tobias Nägeli, Friedrich Fraundorfer, Otmar Hilliges, and Dieter Schmalstieg. High-level teleoperation system for aerial exploration of indoor environments. *Frontiers in Robotics and AI*, 6, 2019. doi:[10.3389/frobt.2019.00095](https://doi.org/10.3389/frobt.2019.00095).
- [35] Inmo Jang, Joaquin Carrasco, Andrew Weightman, and Barry Lennox. Intuitive bare-hand teleoperation of a robotic manipulator using virtual reality and leap motion. In *Annual Conference Towards Autonomous Robotic Systems*, pages 283–294. Springer, 2019. doi:[10.1007/978-3-030-25332-5_25](https://doi.org/10.1007/978-3-030-25332-5_25).
- [36] AE Jimenez-Cano, Jesús Martín, Guillermo Heredia, Aníbal Ollero, and R Cano. Control of an aerial robot with multi-link arm for assembly tasks. In *2013 IEEE International Conference on Robotics and Automation*, pages 4916–4921. IEEE, 2013. doi:[10.1109/ICRA.2013.6631279](https://doi.org/10.1109/ICRA.2013.6631279).
- [37] Arash Kalantari and Matthew Spenko. Design and experimental validation of hytaq, a hybrid terrestrial and aerial quadrotor. In *2013 IEEE International Conference on Robotics and Automation*, pages 4445–4450. IEEE, 2013. doi:[10.1109/ICRA.2013.6631208](https://doi.org/10.1109/ICRA.2013.6631208).
- [38] I. A. Kalinov, R. T. Agishev, A. A. Petrovskiy, E. S. Safronov, T. V. Melnik, M. A. Kurenkov, V. S. Ramzhaev, I. N. Idrisov, G. A. Yashin, and D. O. Tsetserukou. The program for stabilization, localization and navigation of uavs relative to a mobile robot in a warehouse with a gps signal and the presence of a large amount of metal, Certificate of state registration of a computer program: RU 2019661130, April 2019. URL bit.ly/fips-ru-patent-2019661130.
- [39] I. A. Kalinov, G. A. Yashin, A. A. Petrovskiy, and D. O. Tsetserukou. Hybrid robotic platform for warehouse inventory automation, Patent: RU 197 225 U1, April 2020. URL bit.ly/fips-ru-patent-197225.
- [40] Ivan Kalinov, Evgenii Safronov, Ruslan Agishev, Mikhail Kurenkov, and Dzmitry Tsetserukou. High-precision uav localization system for landing on

- a mobile collaborative robot based on an ir marker pattern recognition. In *2019 IEEE 89th Vehicular Technology Conference (VTC2019-Spring)*, pages 1–6. IEEE, 2019. doi:[10.1109/VTCSpring.2019.8746668](https://doi.org/10.1109/VTCSpring.2019.8746668).
- [41] Ali Kanso, Imad H Elhajj, Elie Shamma, and Daniel Asmar. Enhanced teleoperation of uavs with haptic feedback. In *International Conference on Advanced Intelligent Mechatronics*, page 305–310. IEEE, 2015. doi:[10.1109/AIM.2015.7222549](https://doi.org/10.1109/AIM.2015.7222549).
- [42] Mingon Kim, Jung Hoon Kim, Sanghyun Kim, Jaehoon Sim, and Jaeheung Park. Disturbance observer based linear feedback controller for compliant motion of humanoid robot. In *2018 IEEE International Conference on Robotics and Automation (ICRA)*, pages 403–410. IEEE, 2018. doi:[10.1109/ICRA.2018.8460618](https://doi.org/10.1109/ICRA.2018.8460618).
- [43] Suseong Kim, Seungwon Choi, and H Jin Kim. Aerial manipulation using a quadrotor with a two dof robotic arm. In *2013 IEEE/RSJ International Conference on Intelligent Robots and Systems*, pages 4990–4995. IEEE, 2013. doi:[10.1109/IROS.2013.6697077](https://doi.org/10.1109/IROS.2013.6697077).
- [44] Suseong Kim, Hoseong Seo, Seungwon Choi, and H Jin Kim. Vision-guided aerial manipulation using a multicopter with a robotic arm. *IEEE/ASME Transactions On Mechatronics*, 21(4):1912–1923, 2016. doi:[10.1109/TMECH.2016.2523602](https://doi.org/10.1109/TMECH.2016.2523602).
- [45] Suseong Kim, Hoseong Seo, Jongho Shin, and H Jin Kim. Cooperative aerial manipulation using multicopters with multi-dof robotic arms. *IEEE/ASME Transactions on Mechatronics*, 23(2):702–713, 2018. doi:[10.1109/TMECH.2018.2792318](https://doi.org/10.1109/TMECH.2018.2792318).
- [46] Hiroshi Kimura, Isao Shimoyama, and Hirofumi Miura. Dynamics in the dynamic walk of a quadruped robot. *Advanced Robotics*, 4(3):283–301, 1989. doi:[10.1163/156855390X00305](https://doi.org/10.1163/156855390X00305).
- [47] Konstantin Kondak, Felix Huber, Marc Schwarzbach, Maximilian Laiacker, Dominik Sommer, Manuel Bejar, and Anibal Ollero. Aerial manipulation robot composed of an autonomous helicopter and a 7 degrees of freedom industrial manipulator. In *2014 IEEE international conference on robotics and automation (ICRA)*, pages 2107–2112. IEEE, 2014. doi:[10.1109/ICRA.2014.6907148](https://doi.org/10.1109/ICRA.2014.6907148).
- [48] Christopher Korpela, Matko Orsag, Miles Pekala, and Paul Oh. Dynamic stability of a mobile manipulating unmanned aerial vehicle. In *2013 IEEE International Conference on Robotics and Automation*, pages 4922–4927. IEEE, 2013. doi:[10.1109/ICRA.2013.6631280](https://doi.org/10.1109/ICRA.2013.6631280).
- [49] Christopher Korpela, Matko Orsag, Todd Danko, and Paul Oh. Insertion tasks using an aerial manipulator. In *2014 IEEE international conference on technologies for practical robot applications (TePRA)*, pages 1–6. IEEE, 2014. doi:[10.1109/TePRA.2014.6869148](https://doi.org/10.1109/TePRA.2014.6869148).

- [50] Christopher Korpela, Matko Orsag, and Paul Oh. Towards valve turning using a dual-arm aerial manipulator. In *2014 IEEE/RSJ International Conference on Intelligent Robots and Systems*, pages 3411–3416. IEEE, 2014. doi:[10.1109/IROS.2014.6943037](https://doi.org/10.1109/IROS.2014.6943037).
- [51] James Kutia. *Aerial Manipulation for Canopy Sampling*. PhD thesis, ResearchSpace@ Auckland, 2019. URL <http://hdl.handle.net/2292/46941>.
- [52] James R Kutia, Karl A Stol, and Weiliang Xu. Canopy sampling using an aerial manipulator: A preliminary study. In *2015 International Conference on Unmanned Aircraft Systems (ICUAS)*, pages 477–484. IEEE, 2015. doi:[10.1109/ICUAS.2015.7152326](https://doi.org/10.1109/ICUAS.2015.7152326).
- [53] Luiza Labazanova, Akerke Tleugazy, Evgeny Tsykunov, and Dzmitry Tsetserukou. Swarmglove: A wearable tactile device for navigation of swarm of drones in vr environment. In *International AsiaHaptics conference*, pages 304–309. Springer, 2018. doi:[10.1007/978-981-13-3194-7_67](https://doi.org/10.1007/978-981-13-3194-7_67).
- [54] Maximilian Laiacker, Felix Huber, and Konstantin Kondak. High accuracy visual servoing for aerial manipulation using a 7 degrees of freedom industrial manipulator. In *2016 IEEE/RSJ International Conference on Intelligent Robots and Systems (IROS)*, pages 1631–1636. IEEE, 2016. doi:[10.1109/IROS.2016.7759263](https://doi.org/10.1109/IROS.2016.7759263).
- [55] Stella Latscha, Michael Kofron, Anthony Stroffolino, Lauren Davis, Gabrielle Merritt, Matthew Piccoli, and Mark Yim. Design of a hybrid exploration robot for air and land deployment (herald) for urban search and rescue applications. In *2014 IEEE/RSJ International Conference on Intelligent Robots and Systems*, pages 1868–1873. IEEE, 2014. doi:[10.1109/IROS.2014.6942808](https://doi.org/10.1109/IROS.2014.6942808).
- [56] J. Lee. Hierarchical controller for highly dynamic locomotion utilizing pattern modulation and impedance control: implementation on the mit cheetah robot, 2013. URL <https://dspace.mit.edu/handle/1721.1/85490>.
- [57] Jameson Y Lee, Zachary Cook, Alexander Barzilov, and Woosoon Yim. Control of an aerial manipulator with an on-board balancing mechanism. In *ASME 2016 International Mechanical Engineering Congress and Exposition*. American Society of Mechanical Engineers Digital Collection, 2016. doi:[10.1115/IMECE2016-66976](https://doi.org/10.1115/IMECE2016-66976).
- [58] Jongseok Lee, Ribin Balachandran, Yuri S Sarkisov, Marco De Stefano, Andre Coelho, Kashmira Shinde, Min Jun Kim, Rudolph Triebel, and Konstantin Kondak. Visual-inertial telepresence for aerial manipulation. *arXiv preprint arXiv:2003.11509*, 2020. URL <https://arxiv.org/abs/2003.11509>.
- [59] Jongwoo Lee, Dong Jin Hyun, Joeeun Ahn, Sangbae Kim, and Neville Hogan. On the dynamics of a quadruped robot model with impedance control: Self-stabilizing high speed trot-running and period-doubling bifurcations. In *2014 IEEE/RSJ International Conference on Intelligent Robots and Systems*, pages 4907–4913. IEEE, 2014. doi:[10.1109/IROS.2014.6943260](https://doi.org/10.1109/IROS.2014.6943260).

- [60] Boyang Li, Yifan Jiang, Jingxuan Sun, Lingfeng Cai, and Chih-Yung Wen. Development and testing of a two-uav communication relay system. *Sensors*, 16(10):1696, 2016. doi:[10.3390/s16101696](https://doi.org/10.3390/s16101696).
- [61] Zhijun Li, Quanbo Ge, Wenjun Ye, and Peijiang Yuan. Dynamic balance optimization and control of quadruped robot systems with flexible joints. *IEEE Transactions on Systems, Man, and Cybernetics: Systems*, 46(10):1338–1351, 2015. doi:[10.1109/TSMC.2015.2504552](https://doi.org/10.1109/TSMC.2015.2504552).
- [62] Eleftherios Lygouras, Nicholas Santavas, Anastasios Taitzoglou, Konstantinos Tarchanidis, Athanasios Mitropoulos, and Antonios Gasteratos. Unsupervised human detection with an embedded vision system on a fully autonomous uav for search and rescue operations. *Sensors*, 19(16):3542, 2019. doi:[10.3390/s19163542](https://doi.org/10.3390/s19163542).
- [63] Sebastian Madgwick. An efficient orientation filter for inertial and inertial/magnetic sensor arrays. *Report x-io and University of Bristol (UK)*, 25:113–118, 2010.
- [64] Vasudevan Manivannan, Jared P Langley, Mark Costello, and Massimo Ruzzene. Rotorcraft slope landings with articulated landing gear. In *AIAA Atmospheric Flight Mechanics (AFM) Conference*, page 5160, 2013. doi:[10.2514/6.2013-5160](https://doi.org/10.2514/6.2013-5160).
- [65] Nicolas Marchand, Fermi Guerrero-Castellanos, Durand Syl-vain, AE Lopez-Luna, et al. Improving control of quadrotors carrying a manipulator arm. In *XVI Congreso Latinoamericano de Control Automático*, pages 6–p, 2014. URL <https://hal.archives-ouvertes.fr/hal-01067104/>.
- [66] Bernard Markus, Konstantin Kondak, and Gunter Hommel. A slung load transportation system based on small size helicopters. *Spring Science+ Business Media BV*, 2008. doi:[10.1007/978-1-4020-8889-6_6](https://doi.org/10.1007/978-1-4020-8889-6_6).
- [67] L Marques, AT De Almeida, Manuel Armada, Roemi Fernández, Héctor Montes Franceschi, P González, and Y Baudoin. State of the art review on mobile robots and manipulators for humanitarian demining. 2016. URL <http://rida2.utp.ac.pa/handle/123456789/2401>.
- [68] Marcos R. O. A. Maximo, Carlos H.C. Ribeiro, and Rubens J.M. Afonso. Modeling of a position servo used in robotics applications. In *XIII Simpósio Brasileiro de Automação Inteligente*, pages 2032–2038, 2017. URL https://www.ufrgs.br/sbai17/papers/paper_599.pdf.
- [69] Daniel Mellinger, Quentin Lindsey, Michael Shomin, and Vijay Kumar. Design, modeling, estimation and control for aerial grasping and manipulation. In *2011 IEEE/RSJ International Conference on Intelligent Robots and Systems*, pages 2668–2673. IEEE, 2011. doi:[10.1109/IROS.2011.6094871](https://doi.org/10.1109/IROS.2011.6094871).

- [70] Nathan Michael, Shaojie Shen, Kartik Mohta, Yash Mulgaonkar, Vijay Kumar, Keiji Nagatani, Yoshito Okada, Seiga Kiribayashi, Kazuki Otake, Kazuya Yoshida, et al. Collaborative mapping of an earthquake-damaged building via ground and aerial robots. *Journal of Field Robotics*, 29(5):832–841, 2012. doi:[10.1007/978-3-642-40686-7_3](https://doi.org/10.1007/978-3-642-40686-7_3).
- [71] Jenifer Miehlbradt, Alexandre Cherpillod, Stefano Mintchev, Martina Coscia, Fiorenzo Artoni, Dario Floreano, and Silvestro Micera. Data-driven body-machine interface for the accurate control of drones. volume 115, pages 7913–7918. National Acad Sciences, 2018. doi:[10.1073/pnas.1718648115](https://doi.org/10.1073/pnas.1718648115).
- [72] S. MohaimenianPour and R. Vaughan. Hands and faces, fast: Mono-camera user detection robust enough to directly control a uav in flight. In *International Conference on Intelligent Robots and Systems*, page 5224–5231. IEEE/RSJ, 2018. doi:[10.1109/IROS.2018.8593709](https://doi.org/10.1109/IROS.2018.8593709).
- [73] Robin R Murphy and Debra Schreckenghost. Survey of metrics for human-robot interaction. In *2013 8th ACM/IEEE International Conference on Human-Robot Interaction (HRI)*, pages 197–198. IEEE, 2013. doi:[10.1109/HRI.2013.6483569](https://doi.org/10.1109/HRI.2013.6483569).
- [74] Robin R Murphy, Jeffery Kravitz, Samuel L Stover, and Rahmat Shoureshi. Mobile robots in mine rescue and recovery. *IEEE Robotics Automation Magazine*, 16(2):91–103, 2009. doi:[10.1109/MRA.2009.932521](https://doi.org/10.1109/MRA.2009.932521).
- [75] Abdeldjallil Naceri, Dario Mazzanti, Joao Bimbo, Domenico Prattichizzo, Darwin G Caldwell, Leonardo S Mattos, and Nikhil Deshpande. Towards a virtual reality interface for remote robotic teleoperation. In *2019 19th International Conference on Advanced Robotics (ICAR)*, pages 284–289. IEEE, 2019. doi:[10.1109/ICAR46387.2019.8981649](https://doi.org/10.1109/ICAR46387.2019.8981649).
- [76] Arjun Nagendran, William Crowther, and Robert Richardson. Biologically inspired legs for uav perched landing. *IEEE Aerospace and Electronic Systems Magazine*, 27(2):4–13, 2012. doi:[10.1109/MAES.2012.6163608](https://doi.org/10.1109/MAES.2012.6163608).
- [77] J. Nagi, A. Giusti, G.A. Di Caro, and L.M. Gambardella. Hri in the sky: controlling uavs using face poses and hand gestures. In *International conference on Human-robot interaction*, page 252–253. ACM/IEEE, 2014.
- [78] Tayyab Naseer, Jürgen Sturm, and Daniel Cremers. Followme: Person following and gesture recognition with a quadcopter. In *International Conference on Intelligent Robots and Systems*, page 624–630. IEEE/RSJ, 2013. doi:[10.1109/IROS.2013.6696416](https://doi.org/10.1109/IROS.2013.6696416).
- [79] Yoshinori Ohnishi, Takeshi Takaki, Tadayoshi Aoyama, and Idaku Ishii. Development of a 4-joint 3-dof robotic arm with anti-reaction force mechanism for a multicopter. In *2017 IEEE/RSJ International Conference on Intelligent Robots and Systems (IROS)*, pages 985–991. IEEE, 2017. doi:[10.1109/IROS.2017.8202265](https://doi.org/10.1109/IROS.2017.8202265).

- [80] Anibal Ollero and Bruno Siciliano. *Aerial Robotic Manipulation*. Springer Tracts in Advanced Robotics. Springer Cham, 2019. doi:[10.1007/978-3-030-12945-3](https://doi.org/10.1007/978-3-030-12945-3).
- [81] Anibal Ollero, Guillermo Heredia, Antonio Franchi, Gianluca Antonelli, Konstantin Kondak, Alberto Sanfeliu, Antidio Viguria, J Ramiro Martinez-de Dios, Francesco Pierri, Juan Cortés, et al. The aeroarms project: Aerial robots with advanced manipulation capabilities for inspection and maintenance. *IEEE Robotics & Automation Magazine*, 25(4):12–23, 2018. doi:[10.1109/MRA.2018.2852789](https://doi.org/10.1109/MRA.2018.2852789).
- [82] Anibal Ollero, Antidio Viguria, Miguel Angel Trujillo, Moritz Oetiker, and Bernard Revaz. Inspection and maintenance. In *Aerial Robotic Manipulation*, pages 367–379. Springer, 2019. doi:[10.1007/978-3-030-12945-3_26](https://doi.org/10.1007/978-3-030-12945-3_26).
- [83] Matko Orsag, Christopher Korpela, Paul Oh, and Stjepan Bogdan. *Aerial Manipulation*. Advances in Industrial Control. Springer Cham, 2018. doi:[10.1007/978-3-319-61022-1](https://doi.org/10.1007/978-3-319-61022-1).
- [84] Hannibal Paul, Ryo Miyazaki, Robert Ladig, and Kazuhiro Shimonomura. Landing of a multirotor aerial vehicle on an uneven surface using multiple on-board manipulators. In *2019 IEEE/RSJ International Conference on Intelligent Robots and Systems (IROS)*, pages 1926–1933, 2019. doi:[10.1109/IROS40897.2019.8968529](https://doi.org/10.1109/IROS40897.2019.8968529).
- [85] Alberto Pepe, Davide Chiaravalli, and Claudio Melchiorri. A hybrid teleoperation control scheme for a single-arm mobile manipulator with omnidirectional wheels. In *2016 IEEE/RSJ International Conference on Intelligent Robots and Systems (IROS)*, pages 1450–1455. IEEE, 2016. doi:[10.1109/IROS.2016.7759236](https://doi.org/10.1109/IROS.2016.7759236).
- [86] Pedro O Pereira, Riccardo Zanella, and Dimos V Dimarogonas. Decoupled design of controllers for aerial manipulation with quadrotors. In *2016 IEEE/RSJ International Conference on Intelligent Robots and Systems (IROS)*, pages 4849–4855. IEEE, 2016. doi:[10.1109/IROS.2016.7759712](https://doi.org/10.1109/IROS.2016.7759712).
- [87] Luis Pérez, Eduardo Diez, Rubén Usamentiaga, and Daniel F García. Industrial robot control and operator training using virtual reality interfaces. *Computers in Industry*, 109:114–120, 2019. doi:[10.1016/j.compind.2019.05.001](https://doi.org/10.1016/j.compind.2019.05.001).
- [88] Noé Pérez-Higueras, Alberto Jardón, Ángel Rodríguez, and Carlos Balaguer. An autonomous navigation and exploration system for search and rescue robots in mine incidents. In *2019 IEEE SmartWorld, Ubiquitous Intelligence & Computing, Advanced & Trusted Computing, Scalable Computing & Communications, Cloud & Big Data Computing, Internet of People and Smart City Innovation (SmartWorld/SCALCOM/UIC/ATC/CBDCOM/IOP/SCI)*, pages 213–218. IEEE, 2019. doi:[10.1109/SmartWorld-UIC-ATC-SCALCOM-IOP-SCI.2019.00079](https://doi.org/10.1109/SmartWorld-UIC-ATC-SCALCOM-IOP-SCI.2019.00079).

- [89] Mark Pitonyak and Ferat Sahin. Locomotion and transitional procedures for a hexapod-quadcopter robot. In *2017 IEEE International Conference on Systems, Man, and Cybernetics (SMC)*, pages 1447–1452. IEEE, 2017. doi:[10.1109/SMC.2017.8122817](https://doi.org/10.1109/SMC.2017.8122817).
- [90] Paul EI Pounds, Daniel R Bersak, and Aaron M Dollar. Grasping from the air: Hovering capture and load stability. In *2011 IEEE international conference on robotics and automation*, pages 2491–2498. IEEE, 2011. doi:[10.1109/ICRA.2011.5980314](https://doi.org/10.1109/ICRA.2011.5980314).
- [91] Marc Raibert, Kevin Blankespoor, Gabriel Nelson, and Rob Playter. Bigdog, the rough-terrain quadruped robot. *IFAC Proceedings Volumes*, 41(2):10822–10825, 2008. doi:[10.3182/20080706-5-KR-1001.01833](https://doi.org/10.3182/20080706-5-KR-1001.01833).
- [92] Pablo Ramon-Soria, Begoña C Arrue, and Anibal Ollero. Grasp planning and visual servoing for an outdoors aerial dual manipulator. *Engineering*, 6(1):77–88, 2020. doi:[10.1016/j.eng.2019.11.003](https://doi.org/10.1016/j.eng.2019.11.003).
- [93] Carine Rognon, Stefano Mintchev, Fabio Dell’Agnola, Alexandre Cherpillod, David Atienza, and Dario Floreano. Flyjacket: An upper body soft exoskeleton for immersive drone control. *Robotics and Automation Letters*, 3(3):2362–2369, 2018. doi:[10.1109/LRA.2018.2810955](https://doi.org/10.1109/LRA.2018.2810955).
- [94] Juan Jesús Roldán, Elena Peña-Tapia, David Garzón-Ramos, Jorge de León, Mario Garzón, Jaime del Cerro, and Antonio Barrientos. Multi-robot systems, virtual reality and ros: Developing a new generation of operator interfaces. In *Robot Operating System (ROS)*, pages 29–64. Springer, 2019. doi:[10.1007/978-3-319-91590-6_2](https://doi.org/10.1007/978-3-319-91590-6_2).
- [95] Roberto Rossi. *Control of an unmanned aerial vehicle equipped with a robotic arm*. PhD thesis, Italy, 2017. URL <https://www.politesi.polimi.it/handle/10589/131558>.
- [96] DD Santiago, E Slawinski, and V Mut. Human-inspired stable bilateral teleoperation of mobile manipulators. *ISA transactions*, 95:392–404, 2019. doi:[10.1016/j.isatra.2019.05.006](https://doi.org/10.1016/j.isatra.2019.05.006).
- [97] Y. S. Sarkisov, G. A. Yashin, E. V. Tsykunov, and D. Tsetserukou. Dronegear: A novel robotic landing gear with embedded optical torque sensors for safe multicopter landing on an uneven surface. *IEEE Robotics and Automation Letters*, 3(3):1912–1917, 2018. doi:[10.1109/LRA.2018.2806080](https://doi.org/10.1109/LRA.2018.2806080).
- [98] Yuri S Sarkisov, Min Jun Kim, Davide Bicego, Dzmitry Tsetserukou, Christian Ott, Antonio Franchi, and Konstantin Kondak. Development of sam: Cable-suspended aerial manipulator. In *2019 International Conference on Robotics and Automation (ICRA)*, pages 5323–5329. IEEE, 2019. doi:[10.1109/ICRA.2019.8793592](https://doi.org/10.1109/ICRA.2019.8793592).

- [99] Yuri S Sarkisov, Min Jun Kim, Andre Coelho, Dzmitry Tsetserukou, Christian Ott, and Konstantin Kondak. Optimal oscillation damping control of cable-suspended aerial manipulator with a single imu sensor. In *2020 International Conference on Robotics and Automation (ICRA)*. IEEE, 2020. URL <https://arxiv.org/abs/2003.00472>.
- [100] Shreyas Sen, Jinkyu Koo, and Saurabh Bagchi. Trifecta: security, energy efficiency, and communication capacity comparison for wireless iot devices. *IEEE Internet Computing*, 22(1):74–81, 2018. doi:10.1109/MIC.2018.011581520.
- [101] Dmitrii Shadrin, Mariia Pukalchik, Anastasia Uryasheva, Evgeny Tsykunov, Grigoriy Yashin, Nikita Rodichenko, and Dzmitry Tsetserukou. Hyper-spectral nir and mir data and optimal wavebands for detecting of apple trees diseases. *arXiv preprint arXiv:2004.02325*, 2020. URL <https://arxiv.org/abs/2004.02325>.
- [102] Xuesong Shao, Yiping Yang, Ying Zhang, and Wei Wang. Trajectory planning and posture adjustment of a quadruped robot for obstacle striding. In *2011 IEEE International Conference on Robotics and Biomimetics*, pages 1924–1929. IEEE, 2011. doi:10.1109/ROBIO.2011.6181572.
- [103] H.I. Son. The contribution of force feedback to human performance in the teleoperation of multiple unmanned aerial vehicles. *Multimodal User Interfaces*, 13(4):335–342, 2019. doi:10.1007/s12193-019-00292-0.
- [104] Pedro Sousa, André Ferreira, M Moreira, T Santos, Alfredo Martins, André Dias, José Almeida, and E Silva. Isep/inesc tec aerial robotics team for search and rescue operations at the eurathlon 2015. *Journal of Intelligent & Robotic Systems*, 93(3-4):447–460, 2019. doi:10.1007/s10846-018-0772-1.
- [105] Nicolas Staub, Mostafa Mohammadi, Davide Bicego, Quentin Delamare, Hyunsoo Yang, Domenico Prattichizzo, Paolo Robuffo Giordano, Dongjun Lee, and Antonio Franchi. The tele-magmas: An aerial-ground comanipulator system. *IEEE Robotics & Automation Magazine*, 25(4):66–75, 2018. doi:10.1109/MRA.2018.2871344.
- [106] Boris Stolz, Tim Brödermann, Enea Castiello, Gokula Englberger, Daniel Erne, Jan Gasser, Eric Hayoz, Stephan Müller, Lorin Muhlebach, Tobias Löw, et al. An adaptive landing gear for extending the operational range of helicopters. In *2018 IEEE/RSJ International Conference on Intelligent Robots and Systems (IROS)*, pages 1757–1763. IEEE, 2018. doi:10.1109/IROS.2018.8594062.
- [107] Alejandro Suarez, Guillermo Heredia, and Anibal Ollero. Lightweight compliant arm for aerial manipulation. In *2015 IEEE/RSJ International Conference on Intelligent Robots and Systems (IROS)*, pages 1627–1632. IEEE, 2015. doi:10.1109/IROS.2015.7353585.

- [108] Alejandro Suarez, Guillermo Heredia, and Anibal Ollero. Design of an anthropomorphic, compliant, and lightweight dual arm for aerial manipulation. *IEEE Access*, 6:29173–29189, 2018. doi:[10.1109/ACCESS.2018.2833160](https://doi.org/10.1109/ACCESS.2018.2833160).
- [109] Alejandro Suárez, P Sanchez-Cuevas, M Fernandez, M Perez, Guillermo Heredia, and Anibal Ollero. Lightweight and compliant long reach aerial manipulator for inspection operations. In *International Conference on Intelligent Robots and Systems*, pages 6746–6752. IEEE/RSJ, 2018. doi:[10.1109/IROS.2018.8593940](https://doi.org/10.1109/IROS.2018.8593940).
- [110] Alejandro Suarez, Fran Real, Víctor M Vega, Guillermo Heredia, Angel Rodriguez-Castaño, and Anibal Ollero. Compliant bimanual aerial manipulation: Standard and long reach configurations. *IEEE Access*, 8:88844–88865, 2020. doi:[10.1109/ACCESS.2020.2993101](https://doi.org/10.1109/ACCESS.2020.2993101).
- [111] Da Sun, Andrey Kiselev, Qianfang Liao, Todor Stoyanov, and Amy Loutfi. A new mixed-reality-based teleoperation system for telepresence and maneuverability enhancement. *Transactions on Human-Machine Systems*, 50(1):55–67, 2020. doi:[10.1109/THMS.2019.2960676](https://doi.org/10.1109/THMS.2019.2960676).
- [112] Justin Thomas, Giuseppe Loianno, Joseph Polin, Koushil Sreenath, and Vijay Kumar. Toward autonomous avian-inspired grasping for micro aerial vehicles. *Bioinspiration & biomimetics*, 9(2):025010, 2014. doi:[10.1088/1748-3182/9/2/025010](https://doi.org/10.1088/1748-3182/9/2/025010).
- [113] Evgeny Tsykunov, Ruslan Agishev, Roman Ibrahimov, Luiza Labazanova, Akerke Tleugazy, and Dzmitry Tsetserukou. Swarmtouch: Guiding a swarm of micro-quadrotors with impedance control using a wearable tactile interface. *IEEE transactions on haptics*, 12(3):363–374, 2019. doi:[10.1109/TOH.2019.2927338](https://doi.org/10.1109/TOH.2019.2927338).
- [114] G. A. Yashin, I. A. Kalinov, E. V. Tsykunov, and D. O. Tsetserukou. Touch and weight sensitive robotic arm for uav aimed at aerial manipulation and safe physical human-drone interaction. In *IEEE Haptics Symposium*, 2018. URL <https://cutt.ly/cuv8z5U>.
- [115] G. A. Yashin, D. Trinitatova, R. T. Agishev, R. Ibrahimov, and D. Tsetserukou. Aerovr: Virtual reality-based teleoperation with tactile feedback for aerial manipulation. In *2019 19th International Conference on Advanced Robotics (ICAR)*, pages 767–772, 2019. doi:[10.1109/ICAR46387.2019.8981574](https://doi.org/10.1109/ICAR46387.2019.8981574).
- [116] G. Yashin, D. Trinitatova, N. Zherdev, R. Agishev, and D. Tsetserukou. Airinterface: Study of effectiveness of aerial manipulation using vr system. *Journal of Intelligent & Robotic Systems*. 16 pages, 2020. Submitted.
- [117] G. Yashin, A. Egorov, Zh. Darush, N. Zherdev, and D. Tsetserukou. Locogear: Locomotion analysis of robotic landing gear for multicopters. *IEEE Journal on Miniaturization for Air and Space Systems*, 1(2):138–147, 2020. doi:[10.1109/JMASS.2020.3015525](https://doi.org/10.1109/JMASS.2020.3015525).

- [118] David Valenzuela-Urrutia, Rodrigo Muñoz-Riffo, and Javier Ruiz-del Solar. Virtual reality-based time-delayed haptic teleoperation using point cloud data. *Journal of Intelligent & Robotic Systems*, 96(3-4):387–400, 2019. doi:10.1007/s10846-019-00988-1.
- [119] Robert Valner, Karl Kruusamäe, and Mitch Pryor. Temoto: intuitive multi-range telerobotic system with natural gestural and verbal instruction interface. *Robotics*, 7(1):9, 2018. doi:10.3390/robotics7010009.
- [120] M. Vukobratović and B. Borovac. Zero-moment point — thirty five years of its life. *International journal of humanoid robotics*, 1(01):157–173, 2004. doi:10.1142/S0219843604000083.
- [121] Kandai Watanabe and Masaki Takahashi. Head-synced drone control for reducing virtual reality sickness. *Journal of Intelligent & Robotic Systems*, 97(3):733–744, 2020. doi:10.1007/s10846-019-01054-6.
- [122] R. P. Wells. The kinematics and energy variations of swing-through crutch gait. *Journal of biomechanics*, 12(8):579–585, 1979. doi:10.1016/0021-9290(79)90077-0.
- [123] Brian H Wilcox, Todd Litwin, Jeff Biesiadecki, Jaret Matthews, Matt Heverly, Jack Morrison, Julie Townsend, Norman Ahmad, Allen Sirota, and Brian Cooper. Athlete: A cargo handling and manipulation robot for the moon. *Journal of Field Robotics*, 24(5):421–434, 2007. doi:10.1002/rob.20193.
- [124] Bob G Witmer and Michael J Singer. Measuring presence in virtual environments: A presence questionnaire. *Presence*, 7(3):225–240, 1998. doi:10.1162/105474698565686.
- [125] Yuqiang Wu, Pietro Balatti, Marta Lorenzini, Fei Zhao, Wansoo Kim, and Arash Ajoudani. A teleoperation interface for loco-manipulation control of mobile collaborative robotic assistant. *Robotics and Automation Letters*, 4(4):3593–3600, 2019. doi:10.1109/LRA.2019.2928757.
- [126] Pu Xie, Ou Ma, and Zhen Zhang. A bio-inspired approach for uav landing and perching. In *AIAA Guidance, Navigation, and Control (GNC) Conference*, page 5108, 2013. doi:10.2514/6.2013-5108.
- [127] Pu Xie, Ou Ma, Zhen Zhao, and Lin Zhang. A bio-inspired uav leg-foot mechanism for landing, grasping and perching tasks. In *AIAA Atmospheric Flight Mechanics Conference*, page 1689, 2015. doi:10.2514/6.2015-1689.
- [128] Holly A Yanco, Jill L Drury, and Jean Scholtz. Beyond usability evaluation: Analysis of human-robot interaction at a major robotics competition. *Human-Computer Interaction*, 19(1-2):117–149, 2004. doi:10.1080/07370024.2004.9667342.
- [129] Pengfei Yu, Zihao Wang, and KC Wong. Exploring aerial perching and grasping with dual symmetric manipulators and compliant end-effectors.

- International Journal of Micro Air Vehicles*, 11:1756829319877416, 2019. doi:10.1177/1756829319877416.
- [130] Burak Yüksel and Antonio Franchi. Pvtol aerial manipulators with a rigid or an elastic joint: Analysis, control, and comparison. 2016. URL <https://hal.archives-ouvertes.fr/hal-01388462/>.
- [131] Ali Zamani, Mahdi Khorram, and S Ali A Moosavian. Dynamics and stable gait planning of a quadruped robot. In *2011 11th International Conference on Control, Automation and Systems*, pages 25–30. IEEE, 2011. URL <https://ieeexplore.ieee.org/abstract/document/6106373>.